

UC San Diego

UC San Diego Electronic Theses and Dissertations

Title

Toward multifunctional nanoparticle-based therapeutics

Permalink

<https://escholarship.org/uc/item/64w2m2kw>

Author

Derfus, Austin Matthew

Publication Date

2006

Peer reviewed|Thesis/dissertation

UNIVERSITY OF CALIFORNIA, SAN DIEGO

**TOWARDS MULTIFUNCTIONAL NANOPARTICLE-
BASED THERAPEUTICS**

A dissertation submitted in partial satisfaction of the requirements

for the degree Doctor of Philosophy

in

Bioengineering

by

Austin Matthew Derfus

Committee in charge:

Professor Sangeeta N. Bhatia, Chair
Professor Erkki Ruoslahti, Co-chair
Professor Michael J. Heller
Professor Xiaohua Huang
Professor Michael J. Sailor

2006

Copyright

Austin Matthew Derfus, 2006

All rights reserved

The dissertation of Austin Matthew Derfus is approved,
and it is acceptable in quality and form for publication
on microfilm:

Chair

University of California, San Diego

2006

For Mom and Dad. They taught me the important stuff.

TABLE OF CONTENTS

Signature Page	iii
Dedication Page	iv
Table of Contents.....	v
List of Figures and Tables	viii
Acknowledgements.....	xi
Vita.....	xiii
ABSTRACT	xv
CHAPTER 1: Introduction	1
1.1. Cancer.....	2
1.2. Current state of the art.....	3
1.3. Intracellular delivery	8
1.4. Biological applications of quantum dots.....	11
1.5. Remote actuation.....	13
1.6. In this thesis.....	17
CHAPTER 2: Intracellular Delivery of Quantum Dot Bioconjugates.....	20
2.1. Abstract.....	20
2.2. Introduction	20
2.3. Materials and Methods	21
2.4. Results and Discussion.....	24
2.5. Conclusion.....	35
2.6. Acknowledgements	36
CHAPTER 3: Quantum Dots to Monitor siRNA delivery	37
3.1. Abstract.....	37
3.2. Introduction	38

3.3. Materials and Methods	40
3.4. Results and Discussion	44
3.5. Conclusion	53
3.6. Acknowledgements	55
CHAPTER 4: Targeted Quantum Dot Conjugates for siRNA Delivery.....	56
4.1. Abstract.....	56
4.2. Introduction	56
4.3. Materials and Methods	60
4.4. Results and Discussion	63
4.5. Conclusion.....	70
4.6. Acknowledgements	70
CHAPTER 5: Probing the Cytotoxicity of Semiconductor Quantum Dots.....	71
5.1. Abstract.....	71
5.2. Introduction	71
5.3. Materials and Methods	73
5.4. Results and Discussion	77
5.5. Conclusion.....	94
5.6. Acknowledgements	95
CHAPTER 6: Remotely Triggered Release from Magnetic Nanoparticles.....	96
6.1. Abstract.....	96
6.2. Introduction	97
6.3. Materials and Methods	98
6.4. Results and Discussion	106
6.5. Conclusion.....	110
6.6. Epilogue.....	111
6.7. Acknowledgements	114

CHAPTER 7: Summary and Conclusions	115
7.1. Perspectives on siRNA delivery	115
7.2. Potential for clinical use of quantum dots	117
7.3. Improving the feasibility of remotely triggered release	119
REFERENCES	121

LIST OF FIGURES AND TABLES

Figure 1.1 – Multifunctional nanoparticle concept	1
Figure 1.2 – Intracellular delivery strategies.....	8
Table 2.1 - Optimization of electroporation parameters for HeLa cells in PBS	23
Figure 2.1 - Improved Intracellular QD Delivery Quantified by Flow Cytometry	26
Figure 2.2 - Confocal imaging of QD/cationic liposome intracellular delivery	27
Figure 2.3 - Comparison of Delivery Methods	29
Figure 2.4 - EGF-QDs colocalize with an endosome marker	29
Figure 2.5 - Microinjection of PEG-QDs in 3T3 cells.....	31
Figure 2.6 - Subcellular Localization of Single QDs	34
Figure 3.1 - QD/siRNA complexes allow sorting of gene silencing in cell populations	46
Figure 3.2 - Immunofluorescence staining of Lamin A/C nuclear protein	47
Figure 3.3 - Optimization of QD concentration for siRNA tracking	48
Figure 3.4 - Sorting the effects of double gene knockdowns using two colors of QDs	50
Figure 3.5 - Fluorescence/phase micrographs of two color QD transfections	51
Figure 3.6 - Significant downstream gene knockdown effects of T-cadherin gene silencing are observed only in a homogenous silenced cell population.....	52
Figure 3.7 - Knockdown efficacy is not improved by transfecting higher doses of siRNA	54
Figure 3.8 - Comparison of QD and fluorescein-labeled siRNA fluorescence in 3T3 murine fibroblasts.....	55
Figure 4.1 - Scheme for delivery of QD/siRNA conjugates	59
Figure 4.2 - Attachment of F3 peptide leads to QD internalization in HeLa cells.....	64

Figure 4.3 - Conjugation of siRNA to QDs with cleavable or non-cleavable crosslinkers.....	67
Figure 4.4 - EGFP knockdown is limited by number of siRNA per QD and endosome entrapment.....	69
Figure 5.1 - Toxicity Of CdSe Quantum Dots In Liver Culture Model Is Dependent On Processing Conditions And Nanoparticle Dose	79
Figure 5.2 - Toxicity Of QDs Correlates with Surface Oxidation, Decrease of QD size, and Disruption of Crystal Lattice	81
Figure 5.3 - Surface Oxidation Leads to Release of Cadmium Ions	84
Figure 5.4 - Effects of ZnS Surface Coating on Surface Oxidation, Release of Cadmium, and Cytotoxicity.....	86
Figure 5.5 - Effects of Bovine Serum Albumin Surface Coating on Surface Oxidation and Cytotoxicity	88
Figure 5.6 - Application of Coated QDs to Long-term Tracking of Primary Cells Without Compromising Liver-specific Function	93
Figure 6.1 - Scheme for EMF-triggered release from magnetic nanoparticles	97
Table 6.1 - Oligonucleotide sequences.....	99
Figure 6.2 - Melting transition can be shifted by varying complement length	99
Figure 6.3 - Experimental Setup for conductive heat transfer measurements.....	101
Figure 6.4 - EMF-induced temperature rise varies with particle concentration and sample diameter.....	102
Figure 6.5 - Shorter heating intervals applied to higher particle concentrations reduces collateral heating	103
Figure 6.6 - Experimental setup for EMF application to tumor phantoms	104

Figure 6.7 - Superparamagnetic nanoparticles transduce external electromagnetic energy to heat, thereby melting oligonucleotide duplexes that act as heat-labile tethers to model drugs	107
Figure 6.8 - Release from nanoparticles in vivo	108
Figure 6.9 - Images of tissue/phantom boundary in +EMF group used to quantify penetration depth	109
Figure 6.10 - Images of tissue/phantom boundary in -EMF group used to quantify penetration depth	110
Figure 6.11 - Scheme for fabrication of alginate beads containing releasable particles	113
Figure 6.12 - Characterization of magnetic particle hydrogels	114

ACKNOWLEDGEMENTS

I have had a lot of help along the way. Warren Chan taught me how to make Qdots. Mike Sailor let us stink up his lab and always make me feel like part of the group. Salman Khetani (along with Sangeeta) taught me everything I know about hepatocytes. Jen Felix Rio spent hours over the surgery table isolating those cells. Geoff von Maltzahn had some great ideas along the way (along with some crazy ones). Todd Harris kept working hard even when I got discouraged. Alice Chen is a western blot machine and always kept me excited about our projects. Tasmia Duza was a good teacher and advice-giver. The chemists from the Sailor lab were great – Mike Schwartz, Joe Park, Jason Dorvee and Sara Alvarez. I also got a lot of help and advice from the rest of MTEL/LMRT, especially Chris Flaim, Greg Underhill, Elliot Hui, Dirk Albrecht, Vicki Chin, and Val Lui Tsang. The Ruoslahti lab became my adopted home in March of 2005, and all of them have been welcoming and helpful. I am in debt to Erkki for letting me join the team. A generous G.R.E.A.T. fellowship the UC Biotechnology Research and Education Program has paid the bills for the last two years, granting me independence in times of change.

A special thanks to Sangeeta for believing in me, giving great pep talks, and teaching me to be a scientist.

Gayle was always there with a sympathetic ear and lots of questions.

Chapter 2 was reproduced in full from Derfus AM, Chan WCW, and Bhatia SN. “Intracellular Delivery of Quantum Dots for Live Cell Labeling and Organelle Tracking.” *Advanced Materials* **16** (2004): 961-966. The dissertation author was the primary investigator and first author on the paper. He thanks Warren Chan and Sangeeta Bhatia for their significant contributions to the work.

Chapter 3 was reproduced in full from Chen AA, Derfus AM, Khetani SR and Bhatia SN. “Quantum Dots to Monitor RNAi delivery and Improve Gene Silencing.” *Nucleic Acids Research* **33** (2005):e120. The dissertation author was the co-primary investigator and co-first author on the paper. He thanks Alice Chen, Salman Khetani, and Sangeeta Bhatia for their significant contributions to the work.

Chapter 4 was reproduced in part from Derfus AM, Chen AA, Ruoslahti E, Bhatia SN. “Targeted Quantum Dot conjugates for siRNA delivery” (submitted to *Bioconjugate Chemistry*). The dissertation author was the primary investigator and first author on the paper. He thanks Alice Chen, Erkki Ruoslahti, and Sangeeta Bhatia for their significant contributions to the work.

Chapter 5 was reproduced in full from Derfus AM, Chan WCW, and Bhatia SN. “Probing the Cytotoxicity of Semiconductor Quantum Dots.” *Nano Letters* **4** (2004): 11-18. The dissertation author was the primary investigator and first author on the paper. He thanks Warren Chan and Sangeeta Bhatia for their significant contributions to the work.

Chapter 6 was reproduced in part from Derfus AM, von Maltzahn G, Harris TJ, Duza T, Vecchio KS, Ruoslahti E, Bhatia SN. “Remotely Triggered Release from Magnetic Nanoparticles” (submitted to *Nature Nanotechnology*). The dissertation author was the primary investigator and first author on the paper. He thanks Geoff von Maltzahn, Todd Harris, Tasmia Duza, Ken Vecchio, Erkki Ruoslahti, and Sangeeta Bhatia for their significant contributions to the work.

VITA

1979	Born, Rhinelander, Wisconsin
2001	B.S.E., Duke University
2003	M.S., University of California, San Diego
2006	Ph.D., University of California, San Diego

Publications

Derfus AM, Chan WC, and Bhatia SN. “Probing the Cytotoxicity of Semiconductor Quantum Dots.” *Nano Letters* **4** (2004): 11-18.

Derfus AM, Chan WC, and Bhatia SN. “Intracellular Delivery of Quantum Dots for Live Cell Labeling and Organelle Tracking.” *Advanced Materials* **16** (2004): 961-966.

Dorvee JR, **Derfus AM**, Bhatia SN and Sailor M. “Manipulation of liquid droplets using amphiphilic, magnetic one-dimensional photonic crystal chaperones.” *Nature Materials* **3** (2004): 896–899.

Chen AA*, **Derfus AM***, Khetani SR and Bhatia SN. “Quantum Dots to Monitor RNAi delivery and Improve Gene Silencing.” *Nucleic Acids Research* **33** (2005):e120. *authors contributed equally

Harris TJ, von Maltzahn G, **Derfus AM**, Ruoslahti E, Bhatia SN. “Proteolytic Actuation of Nanoparticle Self-Assembly.” *Angewandte Chemie Int. Ed.* **45** (2006): 3161-3165.

- Sunderland CJ, Steiert M, Talmadge JE, **Derfus AM**, Barry SE. “Targeted nanoparticles for detecting and treating cancer.” *Drug Development Research* **67** (2006): 70-93.
- Park J, **Derfus AM**, Segal E, Vecchio KS, Bhatia SN, Sailor MJ. “Local Heating of Discrete Droplets Using Magnetic Porous Silicon-based Photonic Crystals.” (in press, *Journal of the American Chemical Society*)
- Schwartz MP, **Derfus AM**, Alvarez SD, Bhatia SN, Sailor MJ. “The smart petri dish: A nanostructured porous photonic crystal for monitoring living cells.” (in press, *Langmuir*)
- Derfus AM**, von Maltzahn G, Harris TJ, Duza T, Vecchio KS, Ruoslahti E, Bhatia SN. “Remotely Triggered Release from Magnetic Nanoparticles.” (submitted to *Nature Nanotechnology*)
- Derfus AM**, Chen AA, Ruoslahti E, Bhatia SN. “Targeted Quantum Dot conjugates for siRNA delivery.” (submitted to *Bioconjugate Chemistry*)

ABSTRACT OF THE DISSERTATION

TOWARDS MULTIFUNCTIONAL NANOPARTICLE-BASED THERAPEUTICS

by

Austin Matthew Derfus

Doctor of Philosophy in Bioengineering

University of California, San Diego, 2006

Professor Sangeeta N. Bhatia, Chair

Professor Erkki Ruoslahti, Co-chair

The diagnosis and treatment of solid tumors may be improved by tailoring nanoparticles for drug delivery and medical imaging. The core of the nanoparticle can offer diagnostic imaging capabilities while simultaneously providing a multivalent scaffold for other moieties that impart additional functions such as improved pharmacokinetics and remote sensing. To move towards these goals, this thesis explores methods to traffic particles in living systems, delivery of therapeutic cargo, the biocompatibility of nanomaterials, and strategies to exploit the utility of the nanoparticle core. This work employs two inorganic nanoparticle cores that can be visualized, luminescent semiconductor quantum dots (QDs) and superparamagnetic iron oxide nanocrystals, and explores adding functionality to these scaffolds in a ‘modular’ fashion such that they can later be combined for specific applications.

While many therapeutic ‘payloads’ act intracellularly, cell membranes are impermeable to unmodified inorganic nanoparticles, as they are to free

oligonucleotides. Given their similar size and charge, we explored gene delivery methods to ferry QDs across the lipid bilayer. Trafficking these particles to subcellular organelles required intracellular monodispersity achieved through microinjection; however, therapeutic cargo (small interfering RNA) could be efficiently delivered along with nanoparticle aggregates via complexation with cationic liposomes. To further enable systemic delivery, the functions of the cationic liposome (multivalent carrier for siRNA, cellular uptake, endosomal escape) were replaced with chemical crosslinkers and tumor homing peptides derived from in vivo phage display. One concern regarding the systemic use of cadmium-containing particles is the potential release of cytotoxic components. We found that breakdown of the CdSe core can occur in oxidative environments, but can also be largely mitigated by the use of additional capping layers. Finally, we explored the use of iron oxide nanoparticle cores as they have the potential to act as transducers of external energy to actuate the release of a model therapeutic on demand. Electromagnetic fields generate local heating of iron oxide, which was harnessed to cleave a tunable heat-labile bond. Collectively, our investigations into delivery, biocompatibility, and remote actuation form an integrated basis for the vision of multifunctional nanoparticles that combine diagnostic and therapeutic capabilities.

CHAPTER 1

INTRODUCTION

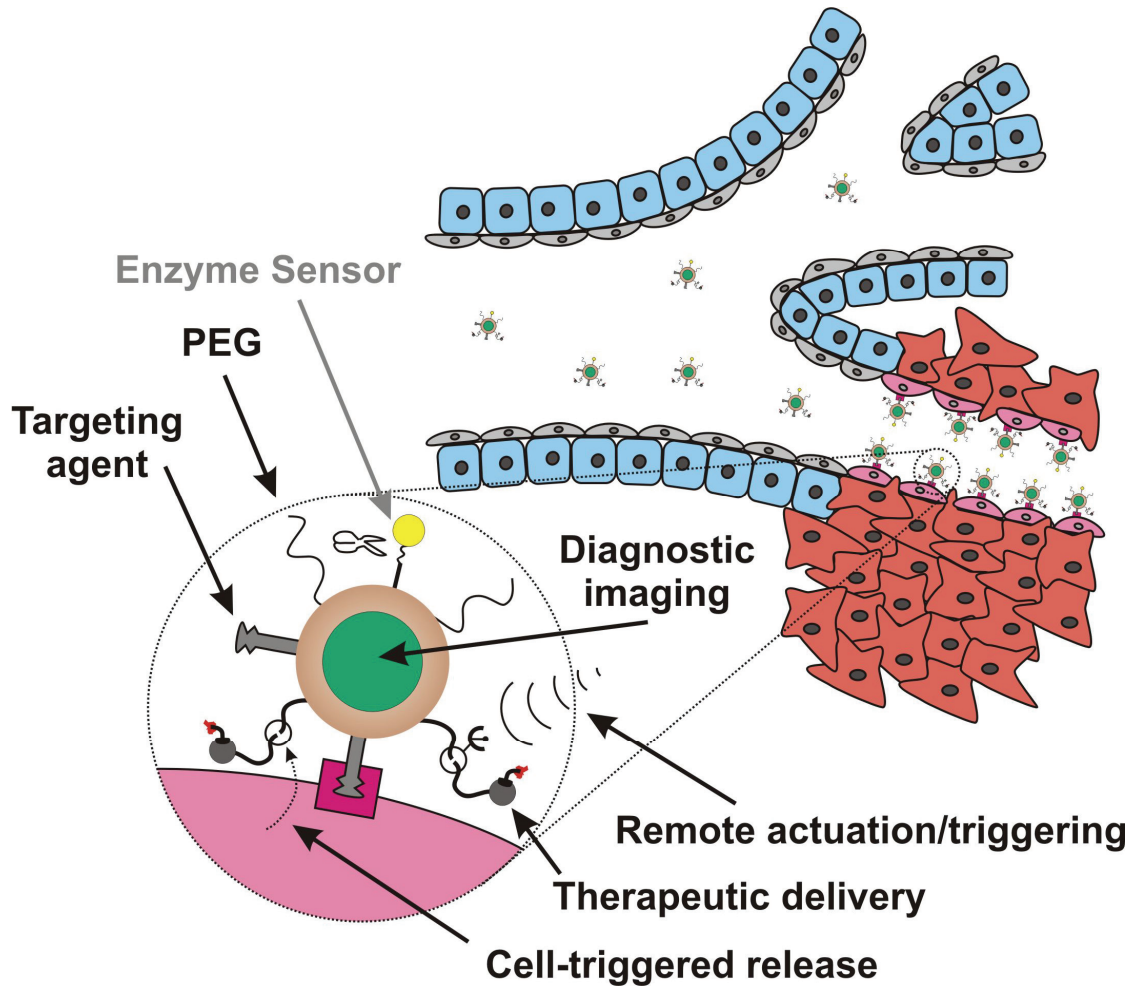


Figure 1.1 – Multifunctional nanoparticle concept. The eventual goal of this research is to design multifunctional nanoparticle-based therapeutics for solid tumors, which can selectively bind to a disease site, release a drug, and report on its location and microenvironment.

1.1 Cancer

Cancer is the uncontrolled growth of cells that have mutated from normal tissues. Cancerous tumors can develop in almost any organ or tissue and occur when cells express oncogenes, altered versions of genes responsible for regulating growth and differentiation. These malignant cells divide continuously and invade nearby, normal tissue, leading to organ dysfunction. Upon reaching blood vessels or lymphatics, cancer cells can spread to other portions of the body, forming metastases. Metastasis can be particularly damaging if it occurs in essential areas, such as parts of the brain. Next to heart disease, cancer is second leading cause of death in the US.

Cancer therapy typically begins with an imaging test (X-ray, CT, ultrasound, PET), to identify the location of a tumor, its size, and extent of spreading. Weak image contrast between cancerous and normal tissue often makes diagnosis difficult, however, and intravenous contrast agents are often required. Generally, these tests only indicate a suspicious area, and a biopsy of the tissue is taken to screen for cancer cells. If cancer (or precancerous) tissue is present, the tumor is typically removed with surgery. Because cancer begins as a focal disease and the most common cancers (breast, prostate, colon, and lung) develop in organs that can be completely or partially removed, resection is an effective means of reducing tumor mass. With the hope of extracting all the cancerous tissue, normal tissue at the boundaries of a malignant area is also removed. For some areas, such as parts of the brain, full tumor removal is not an option. The patient is then treated with small molecule drugs (e.g. alkylating agents) or high dose radiation (applied externally or with implanted seeds). While each of these treatments preferentially damages dividing cells, collateral injury to non-cancerous tissues and associated side effects (nausea, hair loss, fatigue) are very common. For this reason, targeted drug delivery to tumors is an active area of

research. Selective delivery of cytotoxic agents to the tumor would allow reduced dosage and would alleviate damage to normal tissues. If the tumor mass is reduced and treatment discontinued, the patient is typically monitored for the remainder of their lifetime for recurrence of malignant cells. Non-invasive tests for some cancers do not exist and repeated biopsy may be required.

To achieve these treatment goals, the tools of cancer therapy currently include image contrast agents (iron oxide, gadolinium), therapeutics (small molecule drugs, genes), and ligands for detection (antibodies, peptides). Combining these tools in a single, multifunctional conjugate would allow important functions in cancer therapy (imaging, tumor destruction, monitoring of regression, etc) to take place simultaneously and more effectively. Engineering supramolecular structures to perform these functions has proven more complex than co-conjugation of multiple chemical species, and dozens of research groups around the world are taking diverse approaches to the task at hand.

1.2 Current state of the art

Early efforts have focused on targeting of a nanoparticle imaging agent or drug carrier to a disease site. Typically, these systems begin with a core or backbone particle or polymer. In some cases, the particle is an imaging agent (quantum dots^{1, 2}, iron oxide^{3, 4}, perfluorocarbon⁵, etc). A small molecule imaging agent (fluorophore⁶, gadolinium⁷, etc) may also be attached to the particle's surface, or encapsulated within the particle core. In a similar manner, drugs have been attached to the surface of particles, or on their interior. Few groups have simultaneously demonstrated the three functions of targeting, therapeutic delivery and imaging on a single platform, though the capability exists for many of these technologies.

Our group has experience homing fluorescent quantum dots to tumors and other sites¹. Using phage display-derived peptides conjugated to their surface, the particles are shown to accumulate in the tumor vasculature (F3 peptide) or lymphatics (Lyp-1) or normal lung tissue (GFE). As endothelial cells from different tissues express varying surface antigens and receptors, peptide ligands can be identified that bind these unique epitopes. In phage-display screening, a bacteriophage is used to probe the vasculature for these differences. The virus particles are engineered to display peptides on their surface, and a library ($\sim 10^9$) of various sequences can be built with a multiple copies of a single sequence on each phage. When this library is injected intravenously in a tumor-bearing mouse and allowed to circulate, phage accumulating in the tumor can be collected and amplified. Multiple rounds of in vivo screening (and typically in vitro screening as well) lead to a set of tumor-homing peptides, which may find use in targeting drugs or particles. In addition to tumor targeting peptides, sequences specific to a variety of normal and diseased tissues have been identified (lung, heart, blood clots, etc).

When using these peptides to target quantum dots, conjugation with polyethylene glycol (PEG) was necessary to reduce accumulation in the liver and spleen. For many particle systems, their size ($>5\text{nm}$), leads to non-specific uptake by the reticuloendothelial system (RES) of the liver and spleen is essential. Macrophages in these organs remove particulate from the circulation rapidly. Several reports have demonstrated success with adding stealth molecules, such as PEG, to evade the RES^{1, 8, 9}.

Nie and coworkers have also investigated targeted delivery of quantum dots to xenograft tumors, using antibodies against prostate specific membrane antigen (PSMA)². Even with PEG, however, significant liver and spleen uptake was observed, possibly due to their increased size after addition of a polymer layer and

antibodies. Antibodies are the native homing molecules of the immune system and are a natural first choice. Yet, antibodies are also large (~10nm), and must be “humanized” or will garner a deleterious immune response. Peptides are less immunogenic than antibodies, and much smaller (~0.5-5kDa for a 4-40mer). Traditionally, the binding affinity for peptides has been significantly less than antibodies (~nM for Abs), and must be compensated by increasing the peptide number (increasing avidity). Yet, several recently discovered homing peptides have shown nanomolar affinities^{10,11}.

Aptamers, like peptides, are less immunogenic and can be screened to target various organs or disease states⁶. Langer and coworkers attached RNA aptamers to poly(lactic acid) – polyethylene glycol (PLA-PEG) diblock copolymers, which self-assemble into larger (200-300nm) particles. As a proof of concept, these particles carried fluorescent dextran, though the encapsulation of drugs or imaging agents is possible. A drawback with RNA, however, is the presence of ubiquitous nuclease enzymes that will digest the nucleic acid unless costly modifications are made to their phosphodiester backbone. Locked nucleic acids (LNA), peptide nucleic acids (PNA), and morpholinos are potential options for more stable variants.

Finally, small molecules whose receptors are overexpressed in some tumors have also been used for targeting. Folate, for example, has been attached to dendrimers^{12,13} and carbon nanotubes¹⁴ for targeting. Conjugation with methotrexate, a folate antagonist and chemotherapeutic, has also been achieved with iron oxide particles¹⁵. Upregulation of the folate receptor, however, is not uniform across all tumors¹⁶.

In addition to these forms of active targeting, passive uptake in tumors is significant due to the increased “leakiness” of the tumor vasculature¹⁷. Several targeting strategies use this occurrence, often referred to as the enhanced permeability

and retention (EPR) effect, to accumulate particles in the tumor. West, Halas, and coworkers at Nanospectra Biosciences have used this effect to accumulate PEGlyated gold nanoshells in tumors¹⁸. Irradiation of the nanoshells by a near-infrared source leads to tumor ablation, reduction in lesion size, and improved survival. In these experiments, however, collateral uptake was unimportant, as only the tumor area was irradiated. In addition to the tumor, normal hepatic vasculature contains fenestrae as well, leading to undesirable accumulation in the liver in cases where passive targeting is utilized.

In a laboratory environment, fluorescence is arguably the easiest imaging technology to incorporate. In addition to approaches using quantum dot cores, organic dyes can be covalently linked to most particle systems for tracking in vitro and in vivo. Imaging with fluorescence, while useful for intraoperative means (tumor boundaries, sentinel node mapping¹⁹), does not allow non-invasive imaging of deeper tissues. Wickline, Lanza and coworkers have instead chosen an acoustically reflective perfluorocarbon (PFC) core, useful for ultrasound imaging⁵. Generated by emulsion and coated with a lipid layer, the group has also attached anti-angiogenic antibodies to the particles and shown targeting to tumors⁷ and fibrin clots²⁰. The particles can also be useful for other imaging modalities by incorporating gadolinium-chelate complexes or radionuclides in the lipid coat. Their total particle size is quite large (~200nm diameter), due to a size requirements on the PFC core for generating ultrasound contrast. Perhaps for this reason, targeting with peptides (lower affinity) has not been effective, though antibodies to integrins have been successful^{7, 21}. Additionally, while drug can be incorporated in the coat, this loading amounts to a low weight percent of the particle.

Superparamagnetic iron oxide-core particles also provide MR contrast, enabling whole body imaging. These particles tend to be significantly smaller (5-10 nm core,

30-50 nm total size) than the PFC emulsion. For many years, Weissleder and coworkers have been developing dextran-coated particles for imaging of liver and spleen tumors, which are now clinically available (Feridex). For these particles, uptake by macrophages of the RES generates contrast, as malignant areas of these tissue lack a large population of these cells²². In addition, these particles have been made fluorescent²³ and targeted using antibodies³ and peptides²⁴. As synthesis of these particles is fairly simple, many other groups are currently working on this platform^{4, 15, 25}. Most of the focus is on targeted image contrast, with less effort in using these particles for drug delivery (though a handful of strategies have been investigated^{26, 27}).

For many of these systems, targeted intracellular delivery is still a problem. Though uptake often occurs with peptide or antibody ligands, these particles (and more importantly their therapeutic cargo) remain trapped in endosomal vesicles. Many drugs (e.g. alkylating agents) and genes (e.g. plasmids) act in the nucleus or cytoplasm (e.g. siRNA). While translocation peptides, like HIV-tat, have shown use for nuclear delivery²⁸, these particles would enter all cells *in vivo*, not tumor cells specifically²⁹. Perhaps some insights can be gained from the gene delivery field, which faces similar boundaries.

Additionally, biocompatibility of some inorganic nanoparticles, particularly quantum dots, has not been demonstrated. Numerous *in vivo* applications have been suggested for these bright, photostable particles (see section 1.4 below), but the heavy metals that compose their cores are potentially cytotoxic if released. Investigation into potential conditions for breakdown, and means to slow this degradation, is necessary.

Finally, the ability to externally control the particles, once delivered, is also lacking. Remote actuation would allow multistage delivery of therapeutics (a

sensitizer followed by a drug³⁰), or immune adjuvant (generating an amplified secondary response). While several strategies for external energy input have been identified (section 1.5), few attempts have been made to trigger a chemical reaction or affect release.

1.3 Intracellular delivery

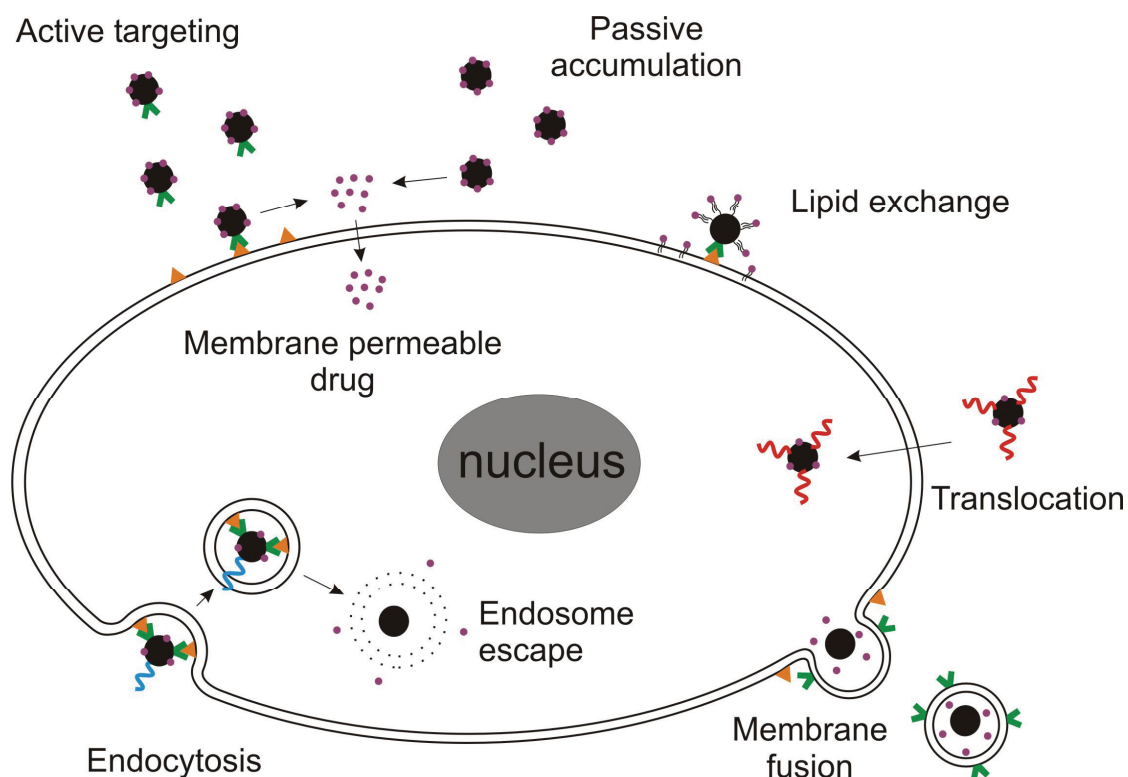


Figure 1.2 – Intracellular delivery strategies. Numerous means are available to enable entry of nanoparticles or their therapeutic payload into cells.

Particle systems can arrive at the tumor site through active targeting (e.g. peptides, antibodies, aptamers, etc) or passive accumulation (e.g. EPR), but to deliver cargo to the interior of a cell, the plasma membrane must be traversed. For particles that carry a membrane-permeable drug (typically hydrophobic, low molecular weight small molecules), extracellular release is sufficient. In fact, uptake of the entire

particle may reduce efficiency of the drug, as degradation in acidic intracellular compartments is possible. A similar, but innovative, solution is to rely on lipid exchange between a lipid-coated nanoparticle and the plasma membrane. Lanza and coworkers found that direct binding of lipid-coated particles to cells increased the rate and duration of this typically slow exchange³¹.

If particles and their cargo enter a cell together, active transport (ATP required) through receptor-mediated endocytosis (RME) is typical. Phagocytosis (only in macrophages) and pinocytosis (non-specific “cellular drinking”) are other means, though less useful for particles. In RME, recognition at the cell’s surface leads to the formation of a clathrin-coated pit, which is invaginated, encapsulating the receptor and ligand in a cytoplasmic vesicle (endosome). For imaging agents, endocytosis can prevent clearance over time, retaining the label for extended periods. Yet, in the case of drug delivery, ferrying the particle to the cytoplasm (free of vesicles) is ideal, either by triggering endosomal escape or avoiding the endosomal pathway altogether.

Much can be learned from viruses (e.g. HIV, influenza), as they enter cells and deliver their genetic information to the nucleus. The HIV virus enters cells using a gp41 fusion protein, which triggers membrane fusion. This route of entry may be a possibility for liposomal delivery³², but may only apply to enveloped systems. The tat peptide from HIV has been used to deliver liposomes³³ as well, but also iron oxide particles³⁴. The activity of this peptide is derived from its basic amino acids, and others have used polyarginine peptides with similar effects³⁵. In the case of iron oxide, particles were shown to accumulate in the nucleus after entry. It was long believed that tat resulted in direct membrane translocation, bypassing the endosomal pathway, due to its temperature and energy independent uptake³⁶. Several reports now indicate that cell uptake followed by endosomal escape is more likely, though the exact mechanism (raft-dependent macropinocytosis³⁷ or clathrin-mediated

endocytosis³⁸) of internalization is still in question. In addition, fusogenic peptides derived from the HA2 domain of influenza have been conjugated to immunoliposomes for gene delivery³⁹. In this case, the lowered pH of the endosome (~5) triggers a conformational change in the peptide's alpha helix, leading to membrane insertion and pore formation or lysis. For these peptides, a ligand for specific cell uptake could be used in tandem for targeting specificity. In some cases, however, in vivo use has shown delivery to all tissues, which would be undesirable²⁹. Several homing peptides derived from phage display combine both these properties, and have shown nuclear accumulation in a targeted cell population⁴⁰.

Gene delivery faces many of the problems associated with delivering particles to cells, and several strategies have been developed. Conjugation with cationic transfection reagents serves to condense negatively-charged nucleic acids, but also functions in endosome escape. These reagents include cationic liposomes (Lipofectamine), polymers (poly(ethylene imine) (PEI)), and dendrimers (SuperFect). Typically, these species act as proton sponges, causing osmotic swelling and lysis of the endosome as the pH is lowered. Attempts to use cationic liposomes in vivo have met with some success⁴¹, though their circulation time is minimal (due to their size and positive charge) and delivery to organs other than the liver may prove difficult.

Other cell biology tools employ physical means for cell entry, such as electroporation and microinjection. Electroporation involves the application of a short (~milliseconds) DC electric field pulse to cells, which causes the formation of temporary pores in their membrane. Materials from outside the cell are then free to diffuse inside. Microinjection of genes and proteins is accomplished using a glass pipette with a narrow fit diameter (~microns). Small (nanoliter) quantities of solutions are injected into the cytoplasm or nucleus. Microinjection of quantum dot micelles into *Xenopus* embryos has been accomplished⁴², though this technique may be limited

to in vitro use. On the other hand, in-vivo electroporation is practiced, and was recently utilized to deliver gold nanoparticle-DNA conjugates to liver cells⁴³.

When investigating cell uptake, it is essential to have a means of tracking the particle throughout the delivery process. Fluorescence is the most useful for an in vitro setting, and thus, luminescent quantum dots are an ideal nanoparticle probe for this purpose.

1.4 Biological applications of quantum dots

Quantum dots (QDs) are semiconductor nanocrystals that exhibit fluorescence due to quantum confinement. This occurs when the size of the material is below the Bohr exciton radius (~nm), the separation distance between an electron and hole pair (exciton) in the bulk material. An exciton is created by incident light of sufficient energy – greater than the bandgap. In a QD, the exciton is confined and electron-hole recombination leads to emission of stoke-shifted light. Also at this size, energy levels are quantized, with a bandgap that is directly related to the crystal's size. Smaller crystals fluoresce in the blue, and larger in the red. The most common quantum dot core material is cadmium selenide (CdSe), with a few monolayers of zinc sulfide (ZnS) as a capping layer or overcoat. Due to a larger bandgap, the ZnS layer reduces surface traps (blinking) and protects the surface from oxidation, increasing the quantum yield⁴⁴. To the surface of these particles, addition organic layers can be added (polymers, proteins, peptides, etc), or ligands can be directly adsorbed to the ZnS cap. The QD surface is hydrophobic, and amphiphilic ligands must be added to render the particles water-soluble.

Advantages of QDs over organic dyes for biological applications include increased brightness, narrow emission widths and improved photostability⁴⁵. Also, all sizes of QDs have a broad absorption cross-section in the UV, allowing multiple

colors to be excited with a single source. While few researchers have taken advantage of this multi-color aspect, labeling of a million (10 colors, 6 intensity levels) unique nucleic acid sequences has been proposed⁴⁶. Due to their brightness, single QDs (identified by their blinking) can be observed and were used to track glycine receptors in neurons⁴⁷. With peptide/QD conjugates delivered via microinjection, we labeled the nucleus and mitochondria in live cells, utilizing QD photostability to track mitochondrial movement⁴⁸. Other in vitro uses include labeling extracellular epitopes in live cells (Her2⁴⁹, erb/HER⁵⁰, P-glycoprotein⁵¹), in-situ hybridization (FISH)⁵², and resonant energy transfer (FRET) biosensors⁵³.

In vivo, QDs have been used to target tumor tissue^{1, 2}, monitor tumor cell invasion⁵⁴, map sentinel lymph nodes¹⁹, track cell differentiation⁴², and image vessel flow⁵⁵. These applications have prompted the suggestion that quantum dots could find clinical uses, though the issue of cytotoxicity must first be addressed⁵⁶. Alternative materials and more advanced coating strategies are under investigation. One example is the synthesis of gold QDs, which are very small (5-31 atoms) and can be fluorescent in the near-IR (useful for in vivo applications)⁵⁷.

In addition to delivery and biocompatibility of particle systems, we are also interested in remote actuation of particles, which is theoretically possible with QDs⁴⁵. Due to a non-ideal (typically 20-80%) quantum yield, QDs also produce heat in addition to emission light. The conversion of incident light to heat could be used as a trigger a chemical reaction or hyperthermic cell death. In addition, singlet oxygen is produced when excited electrons escape from the core. For this reason, QDs have been suggested as a potential photosensitizer for photodynamic therapy⁵⁸. Each of these applications, however, would require excitation with light (visible or near-IR), which has a finite penetration depth. QDs also have distinct x-ray absorption, suggesting energy could be deposited to deep tumors with higher energy EM

radiation⁵⁹. Again, the absorption differential is not ideal, as normal tissue also absorbs x-rays significantly and a large mass of QDs would be required to make such a treatment effective. Instead of continuing with QDs to investigate remote actuation, we have chosen to explore other means (and other particles) for external control.

1.5 Remote actuation

Remote actuation involves the transmission of an extracorporeal signal to an implant, which is transduced into useful work. The signal can take a variety of forms – both mechanical (ultrasound) and electromagnetic (light, x-ray, EM fields). Previous attempts at remote actuation have involved a variety of these energy forms.

Ultrasound imaging, for example, utilizes compression (mechanical) waves at ultrasonic frequencies (~MHz) to image tissue boundaries (differences in refractive index). Ultrasound contrast agents consist of microbubbles containing gases that are excellent reflectors of acoustic energy^{60, 61}. Typically, these are delivered i.v. and grant vascular contrast. In some applications, these have been coated with therapeutics (small molecules and genes) incorporated in a surrounding lipid layer⁶². Higher powers of ultrasound can be used to cavitate microbubbles and release the attached therapeutic locally. These microbubbles, however, can only carry limited therapeutic doses on their surface, have a short echogenic lifetime in vivo (~minutes), are typically micron-sized, are rapidly taken up by the RES, and cannot extravasate.

In photodynamic therapy (PDT), a tumor-homing porphyrin molecule is used, which produces cytotoxic singlet oxygen when excited by incident light⁶³. Due to the short lifetime of singlet oxygen (<0.04ms), the radius of action is small (<0.02um) and the damage is to a specific subcellular site, typically lysosomes, cell membrane and mitochondria. Porphyrins home to tumors due to their lipophilic nature and low tumor pH, though they have also been conjugated to antibodies for targeting⁶⁴. A major

drawback, however is that the light (UV is optimum, but red is also used clinically) used to excite most porphyrins does not penetrate deep tissue, limiting PDT to accessible lesions. While fiber optic delivery of incident light enables deeper treatment (and treatment of the gastrointestinal tract and esophagus), minimizing invasiveness is a limiting concern.

While UV and visible light does not penetrate tissue significantly, near-infrared (NIR) wavelengths (700-900nm) have been used to heat particles in tissue. In this frequency regime, the absorption of light by water (and tissue chromophores) is reduced. Gold nanoshells (coating a silica nanoparticle) can be tuned to absorb strongly in this range⁶⁵. When these particles are concentrated in a tumor, incident light leads to therapeutic thermoablation, which has been shown to arrest tumor growth¹⁸. Due to their size (120-200 nm), the particles passively accumulate in areas of “leaky” vasculature, such as tumors but also in the liver. Attempts to target these particles have proven difficult, due to their large size. While tissue absorption of NIR light is improved over visible wavelengths, scattering losses would prevent treatment of deep-seated tumors (greater than ~1cm from the surface).

Unlike light, x-rays penetrate deep tissue significantly. High atomic number (Z) materials, such as iodine or gold, provide dose enhancement by locally enhancing x-ray absorption. If high-Z materials selectively accumulate in a tumor, differential absorption leads to tumor damage while limiting effects on normal tissue. In one study, gold nanoparticles were injected i.v. in tumor-bearing mice, with ~5% of the injected dose accumulating in the tumor⁶⁶. Subsequent irradiation resulted in decreased tumor volume and increased survival. Yet, differential absorption is a function of the amount of high-Z material. Unless a high concentration (>1%) of particles accumulate in the tumor, differential absorption is insignificant. In this case, 1.8% gold by weight resulted in a dose increase of 550%. Achieving these high

concentrations required a large injected dose (2.7 g Au/kg), which can damage other tissues.

On the opposing end of the electromagnetic spectrum, fields in the range of kHz to MHz penetrate deep tissue as well. Fields in this range will induce eddy currents in conductive materials, generating heat. Additionally, if the material is magnetic, hysteresis effects produce heat as the magnetic dipole of the material attempts to align with the external field. A highly-cited recent study utilized the first of these effects to heat 1.4nm gold nanoparticles⁶⁷. The group claimed they could locally heat the particle's surface (and unwind double-stranded DNA), without raising the temperature of the surrounding medium. We believe, however, that some of their results are an artifact, generated by electromagnetic interference between the applicator coil and spectrophotometer. While induction is a highly effective means of heating larger objects (for industrial welding, for example), power absorption scales with diameter, leading to ineffective heating at the nanoscale. Hysteresis heating of magnetic materials, on the other hand, depends not on the size of individual particles, but the density of magnetic material (iron, in many cases). While a single particle cannot be heated or "actuated", a collection of particles in a defined volume can generate heat in that volume, which can lead to local, heat-induced actuation⁶⁸. In addition, tissue absorption (and thus heating) with ~300-500 kHz fields is negligible, enabling the treatment of deep tumors without collateral heating. For these reasons, we have chosen to investigate actuation of magnetic nanoparticles using externally applied AC fields.

When the direction of an applied field alternates, both Brownian and Neel relaxation of the magnetic moment contribute to heat generation in single domain nanoparticles^{69, 70}. In the Brownian case, the moment is locked to the crystal axis, requiring a rotation of the particle to align with the applied field. This rotation against

a viscous media generates frictional heating. For Neel relaxation, the magnetic moment rotates within the crystal. In this case, energy is dissipated as the moment relaxes to its equilibrium orientation. In multidomain particles (ferrite > 100 nm), heating is dominated by domain wall shifting, and the energy loss is related to the area within the hysteresis loop. These hysteresis effects, however, do not occur in single domain, superparamagnetic nanoparticles.

Several groups have utilized these effects for cancer hyperthermia (investigated since the late 1950s), but most notably Jordan and coworkers^{69, 71-73}. Termed magnetic fluid hyperthermia (MFH), their system involves the injection of non-targeted, aminosilane-coated iron oxide (relying on passive tumor uptake) and a specialized applicator for local field application⁷⁴. Feasibility has been shown in vitro and in tumor-bearing animals. In March 2003, phase I/II clinical trials for treatment of glioblastoma began in Germany, and trials for prostate and other focal cancers is now underway. Preliminary results indicate a 50% response rate.

While higher levels of heating (>47°C), termed thermoablation, typically leads to protein denaturation, moderate hyperthermia (42-45°C) induces an abundance of cellular effectors, which mediate cell death⁷⁵. These include: changes in the fluidity/stability/potential of the cell membrane, impaired intracellular transport, alteration of signal transduction pathways and impairment of protein/nucleic acid synthesis. At lower temperatures, cell death tends to occur through apoptosis, but is necrotic at higher temperatures (>43°C). Hyperthermia also leads to activation of heat shock protein (hsp), inducing T-cell activation against the tumor. Hsp expression, however, can also lead to resistance to other hyperthermia effects in subsequent doses. On a tissue level, hyperthermia decreases tumor blood flow, reducing oxygen and nutrient supplies.

Studies have shown that conventional hyperthermia (convective heating) in combination with chemotherapy or radiotherapy amplifies the effectiveness of these therapies alone. Several phase III clinical trials, tandem application (sequential application is less effective) of radiotherapy with hyperthermia has led to positive results⁷⁶. For this application, heating interferes with DNA repair processes, preventing cancer cells from repairing DNA-damage induced by radiation. For several chemotherapeutics, thermal enhancement has been demonstrated in animal tumor models⁷⁵. In human trials, combination of cisplatin with regional hyperthermia led to a 70% response in children with recurrent germ cell tumors⁷⁷. These findings present a unique opportunity for a multifunctional therapeutic, where heat-triggered drug release leads to amplified effects.

1.6 In this thesis

In this thesis, we focus on three unsettled issues central to the progress of multifunctional nanoparticles. First, as many therapeutics act on proteins or nucleic acids in the interior of the cell, intracellular delivery, free of the endolysosomal pathway, is essential. Particles, however, are generally not membrane permeable, and must be actively transported inside cells. Second, the use of newly-developed inorganic nanomaterials in vivo requires investigation into their biocompatibility and cytotoxicity. Nanoparticle fate, after delivery and imaging have been performed, must be considered. Finally, the unique physical properties of these nanomaterials may enable exciting clinically-relevant functions, especially the ability to remotely actuate nanoparticles after delivery in vivo. We have developed a scheme to trigger therapeutic release from outside the body. Throughout our work, we have developed these biologically-relevant functions in a modular manner, so that they can be investigated individually before combination in a single particle. These units have

been built onto scaffolds with an inorganic nanoparticle core, composed of semiconductor QDs or iron oxide nanocrystals.

In chapter two, we investigate strategies to improve the cellular uptake of nanoparticles for subcellular imaging and therapeutic delivery. Using semiconductor quantum dots (QDs) as a model nanoparticle scaffold, we investigated various means of delivery borrowed from gene delivery. We found that complexing QDs with cationic liposomes significantly increases the particle uptake. Additionally, particles no longer co-localize with an endosome marker, indicating they have reached the cytoplasm. The QDs, however, are aggregated in the cytoplasm. Microinjection delivers monodisperse particles to the cytoplasm, which can then be directed to various organelles by attaching a localization sequence peptide. In chapter three, we worked to incorporate siRNA into the delivery scheme. Taking advantage of the large surface area of cationic liposomes, we co-complexed this reagent with both QDs and siRNA. While the two were not directly linked, we found the fluorescence of an individual cell correlates with the amount of siRNA delivered to that cell, enabling sorting into populations of high delivery and knockdown. Finally, in chapter four, we developed a strategy to bypass the use of the cationic liposome, which would allow the co-delivery of siRNA and QDs *in vivo*. Here, we tethered the siRNA directly to the surface of QDs and co-attached a tumor targeting peptide to improve accumulation. This multifunctional particle now contains imaging, drug delivery, and tumor targeting features in a package small enough to allow systemic targeting.

Along the way, we began to question the potential cytotoxicity of these cadmium-containing QDs, and explored this possibility in chapter five. We found that the CdSe core is prone to oxidation and released toxic Cd ions when disrupted. Inorganic (ZnS) and organic capping layers minimize this oxidation, however, and render the particles safe for *in vitro* use and animal experimentation. To demonstrate, we used QDs to

track the reorganization of micropatterned hepatocytes over 7 days in culture with no effects on viability or function. Clinical use of these particles, however, will require further investigation and perhaps alternate core materials. In the meantime, other inorganic particles exist which may be more useful in a clinical setting. Dextran-coated iron oxide particles, for example, have been approved by the US FDA as contrast agents for MR imaging.

In chapter six, we investigated a means to remotely actuate these iron oxide particles with the extracorporeal application of electromagnetic fields (EMF). When applied to magnetic particles, radiofrequency EMF leads to local heating, which can be used to disrupt a heat-labile bond and release a payload. We attached a single stranded oligonucleotide to the particle's surface, and conjugated fluorescent dyes (as model drugs) to a complementary strand. Combining the two components leads to self-assembly of dye-laden particles, and the application of EMF triggers dye release. By tuning the EMF and duplex melting point, selective release of multiple moieties is possible. Triggered release of this sort may be beneficial for customizing chemotherapy, multistage therapies, and reducing collateral damage to non-diseased tissues.

CHAPTER 2

INTRACELLULAR DELIVERY OF QUANTUM DOT BIOCONJUGATES

2.1 Abstract

In this study, we explored several strategies borrowed from the field of gene delivery to enhance delivery of QDs to the interior of live cells. To traffic QDs to subcellular organelles, we then derivatized QDs with known peptide localization sequences. Thus, using microinjection of QD-PEG-peptide conjugates, we demonstrated the ability to target QDs to subcellular sites such as the nucleus and mitochondria.

2.2 Introduction

The ability to fluorescently tag and track subcellular structures in living cells represents a powerful tool in cell biology. While the time scale of observation for conventional organic dyes is limited due to photobleaching, semiconductor quantum dots (QDs) have surfaced as a bright, photostable alternative¹. Furthermore, the emission properties of QDs can be tuned by size and composition, permitting the synthesis of a large set of probes to monitor many dynamic processes occurring inside living cells simultaneously. A key challenge, however, in the use of QDs for intracellular tracking is the delivery of QDs to the cytoplasm and organelles such as the nucleus and mitochondria. While organic dyes used to label these organelles (DAPI, Mitotracker) are able to permeate cell membranes, the size and surface

properties of QDs prevent passive diffusion across the lipid bilayer. Several groups have demonstrated the use of receptor-mediated endocytosis for intracellular delivery of QDs, but all have found that QDs entering cells by this pathway remain sequestered in endocytic vesicles, preventing the labeling of other intracellular structures^{51, 78, 79}. As an alternative, one study reported the use of microinjection as a means of introducing QDs into the cytoplasm, but only to track populations of cells and not for the investigation of intracellular events⁴². Furthermore, QDs have yet to be targeted to specific organelles, proteins, or nucleic acids inside living cells to observe subcellular events. As progress is made towards the goal of real-time, multiplexed analysis of living cells, there is a need to: (1) explore alternative strategies for delivering QDs into cells, (2) develop methods to characterize and compare delivery schemes, and (3) investigate targeting strategies for labeling subcellular compartments.

2.3 Materials and Methods

2.3.1 Quantum Dot preparation

CdSe/ZnS nanocrystals were synthesized^{17, 80} and water-solubilized with mercaptoacetic acid (MAA)⁷⁸ as previously described. Green (550nm emission maxima, 40nm FWHM) and red QDs (630nm emission maxima, 38nm FWHM) were used for these experiments. For PEG-QDs, Methoxy polyethylene glycol amine (mPEG-NH₂-5000MW) (Shearwater) was reacted with equimolar 2-iminothiolane (Sigma) to add a thiol group, and then conjugated directly to MAA-QDs via a thiol exchange reaction¹. For EGF-QDs, Epidermal Growth Factor (EGF, BD) was thiolated with equimolar 2-iminothiolane and reacted with PEG-QDs at room temperature for several hours. The NLS peptide, NH₂-CSSDDEATADSQHSTPPKKRKY-COOH, and MLS peptide, NH₂-

MSVLTPLLLRLGLTGSARRLPVPRAKIHC-CONH₂, were commercially synthesized (Global Peptide).

2.3.2 Transfection Agent Assisted QD Labeling

Transfection reagents from three different classes were used – cationic liposomes (Lipofectamine 2000, Invitrogen), activated dendrimers (Superfect, Qiagen), and translocation peptides (Chariot, Active Motif). The reagents were applied to cells based on the manufacturer's instructions for DNA/protein transfection. Briefly, 10 μ L of transfection reagent in DMEM and 15 μ g of QDs in DMEM were used for each 35 mm well (80% confluent) and allowed to complex. For Chariot, the protocol was altered slightly (6 μ L reagent in water complexed with QDs in PBS). The QD/reagent solutions were diluted in DMEM (to 1 mL per well) and incubated with the cells. Six hours later, the transfection media was removed and DMEM with 10% FBS and pen/strep was added. Approximately 6 hours later, the cells were trypsinized and prepared for flow cytometry or replated on glass coverslips for imaging. All cell images were captured by a cooled CCD camera (CoolSnap HQ, Roper Scientific) and processed on MetaVue software (Universal Imaging). Flow cytometry was performed on a FACSCalibur (BD Biosciences) with a 488 nm Ar laser. Signal from the FL1 bandpass emission (530/30) was used for the green QDs and WinMDI software (<http://facs.scripps.edu>) was used to generate population histograms.

2.3.3 Electroporation

A BTX 600 electro cell manipulator was used to deliver PEG QDs to HeLa cells. Several critical parameters were identified: temperature, electroporation solution, charging voltage, and pulse length (determined by resistance and capacitance of pulsing circuit). To ensure that endocytosis would not occur, we performed most of

the experiments at 4°C (though studies at 22°C were also performed). For the electroporation solution, we used tested phosphate-buffered saline (PBS), Krebs Ringers Buffer (KRB), serum-free DMEM, and a low conductivity, isotonic HEPES-buffered glucose solution. Low conductivity solutions required longer pulse lengths as expected (time constant = 1/RC). In all four solutions, charging voltages of 100-200V and 1-5ms pulse lengths did deliver QDs to the cell's interior (though these QDs were not monodisperse). Optimal intracellular delivery without extensive cell death (greater than 50% viability) occurred in Phosphate Buffered Saline (PBS) with a single 100-200V, 1-5ms pulse (see **Table 2.1**). Approximately 10^6 cells were suspended in 400uL of PBS with 250 ug/mL QDs. The electroporation charge was applied, and, after ten minutes, the cells were pelleted to remove the QD solution, and then plated on coverslips.

Table 2.1: Optimization of electroporation parameters for HeLa cells in PBS.

Settings marked “+” resulted in delivery of intracellular aggregates. “+/-” indicates that some internalization occurred, but few nanoparticles were seen inside the cells, compared with other settings. “D” indicates that greater than 95% of the cells were killed in the electroporation process. “*” indicates that large aggregates of QDs were seen in the solution following electroporation (and few were seen inside the cells).

		Pulse length (ms)				
		0.5	1	5	10	20
Voltage (V)	100	+/-	+/-	+	+	+/-
	200	+/-	+	+	D	D
	300	+	+/-/D	D		
	400	+	+/-/D	D		
	500	*	D			

2.4 Results and Discussion

With the goal of identifying an improved delivery scheme for intracellular tracking, we studied both biochemical (translocation peptides, cationic liposomes, dendrimers) and physical methods (electroporation and microinjection) of delivering QDs into cells. These approaches are commonly used for oligonucleotide delivery; however they have not been explored for delivery of semiconductor nanocrystals despite obvious similarities in size (~nm) and charge (negative). In order to compare these techniques qualitatively and quantitatively, we combined the use of epifluorescence microscopy to evaluate intracellular QD localization in single cells with flow cytometry to quantify the delivery efficiency over a population of live cells. To explore these methods, we coated the nanoparticles with poly(ethylene)glycol (PEG) – an inert coating that minimizes cellular uptake through endocytosis⁷⁸, likely by preventing non-specific attachment to the cell surface, unlike other QD coatings such as silica and DHLA^{51, 79}. **Figure 2.1A** depicts a composite (fluorescence/phase) micrograph verifying the lack of internalization of PEG-coated QDs by direct incubation with HeLa cells (middle). Dimly fluorescent aggregates are qualitatively visible on the extracellular border. This non-specific labeling was quantified using flow cytometry, where the median cell fluorescence was measured as approximately 6-fold over background (Fig 1A, right). Furthermore, this non-specific binding was fairly uniform across a population of one million cells as indicated by the width of the cytometry peak. In comparison, QDs that were complexed with transfection reagents (translocation peptide, cationic liposome, dendrimer) prior to incubation with cells were internalized (**Figure 2.1B** – left, middle). The internalization was verified by confocal microscopy, visualizing the membrane with 5,5'-Ph₂-DiIC₁₈ (Molecular Probes), a fluorescent lipophilic dye (data not shown). Flow cytometry allowed

quantification of relative labeling efficiency and distribution across the cell population (**Figure 2.1B** – right). Median fluorescence was highest for cationic liposomes (349 a.u.) followed by dendrimers (88 a.u.). Note that the median fluorescence for the QD-translocation peptide complexes (20 a.u.) was unexpectedly lower than uncomplexed QDs (QDs alone, 52 a.u.), possibly due to increased scattering and quenching effects of intracellular QD aggregates compared with a disperse, extracellular fluorescence. In this case, epifluorescent microscopy provided complementary data to cytometry by indicating internalization of complexed QDs as compared to extracellular localization with uncomplexed QDs. Staining with a membrane dye and observation of the cells with a confocal microscope further confirmed the particles were internalized (**Figure 2.2**). Thus, a combination of flow cytometry and microscopy enabled the qualitative and quantitative comparison of QD delivery strategies.

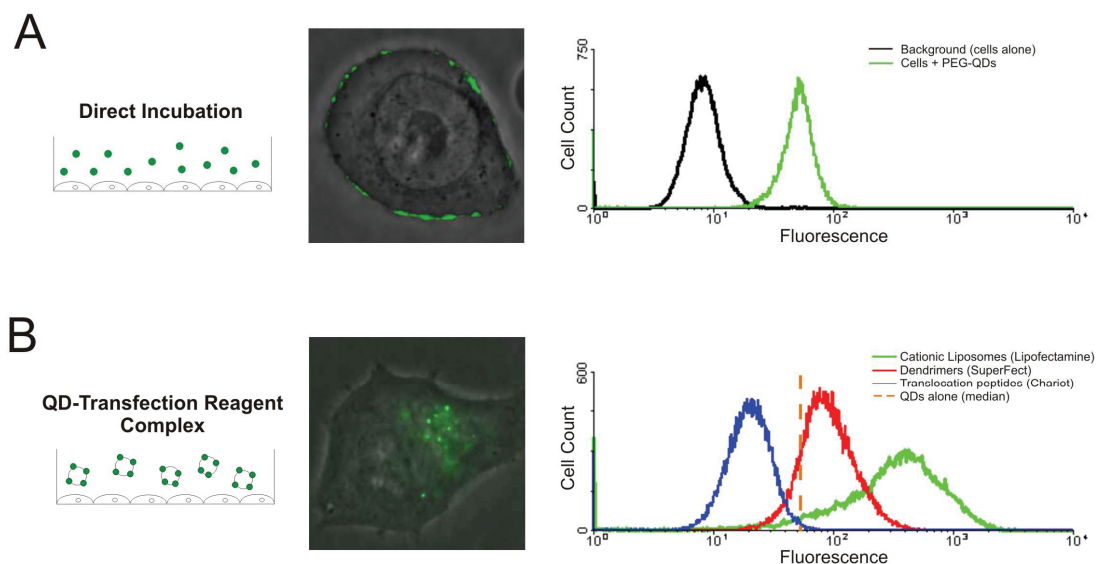


Figure 2.1 - Improved Intracellular QD Delivery Quantified by Flow Cytometry
 (A) Incubation of PEG-coated QDs with HeLa cells. Fluorescence/phase overlay micrograph of QDs on HeLa cells depicts dim, extracellular aggregates (middle). Flow cytometry of cells incubated with QDs (green curve) as compared to unlabeled cells (black) demonstrating ability to quantify labeling efficiency (right). (B) In contrast, QDs complexed with three different transfection reagents are delivered to the interior of HeLa cells (middle). Flow cytometry (right) showed higher labeling efficiency of cationic liposomes (green) than dendrimers and translocation peptides (red, blue). Orange line indicates median of cells alone (from A).

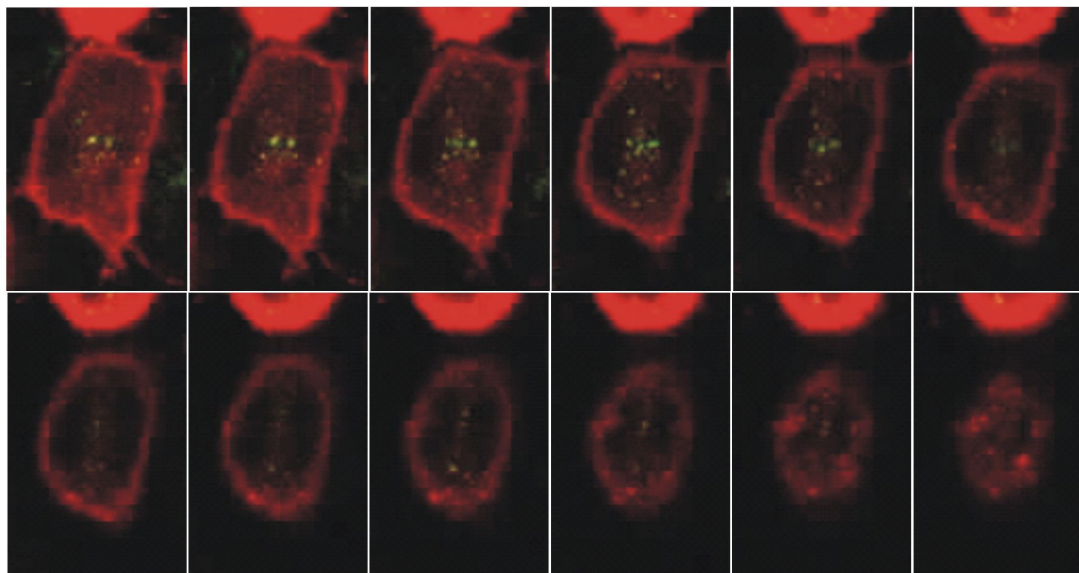


Figure 2.2 – Confocal imaging of QD/cationic liposome intracellular delivery. A Z-series of continuous sections (bottom to top) was taken of a cell incubated with green QD/cationic liposome conjugates. The cell membrane is labeled with 5,5'-Ph₂-DiIc₁₈, a membrane intercalating dye (shown in red). The images clearly show the green QDs inside the bounds of the cell's plasma membrane.

In our study, cationic liposomes provided the highest delivery efficiency of QDs to live cells. Though the mechanism of delivery has not been specifically investigated in detail, we suspect that QDs behave in a similar fashion to DNA during lipofection where DNA/liposome conjugates are formed extracellularly, endocytosed, and subsequently escape from the endosomal vesicle to access the cytoplasm⁸¹. Similarly, we propose that negatively-charged QDs complex with cationic liposomes due to electrostatic interactions. Transmission electron microscopy was used to visualize the complexes where a single liposome measuring 200 to 500 nm in diameter was coated with approximately 20 to 40 QDs (data not shown). Subsequent cellular entry of the complexes was confirmed microscopically and may occur through endocytosis and endosomal escape as seen in DNA delivery. To determine whether intracellular QDs were trapped in endosomes or free in the cytoplasm, we conducted a multicolor QD experiment (**Figure 2.3A**). Green-emitting QDs were complexed with the transfection

agent and red-emitting QDs were coated by adsorption of epidermal growth factor (EGF) to promote endocytosis through the cell-surface receptor (EGFR)⁸². Incubation of EGF-coated QDs yielded red-emitting vesicular structures that were identified as a nearly complete subset (>95%) of the endolysosomal compartment by colocalization with a marker for acidic organelles (LysoSensor Blue) (**Figure 2.4**). In contrast, QDs complexed with cationic liposomes (green) yielded a significant percentage (>90%) of fluorescence emission that did not colocalize with the endolysosomal compartment (red), suggesting some escape from endocytic vesicles. In principle, once QDs are free in the cytoplasm, they could be utilized to track both whole cells and intracellular processes. However, in order to fully exploit the potential of intracellular QD labeling, well-dispersed QDs are imperative. Our studies indicate that while cationic liposomes do promote efficient delivery for live cell labeling, they also form QD aggregates of several hundred nanometers in diameter that would prevent normal trafficking to the nucleus or mitochondria^{83, 84}.

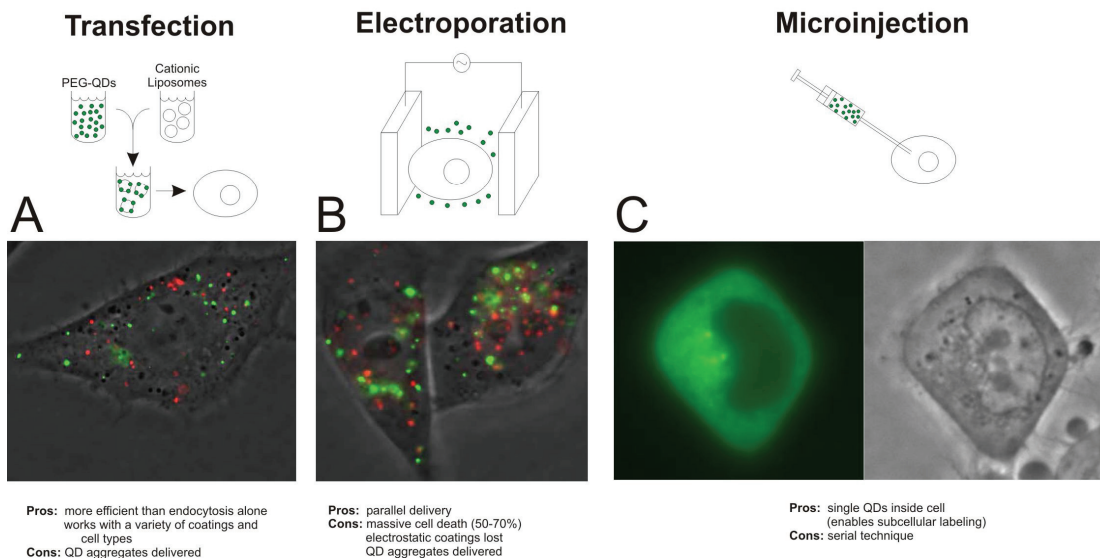


Figure 2.3 - Comparison of Delivery Methods – (A) Fluorescent/phase micrograph of HeLa cell transfected with green PEG-coated QDs (via complexation with cationic liposomes) and red EGF-QDs (as an endosomal label). (B) Fluorescent/phase micrograph of HeLa cell after electroporation in a solution of green QDs followed by incubation with red EGF-QDs as endosomal label. (A) and (B) depict aggregated QDs and significant lack of green/red colocalization consistent with endosomal escape. (C) Fluorescent (left) and phase (right) micrograph of HeLa cell 2 hours after cytoplasmic injection of green QDs. Diffuse cytoplasmic staining is consistent with non-aggregated QDs and nuclear exclusion (though fluorescence can be seen in focal planes above and below the nucleus).



Figure 2.4 – EGF-QDs colocalize with an endosome marker. HeLa cells were sequentially incubated with 20ug/mL red EGF-QDs (2h), 20ug/mL green EGF-QDs (2h), and 2uM LysoSensor Blue endosome dye (20 min), and imaged with a fluorescence microscope in red, green, and blue channels. From left to right – red channel, green channel, blue channel, merged fluorescence, and phase contrast. Nearly complete (>95%) colocalization of EGF-QDs (regardless of color) with the endosome marker suggest the QDs are endosomal.

In an attempt to deliver single, monodisperse QDs to the cell cytoplasm, we next explored the technique of electroporation. Generally used to deliver DNA to cells, electroporation temporarily generates hydrophilic pores in the plasma membrane by applying an electric field pulse. The pores allow the passive transport of DNA (or nanoparticles) into the cell⁸⁵. Although we expected that electroporation would deliver single QDs, we instead found that aggregates of up to 500 nm in diameter were delivered (**Figure 2.3B**, green QDs). We first suspected that the application of a high-energy electric field caused polarization of the QD surface, the loss of electrostatically-adsorbed surface ligands (PEG, mercaptoacetic acid) and subsequent QD aggregation as has been reported for QDs in aqueous solution upon loss of stabilizing ligand.⁸⁶ To test this possibility, we delivered QDs with a crosslinked bovine serum albumin (BSA) coat⁸⁷ (that is not prone to loss of stabilizing ligand) via electroporation, and still observed clumps of QDs both inside and outside the cells. These findings suggest that stabilization of surface ligand is not sufficient to prevent particle aggregation, and point to alternate mechanisms for aggregation. Interestingly, Golzio et al. reported that negatively-charged DNA plasmids also aggregate when entering cells during electroporation⁸⁸. They propose a model in which the electric field causes the formation of a complex between the plasmid (analogous to the nanoparticle, in this case) and the cell membrane, which is internalized when membrane resealing occurs. While the mechanism of particle aggregation remains to be determined, our data suggest that electroporation under conventional conditions is a robust tool for live cell labeling with aggregated, but not monodisperse QDs. Thus, electroporation may be best utilized as a delivery scheme in applications such as whole cell tracking and cytometry.

Using these two approaches (complexing with cationic liposomes and electroporation), we have demonstrated the ability to label a large population of cells

in parallel. Both techniques, however, deliver QD aggregates that are not ideal for intracellular assays. For single-cell labeling, microinjection is a superior approach, albeit serial, that enables delivery of QDs to the cell's interior in a monodisperse form. **Figure 2.3C** depicts the microinjection of PEG-QDs into the cytoplasm of a single cell, resulting in a diffuse cytoplasmic stain. Passive transport through the nuclear envelope is limited to substances 9nm or less in diameter⁸⁹, explaining the observed nuclear exclusion of the PEG-QDs (~28nm in diameter determined by dynamic light scattering (DLS)). To determine the length of time microinjected PEG-QDs remain monodisperse, images were taken at 30 min, 2h, and 24h timepoints (**Figure 2.5**). While the particles appear monodisperse at 2h, significant aggregation was observed at 24h.

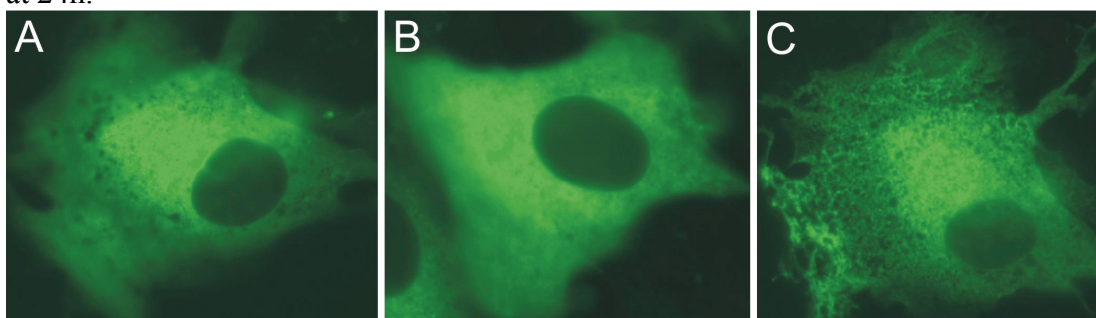


Figure 2.5 – Microinjection of PEG-QDs in 3T3 cells. Fluorescence imaging of the cells was performed at various times after microinjection: 30 min (A), 2h (B), and 24h (C). While QDs remain monodisperse at the 2h timepoint, significant aggregation is seen by 24h.

In order to explore the utility of monodisperse QDs for studying subcellular phenomena, we next synthesized ‘multi-functional’ QDs that combined narrow fluorescence emission with an inert coating (PEG) and a peptide localization sequence for delivery via microinjection. Our goal was to direct subcellular localization of the QDs by alteration of the peptide sequence, thereby enabling visualization of specific intracellular organelles. We specifically explored the use of a 23mer nuclear

localization sequence (NLS) peptide and a 28mer mitochondrial localization sequence (MLS peptide) to traffic QDs to the nucleus and mitochondria respectively. The NLS peptide contains the canonical 7mer (PKKKRKV) functional domain from the SV40 T antigen plus additional residues that have been shown to increase nuclear accumulation⁹⁰. This peptide recognizes the nuclear transport protein importin (karyopherin) alpha, leading to active transport through the nuclear pore complex⁸³. Gold colloids as large as ~39nm in diameter have been transported into the nucleus in this manner⁹¹, and the ~25nm diameter PEG-QD+NLS conjugate (measured by DLS) is well below this threshold. The MLS consists of the targeting presequence from human cytochrome oxidase subunit VIII (COX8), a protein that is synthesized in the cytoplasm and actively transported into the mitochondria^{84, 92}. Each of these peptides was synthesized to contain a free cysteine residue, whose sulfhydryl group allowed electrostatic adsorption to the QD surface. **Figure 2.6A** depicts the successful nuclear localization of the NLS-conjugated QDs as compared to the cytoplasmic distribution of the rhodamine-dextran (70 kDa MW) control 18 h after microinjection. Comparison in nuclear localization of NLS-conjugated PEG QDs to cytoplasmic localization PEG QDs alone (**Figure 2.3C and Figure 2.5**), supports the conclusion that adsorption of the NLS peptide is sufficient to specify nuclear trafficking. Similarly, MLS-conjugated QDs were observed around mitochondria by 18 h as indicated by colocalization of QDs with an organic mitochondrial dye that readily permeates the cell membrane and accumulates due to a thiol-reactive chloromethyl moiety (MitoTracker Red) in **Figure 2.6B**⁹³. For both peptides, significant localization of QDs occurred by 30 minutes, and additional accumulation occurred over 2 and over 18 hours, and no further changes were observed through 24 hours. While these localization kinetics are slower than previous reports of DNA delivery to the nucleus (5-30 minutes)⁹⁰, they are consistent with the time scale of cytoplasmic

transport of larger complexes such as intact adeno-associated viruses (~90nm)⁸⁹, reflecting that size plays a role in localization kinetics. For these viruses, perinuclear accumulation begins within 30 minutes, and significant intranuclear accumulation of the smaller inner core occurs by 2 hours. Thus, possible reasons for the prolonged localization of QD bioconjugates relative to biomolecules include: their relative size, as well as suboptimal live cell microscopy conditions (repeated exposure to room temperature and basic pH due to CO₂ buffering), and an excess of free localization peptide competing with QD conjugates for a fixed number of transporters. In the current report, our goal was to demonstrate proof-of-principle for use of signaling peptides to traffic quantum dot nanoparticles; however, in the future, the subcellular localization kinetics of nanoparticle bioconjugates merits further study.

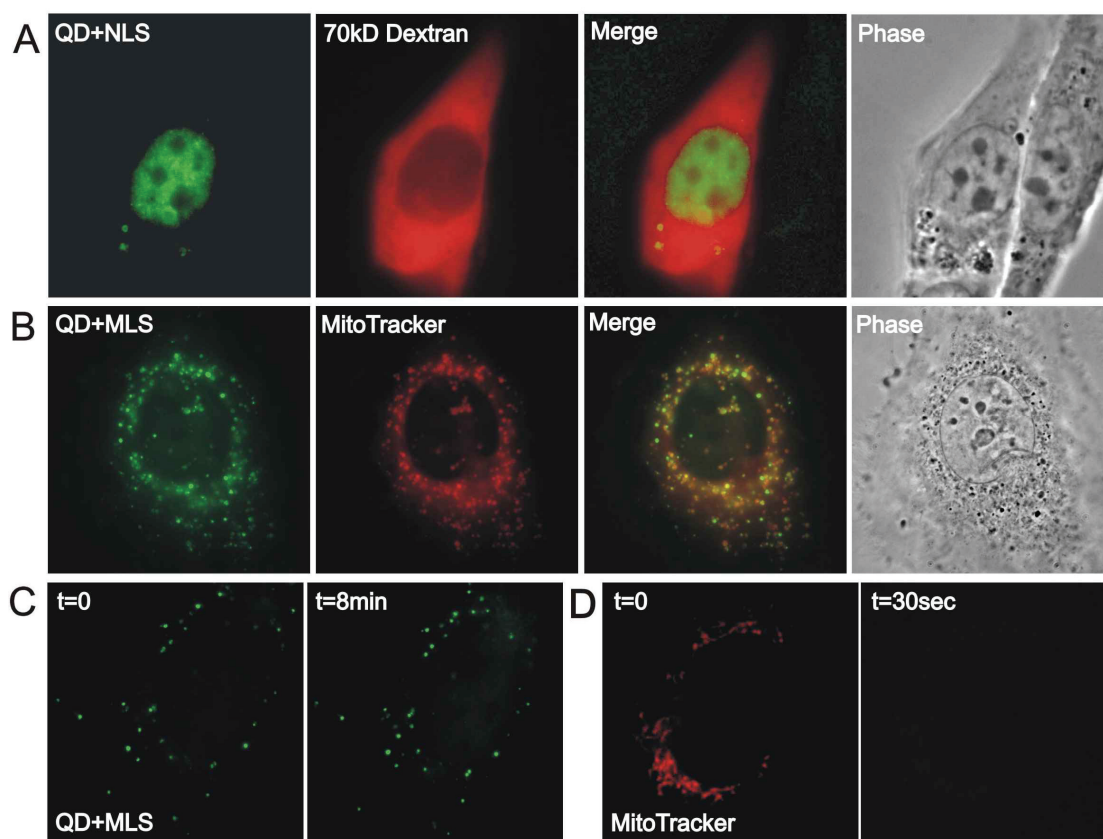


Figure 2.6 - Subcellular Localization of Single QDs – PEG-QDs were conjugated to localization sequence peptides, which permit active transport to the nucleus. (NLS, A) or mitochondria (MLS, B), and were delivered to 3T3 fibroblast cells by microinjection. (A) Fluorescent and phase micrographs of HeLa cell 24 h after co-injection of NLS-QDs with 70kDa rhodamine dextran control. The four spots in the nucleus that are not stained with QDs are the nucleoli, and are also seen on the phase image. (B) Fluorescent and phase micrographs 24 h after injection of MLS-QDs. Colocalization with Mitotracker Red confirms mitochondrial labeling. (C) QDs remain fluorescent after 8m of continuous mercury lamp exposure, while conventional MitoTracker dye (D) bleaches beyond detection after 30s of continuous excitation. Different cells were imaged for (C) and (D).

Finally, in order to demonstrate the feasibility of tracking organelles without photobleaching limitations, we monitored labeled mitochondria in live cells over eight minutes of continuous exposure with no measurable loss in signal intensity (**Figure 2.6C**). In comparison, dye-labeled mitochondria photobleached beyond detection in less than 30 seconds (**Figure 2.6D**). Collectively, these experiments demonstrate

that the use of peptide localization sequences and PEG coating in conjunction with microinjection enable the delivery and subcellular localization of QDs in live cells. The appropriate intracellular trafficking of conjugated QDs is consistent with the persistence of both PEG (required to prevent aggregation) and localization peptides (required for targeting) on the QD surface even in the intracellular biochemical milieu, thereby suggesting that adsorption of a thiolated peptide is an adequate method of QD conjugation for at least some intracellular assays.

2.5 Conclusion

In conclusion, we have explored and characterized several strategies to enhance delivery of QDs to live cells using epifluorescent microscopy and flow cytometry. Endocytosis of QDs results in sequestration of the majority of QDs in the endolysosomal compartment where they are unavailable for subsequent intracellular assays. Delivery of QD/cationic liposome complexes and electroporation are efficient schemes to deliver QDs to the cytoplasm of a large population of cells; yet QDs form large aggregates that can restrict subsequent trafficking (e.g. passage through nuclear pores). In contrast, microinjection delivers QDs to the cell interior as monodisperse nanoparticles, but requires each cell to be individually manipulated. Using microinjection of QD-PEG-peptide conjugates, we demonstrated the ability to target QDs to subcellular sites using known localization sequences. In fact, a plethora of localization sequences exist to extend our findings to the labeling of other organelles (endoplasmic reticulum, golgi, peroxisomes, etc). Moving forward, the ability to deliver and target QDs to intracellular sites will help to realize the promise of these versatile nanoparticles.

2.6 Acknowledgements

We thank Dennis Young for assistance with flow cytometry, Carolan Buckmaster for microinjection, and Mike Sailor for providing facilities for QD synthesis. Funding provided by DARPA-MTO, David and Lucile Packard Foundation, NIH T32 HL07089, NIH NDDK, University of Toronto (WC), the Connaught Foundation (WC), Canadian Foundation for Innovation (WC), and Ontario Innovation Trust (WC).

This chapter was reproduced in full from Derfus AM, Chan WCW, and Bhatia SN. "Intracellular Delivery of Quantum Dots for Live Cell Labeling and Organelle Tracking." *Advanced Materials* **16** (2004): 961-966. The dissertation author was the primary investigator and first author on the paper. He thanks Warren Chan and Sangeeta Bhatia for their significant contributions to the work.

CHAPTER 3

QUANTUM DOTS TO MONITOR SIRNA DELIVERY

3.1 Abstract

A critical issue in using RNA interference for identifying genotype/phenotype correlations is the uniformity of gene silencing within a cell population. Variations in transfection efficiency, delivery-induced cytotoxicity, and ‘off target’ effects at high siRNA concentrations can confound the interpretation of functional studies. To address this problem, we have developed a novel method of monitoring siRNA delivery that combines unmodified siRNA with semiconductor quantum dots (QDs) as multicolor biological probes. We co-transfected siRNA with QDs using standard transfection techniques, thereby leveraging the photostable fluorescent nanoparticles to track delivery of nucleic acid, sort cells by degree of transfection, and purify homogeneously-silenced subpopulations. Compared to alternative RNAi tracking methods (co-delivery of reporter plasmids, end-labeling the siRNA), QDs exhibit superior photostability and tunable optical properties for an extensive selection of non-overlapping colors. Thus this simple, modular system can be extended toward multiplexed gene knockdown studies, as demonstrated in a two-color proof-of-principle study with two biological targets. When the method was applied to investigate the functional role of T-cadherin in cell-cell communication, a subpopulation of highly silenced cells obtained by QD labeling was required to observe significant downstream effects of gene knockdown.

3.2 Introduction

RNA interference (RNAi) has emerged as a powerful tool for studying gene function. Since the discovery of RNAi⁹⁴, the evolutionarily conserved cellular process has been exploited to determine the functions of nearly every gene in model organisms *C. elegans*^{95, 96} and *D. melanogaster*⁹⁷ and a host of mammalian genes including approximately 23% of the sequenced human genes^{57, 98}. If the RNAi effector sequence is potent and the siRNA delivered efficiently throughout the cell culture, remarkably specific post-transcriptional inhibition of gene expression can be achieved^{7, 99}. However, inefficient and heterogeneous delivery of siRNA is frequently observed in cell cultures, causing variable levels of gene silencing and potentially confounding the interpretation of genotype/phenotype correlations¹⁰⁰⁻¹⁰³. Without the means to address and resolve transfection variability, the utility of RNAi in eukaryotes will be limited only to mammalian cell types that have been thoroughly optimized for siRNA delivery¹⁰⁴.

The importance of high transfection efficiency has been spotlighted among numerous reports investigating methods to either improve RNAi delivery¹⁰⁵⁻¹⁰⁸ or screen for efficient knockdown. In the latter case, typical strategies involve monitoring fluorescently end-modified siRNAs^{109, 110} or co-transfecting reporter plasmids and selecting for high transfection by fluorescence or antibiotic-resistance¹¹¹. These techniques enable one-time selection of highly transfected cells yet discard moderately-silenced cells, which may be of interest to the study. For example, varying degrees of RNAi-mediated downregulation in the tumor suppressor gene *Trp53* have been shown to modulate expression of distinct pathological phenotypes both in vitro and in vivo¹¹². Moreover, rapid photobleaching of organic fluorophores and the limited selection of available reporters currently prevent RNAi tracking from

being feasible in either long-term or multiplexed studies. The dyes commonly used to label siRNAs lose over half the intensity of fluorescent signal in 5-10 seconds^{47, 49}. Meanwhile, fluorescent reporter plasmids, although meant to be continuously expressed by the cells, can require as long as 2 hours after transcription for the functional protein to be observable³⁵. Perhaps most importantly, due to the limited availability of fluorophores and reporter proteins that have non-overlapping emission spectra, current transfection screening methods are incapable of simultaneous monitoring of multiple siRNA molecules.

In this study, we demonstrate a novel means of monitoring nucleic acid delivery using standard transfection techniques to co-deliver semiconductor quantum dots (QDs) along with siRNA. QDs are bright, photostable CdSe/ZnS fluorescent nanocrystals that exhibit tunable emission properties for a wide range of color possibilities. We and others have shown that QDs can be rendered non-cytotoxic¹¹³ and innocuous to normal cell physiology and common cellular assays, such as immunostaining and reporter gene expression¹¹⁴. Combining QDs with siRNA for RNAi tracking requires neither chemical labeling of siRNA, which is costly and can potentially deter complexing with RISC, nor the expression of reporter plasmids. QDs are also brighter than most conventional fluorescent dyes by approximately 10-fold^{2, 49} and have been significantly easier to detect than GFP among background autofluorescence *in vivo*². Furthermore, QDs are far less susceptible to photobleaching, fluorescing more than 20 times longer than conventional fluorescent dyes under continuous mercury lamp exposure¹¹⁵. Using our QD/siRNA co-delivery technique, we found that cellular fluorescence correlated with level of silencing, allowing collection of a uniformly silenced cell population by fluorescence-activated cell sorting (FACS). The superior brightness and photostability of these probes in cells sustained not only FACS, but also live imaging, and immunostaining procedures.

With two QD colors and two siRNAs as a model, we also demonstrate the method's unique ability to generate cell populations with multiplexed levels of knockdown. Finally, we show that a homogenous silenced cell population generated using this method is essential to observing the phenotypic effects of decreased T-cadherin protein expression on cell-cell communication between hepatocytes and non-parenchymal cells.

3.3 Materials and Methods

3.3.1 Short interfering RNA and Quantum Dot Preparation

Pre-designed siRNA was used to selectively silence the Lamin A/C gene (*Lmna* siRNA #73605, NM_019390, Ambion) and the T-cadherin gene (SMARTpool reagent CDH13, NM_019707, Dharmacon). Fluorescently-labeled *Lmna* siRNA purchased from Dharmacon was designed with a fluorescein molecule on the 5' end of the sense strand. The annealed sequences were reconstituted in nuclease-free water and used at a concentration of 100 nM (*Lmna* siRNA, 5'-Fluorescein-*Lmna* siRNA) or 50 nM (T-cad siRNA).

Green (560 nm emission maxima) and orange (600 nm emission maxima) CdSe-core, ZnS-shell nanocrystals were synthesized and water-solubilized with mercaptoacetic acid (MAA) as previously described^{44, 78, 80}. MAA-QDs were then surface-modified by reacting with polyethylene glycol (PEG)-thiol MW 5000 (Nektar) overnight at room temperature. Excess PEG-thiol was removed by spin filtration (100kDa cutoff). QDs are also available commercially as an alternative to synthesis (Quantum Dot Corporation, Evident Technologies). Unless stated otherwise, 5 μ g PEGylated QD was used per cell transfection.

3.3.2 Fibroblast Cell Culture and Transfection

3T3-J2 fibroblasts were provided by Howard Green (Harvard Medical School, Cambridge, MA)¹¹⁶ and cultured at 37°C, 5% CO₂ in Dulbecco's Modified Eagle Medium (DMEM) with high glucose, 10% fetal bovine serum (FBS), and 1% penicillin-streptomycin. The transfection procedure was performed using Lipofectamine 2000 (Invitrogen) according to the manufacturer's instructions. Briefly, 3T3 fibroblasts were plated 24h prior to transfection at a density of 3×10^6 cells per 35-mm well, in antibiotic- and serum-free medium. Lipofectamine reagent (5 μ l) and either siRNA or QDs were diluted in Dulbecco's Modified Eagles' Medium (DMEM) and complexed at room temperature. For QD/siRNA co-complexes, siRNA and liposomes were allowed to complex for 15 min prior to an additional 15 min incubation with QDs. Complexes were added to cell cultures in fresh antibiotic- and serum-free medium until 5h later, at which time the cultures were washed and replaced with regular growth medium. Approximately 24h post-transfection, cells were trypsinized and prepared for flow cytometry.

3.3.3 Fluorescence Activated Cell Sorting (FACS)

Flow cytometry and sorting was performed on a FACS Vantage SE flow cytometer (Becton Dickinson) using a 488 nm Ar laser and FL1 bandpass emission (530 ± 20 nm) for the green QDs, FL3 bandpass emission (610 ± 10 nm) for the orange QDs. Fluorescence histograms and dot plots were generated using Cell Quest software (for figures, histograms were re-created using WinMDI software, <http://facs.scripps.edu>). Cell Quest was also used to gate populations of highest and lowest fluorescence intensity for sorting into chilled FBS. Sorted populations were immediately re-plated into separate wells containing regular growth medium and

allowed to adhere. Cells were incubated at 37°C until visualized by fluorescence microscopy or until assayed for protein level.

3.3.4 Western Blotting

Cell cultures were scraped and lysed in RIPA Lysis Buffer (Upstate Biotechnologies) supplemented with COMPLETE EDTA-free Protease inhibitor solution (Roche). Equal amounts (15-20 µg) total protein were loaded into 10% Tris-HCl resolving gel, separated by electrophoresis, and transferred to PVDF membrane. The blot was incubated in blocking solution (5% [w/v] nonfat dry milk, 200 mM Tris base [pH 7.4], 5 M NaCl, 5% Tween-20) for 1 h at room temperature, primary antibody overnight at 4°C, and secondary antibody for 1 h. Three washes in 200 mM Tris base pH 7.4, 5 M NaCl, 5% Tween-20 took place between steps and after completion of probing. Finally, the blot was visualized by chemiluminescence (Super Signal West Pico Kit, Pierce) and developed. Bands were analyzed for density using MetaMorph Image Analysis software (Universal Imaging) and normalized to loading control (β -actin) bands.

Primary antibodies used were polyclonal Lamin A/C antibody (Cell Signaling) at 1:1000 dilution in blocking solution and polyclonal β -actin antibody (Cell Signaling) at 1:750 dilution. T-cadherin primary antibody was a gift from Barbara Ranscht (University of California, San Diego)¹¹⁷. Secondary antibody was goat anti-rabbit IgG-HRP (Santa Cruz Biotechnology) at 1:7500 dilution. Blots were probed simultaneously for lamin A/C protein (70 kDa, 28 kDa) and β -actin protein (45 kDa); after detection, select blots were re-probed for T-cadherin (95 kDa).

3.3.5 Immunofluorescence Staining

Sorted and unsorted cells intended for Lamin nuclear protein immunostaining were seeded onto Collagen-I coated glass coverslips. Coverslips with attached cells were washed twice in cold phosphate-buffered saline (PBS, Gibco) and fixed in 4% paraformaldehyde at room temperature. After three brief PBS washes, cells were permeabilized with 0.2% Triton-X for 10 min at room temperature and washed again. The cells were blocked with 10% goat serum for 30 min at 37°C, incubated in primary antibody (1:100 Lamin A antibody, Santa Cruz Biotechnology) for 90 min at 37°C, washed three times with 0.05% Triton-X, incubated in secondary antibody (1:250 AlexaFluor 594 chicken anti-rabbit IgG antibody, Molecular Probes) for 1 h at room temperature, and washed a final three times. Antibody dilutions were performed in 1% bovine serum albumin (BSA) in PBS. Coverslips were mounted onto glass slides using Vectashield anti-fade medium (Vector Laboratories). Finally, nuclear staining was visualized and documented by phase contrast microscopy or epifluorescence (Nikon Eclipse TE200 inverted fluorescence microscope and CoolSnap-HQ Digital CCD Camera).

3.3.6 Hepatocyte/Fibroblast Co-cultures

Hepatocytes were isolated from 2-3 month old adult female Lewis rats (Charles River Laboratories) and purified as described previously^{118, 119}. Fresh, isolated hepatocytes were seeded at a density of 2.5×10^5 cells per well, in 17-mm wells adsorbed with 0.13 mg/mL Collagen-I. Cultures were maintained at 37°C, 5% CO₂ in hepatocyte medium consisting of DMEM with high glucose, 10% fetal bovine serum, 0.5 U/mL insulin, 7 ng/mL glucagons, 7.5 µg/mL hydrocortisone, 10 U/mL penicillin, and 10 µg/mL streptomycin. Twenty-four hours after hepatocyte seeding, fibroblasts from transfection experiments were co-cultivated at a previously optimized 1:1

hepatocyte:fibroblast ratio in fibroblast medium¹²⁰. Medium from hepatocyte/fibroblast co-cultures was collected and replaced with hepatocyte medium every 24h until completion of the experiment.

3.3.7 Hepatocellular Function Assays

Hepatocyte/fibroblast co-cultures were assayed for albumin production and cytochrome P450 enzymatic activity, prototypic indicators of hepatocellular function^{121, 122}. Albumin content in spent media samples was measured using an enzyme linked immunosorbent assay (ELISA) with horseradish peroxidase detection¹¹⁹. Cytochrome P450 (CYP1A1) enzymatic activity was measured by quantifying the amount of resorufin produced from the CYP-mediated cleavage of ethoxyresorufin *O*-deethylase (EROD)¹²³. Specifically, EROD was incubated with cell cultures for 30 min, media was collected, and resorufin fluorescence quantified at 571/585 nm excitation/emission.

Error bars represent standard error of the mean (n=3). Statistical significance was determined using one-way ANOVA (analysis of variance).

3.4 Results and Discussion

We used cationic liposomes to co-deliver green QDs and siRNA targeting the lamin a/c gene (*Lmna*) into murine fibroblasts, followed by flow cytometry to quantify intracellular QD uptake (**Figure 3.1A**). The median fluorescence of QD/siRNA-transfected cells compared to mock-transfected cells (liposome reagent only) and cells transfected with siRNA alone varied by approximately 84% (coefficient of variation). FACS was used to gate and collect the brightest 10% (high, H) of each fluorescence distribution, along with the dimmest 10% (low, L). After the sorted cells were replated and grown for 72 h to ensure protein turnover, protein expression analysis by

either Western blot or immunostaining was performed. In cells that had been co-transfected with siRNA and QDs, gene silencing correlated directly with intracellular fluorescence. Western blotting (**Figure 3.1B**) and image analysis of lamin a/c protein bands (**Figure 3.1C**) show approximately 90% knockdown in the highly fluorescent cells and negligible knockdown in the dimmest cells. The cells treated with siRNA alone exhibited mediocre gene down-regulation (20-30%) independent of sorting parameters. Consistent with the quantitative bulk protein assay, immunofluorescent detection of lamin nuclear protein in unsorted, siRNA-transfected cells produced heterogeneous staining throughout the cell population (**Figure 3.2A**). However, in the co-transfected case, the presence of green QDs correlated with consistently weak lamin immunofluorescent staining in the high co-transfected subpopulation (**Figure 3.2B**), compared to a lack of observable QDs and strong lamin staining in the low subpopulation (**Figure 3.2C**). Heterogeneous silencing therefore influences the accuracy of the bulk protein expression readout, suggesting the importance of verifying successful siRNA transfection for each gene knockdown study. Using QDs as photostable probes in combination with FACS, a subpopulation of uniformly-treated cells can be isolated, and also tracked with fluorescence microscopy over long periods of time. This may be useful for observing the protein upregulation and phenotypic responses of cells to gene regulation over time.

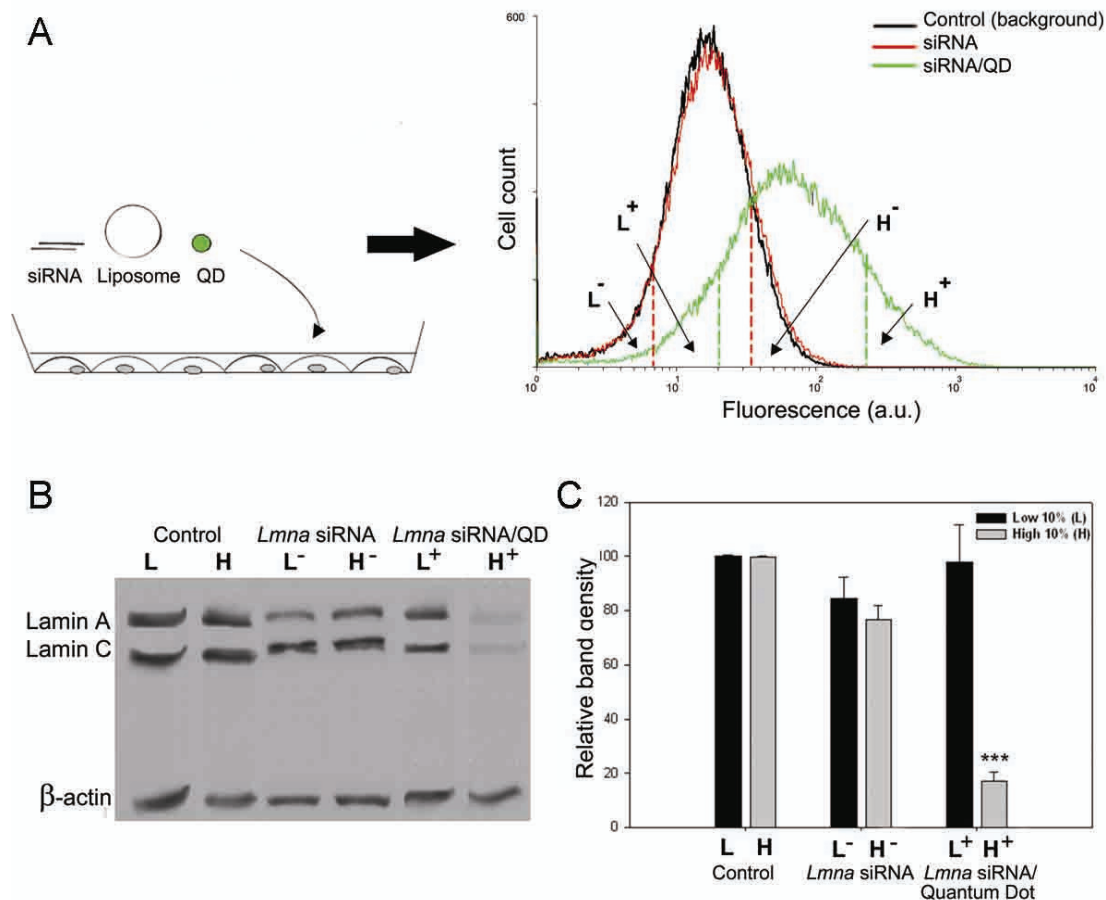


Figure 3.1 – QD/siRNA complexes allow sorting of gene silencing in cell populations. (A) Schematic representation of cells co-transfected with QDs and siRNA and analyzed for intracellular fluorescence by flow cytometry. Histograms depict fluorescence distributions of control murine fibroblast cells, *Lmna* siRNA-treated cells, and *Lmna* siRNA/QD-treated cells. FACS was used to gate and sort the high 10% (H) fluorescence and low 10% (L) fluorescence of each distribution. L^- and H^- point to gates for the siRNA only histogram. L^+ and H^+ indicate gates for the siRNA/QD histogram. (B) Representative Western blot of Lamin A/C protein expression levels in sorted cells with β -actin as loading control. Control lanes are protein from cells mock-transfected with liposome reagent only and sorted (L, H). The absence of QDs is indicated by a minus sign (-) and the presence of QDs is indicated by a plus sign (+). (C) Band densitometry analysis of Western blots from replicate experiments. Error bars represent standard error of the mean (n=3). ***P<0.001 (One-way ANOVA).

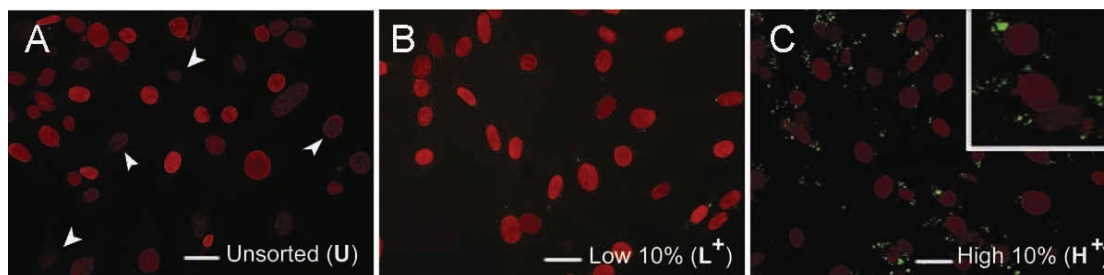


Figure 3.2 – Immunofluorescence staining of Lamin A/C nuclear protein (red).

(A) Unsorted cells (U) transfected with *Lmna* siRNA alone display heterogeneous staining for nuclear lamin throughout the cell population. White arrows highlight examples of cells with weak lamin staining among cells stained strongly for lamin. (B) Cells co-transfected with *Lmna* siRNA and green QDs exhibit bright lamin staining and lack of QDs in low-gated (L^+) cell subpopulations and (C) weak lamin staining and presence of QDs in high-gated (H^+) cell subpopulations (shown enlarged in inset). Scale bars 75 μm .

To optimize the QD/siRNA correlative effect, we varied the ratio of QD to lipofection reagent with a fixed dose of 100 nM siRNA. Specifically, we co-complexed *Lmna* siRNA with QD:lipofection reagent ratios of 1:5, 1:2, 1:1 or 2:1 (corresponding to 1, 2.5, 5 or 10 μg QD) and sorted the high 10% and low 10% of the cell fluorescence distributions as before. We found that optimal fluorescence and gene silencing correlation for the least amount of QD occurs at a 1:1 QD:lipofection reagent mass ratio (5 μg QD), as assayed by Western blot (**Figure 3.3A-C**). We hypothesize that this optimum results from the limited surface area of the cationic liposome delivery agent ($\sim 1 \mu\text{m}^2$) that is shared by the siRNA and QDs during the complexing process. Using too few QDs fails to provide fluorescence that is detectable over background, whereas excess QDs occupy sites on the liposome that would otherwise be available to siRNA. In support of this theory, we found that saturating the liposome with QDs (100:1 ratio) prior to transfection abolished correlation between cellular fluorescence and gene silencing; both high- and low-populations exhibited little to no knockdown (data not shown).

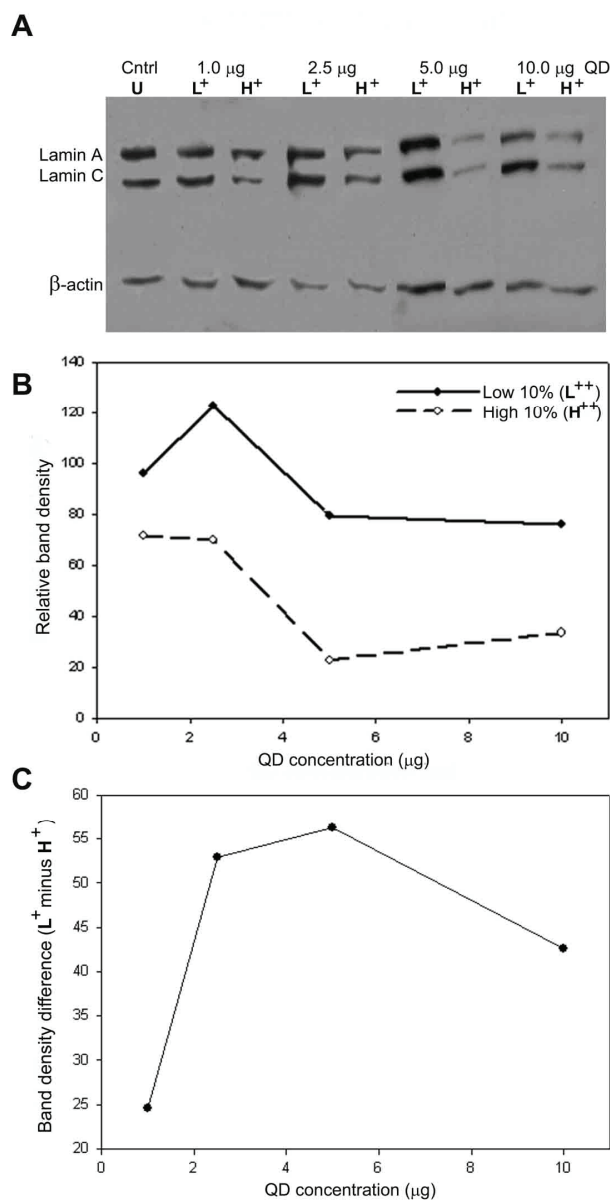


Figure 3.3 – Optimization of QD concentration for siRNA tracking. *Lmna* siRNA (100 nM) and 1, 2.5, 5, or 10 µg QD were co-transfected into murine fibroblasts and the cells FACS-sorted for the low 10% (L⁺) and high 10% (H⁺) of intracellular fluorescence distribution. (A) Protein expression of sorted cells assayed by Western blot, β-actin loading control. Unsorted, lipofectamine only control (U) represented 100% lamin a/c protein expression. (B) Western blot band densitometry analysis of L⁺ and H⁺ bands shows an optimum QD concentration for obtaining high-efficiency silencing. (C) Band density difference (L⁺ minus H⁺) reveals an optimum QD concentration for sorting most efficiently silenced from least efficiently silenced subpopulations.

QDs exhibit an extensive range of size- and composition- dependent optical properties, making them uniquely advantageous for multiplexing- i.e. monitoring and sorting cells that have been treated simultaneously with different siRNA/QD complexes. As a proof-of-principle, we complexed cationic liposomes with either green (em 560nm) QDs and *Lmna* siRNA or orange (em 600 nm) QDs and siRNA targeting T-cadherin (T-cad). Cells were exposed simultaneously to both complexes and flow cytometry was used to quantify orange fluorescence (600 +/- 10nm) versus green fluorescence (560 +/- 20nm) (**Figure 3.4A**). Cells exhibiting dual-color fluorescence were gated for low 8% and high 8% fluorescence and collected. Western blots probing lamin a/c and T-cad protein confirm specificity of QD/siRNA complexing (**Figure 3.4B and Figure 3.4C**), while fluorescence microscopy validates gating accuracy and demonstrates multi-color tracking capabilities (**Figure 3.5**). Unsorted cells transfected with T-cad siRNA alone expressed a 45% down-regulation in protein expression quantified by Western blot band densitometry. In contrast, co-delivery of QDs with T-cad siRNA and subsequent sorting enabled separation of the least efficiently transfected cell subpopulation (30% protein knockdown) from a highly transfected population (95% knockdown). In the highest 8% of the dual color, dual siRNA co-transfected cell population, highly effective silencing of both *Lmna* gene (96% knockdown) and T-cad gene (98% knockdown) was achieved. Given the wide spectrum of QD color possibilities, this method promises to be useful for tracking and sorting multiple siRNA-mediated knockdowns within one cell population.

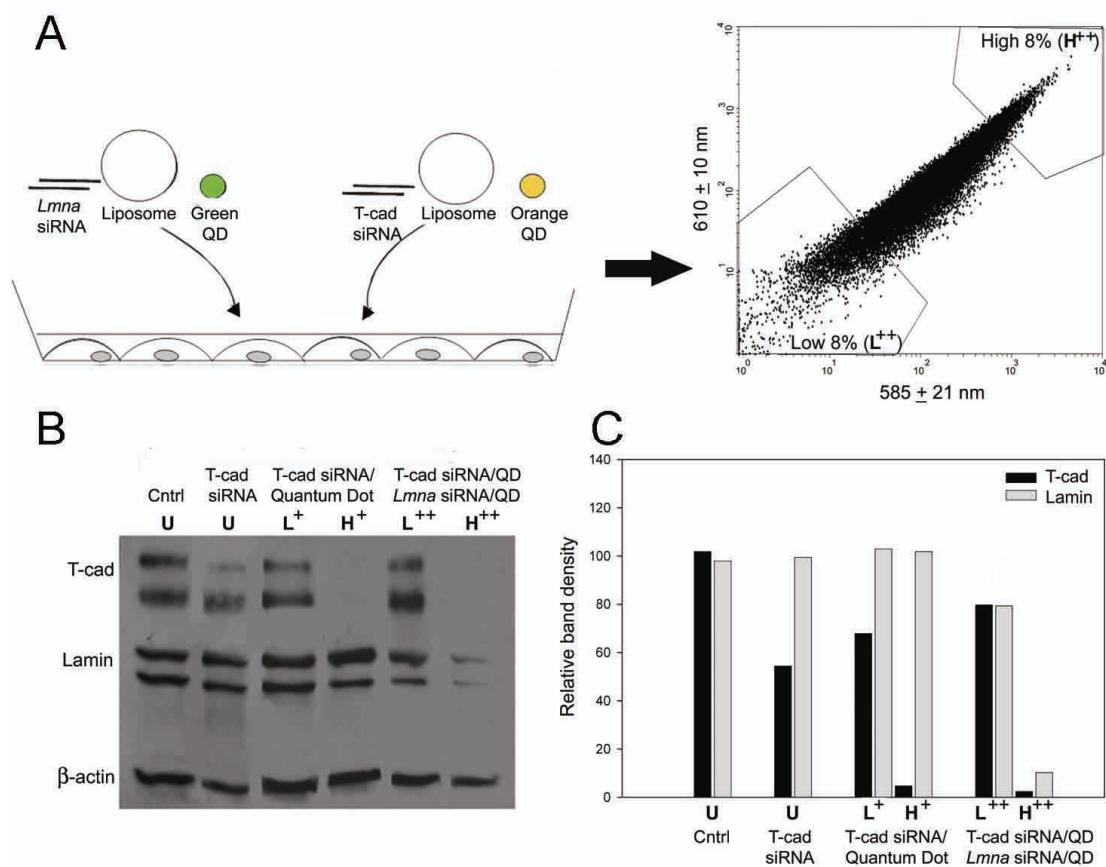


Figure 3.4 – Sorting the effects of double gene knockdowns using two colors of QDs. (A) Schematic representation of cells transfected simultaneously with *Lmna* siRNA/green QD complexes and T-cad siRNA/orange QD complexes. The low 8% (L^{++} , where ++ designates the presence of two colors of QDs) and high 8% (H^{++}) of the dual fluorescence dot plot was gated and isolated using FACS. (B) Representative Western blot and (c) corresponding band densitometry analysis of lamin A/C and T-cadherin protein levels in control unsorted (U) cells, unsorted (U) T-cad siRNA-treated cells, sorted T-cad/QD-treated cells (L^+ , H^+), and sorted dual siRNA/dual QD-treated (L^{++} , H^{++}) cells.

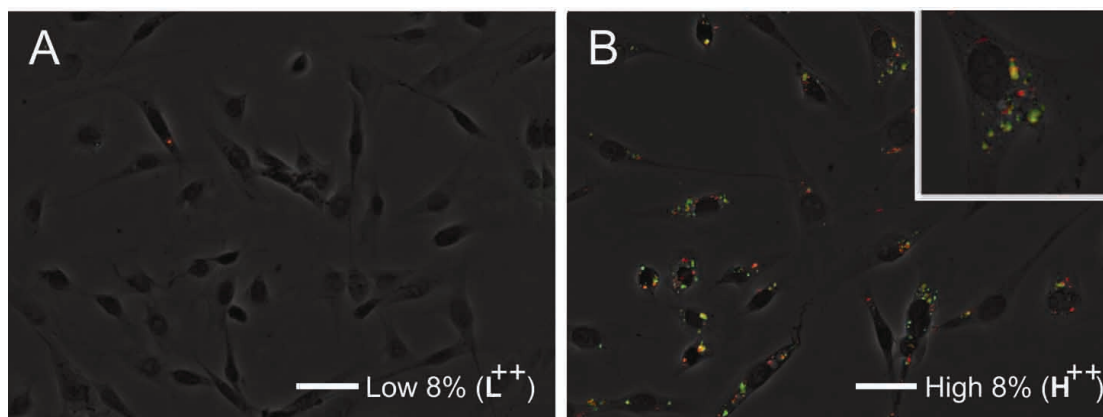


Figure 3.5 – Fluorescence/phase micrographs of two color QD transfections. (A) Low-gated cells (L^{++} , where ++ indicates the presence of two colors of QD) nearly lack orange or green QDs. (B) High-gated cells (H^{++}) fluoresce brightly with punctate green and orange QDs (enlarged in inset). Scale bars 100 μm .

The utility of RNAi as a functional genomics tool is predicated upon associating gene silencing with downstream phenotypic observations. Yet non-uniform gene silencing may obscure bulk measurements (protein, mRNA) commonly used to validate gene knockdown and obscure genotype/phenotype correlations. We compared the downstream effects of non-uniform and homogenous gene silencing to specifically examine the stabilizing effect of non-parenchymal cells (3T3 fibroblasts) on hepatocellular function *in vitro*¹²⁰. Recently, several cadherins from hepatocyte-fibroblast junctions were identified as potential mediators of liver-specific function *in vitro*¹²¹. Based on this finding, we transfected fibroblasts with T-cad siRNA or T-cad siRNA/QD complexes, sorted each population according to high or low cellular fluorescence, and co-cultivated the populations with hepatocytes. Markers of liver-specific function, albumin synthesis and cytochrome P450 1A1 (CYP1A1) activity, were measured in hepatocyte/3T3 co-cultures (**Figure 3.6**). Compared to control co-cultures, significant downregulation in hepatocellular function (2-fold) was observed exclusively in the cultures that had been treated with T-cad siRNA/QD complexes and sorted for high cellular fluorescence. These studies implicate a role for fibroblast T-

cadherin protein expression in modulating hepatocellular function in vitro, an interpretation revealed only once a homogenously-silenced population of fibroblasts was obtained.

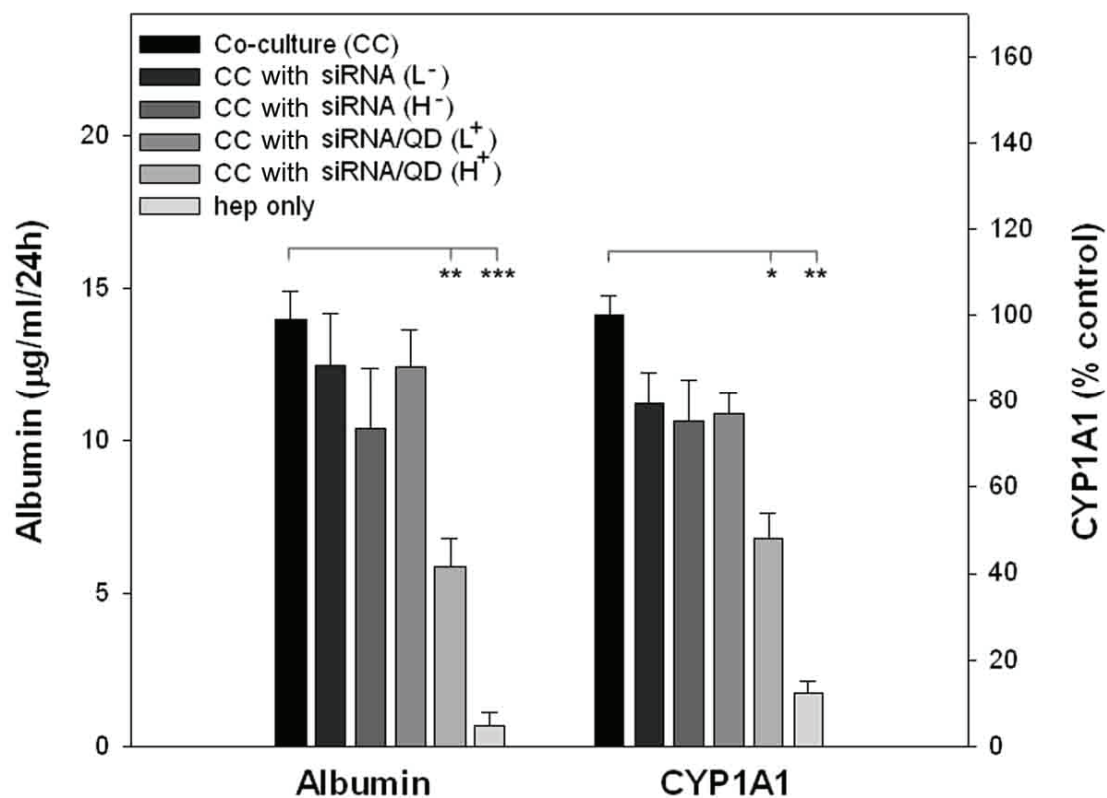


Figure 3.6 – Significant downstream gene knockdown effects of T-cadherin gene silencing are observed only in a homogenous silenced cell population. Murine 3T3 fibroblasts transfected with T-cad siRNA alone or with T-cad siRNA/QD complexes were FACS-sorted for low 10% (L) or high 10% (H) intracellular fluorescence. Symbols – and + indicate the absence or presence of QD during transfection. To study the stabilizing effect of non-parenchymal cell (3T3 fibroblast) protein expression on liver-specific function, control or transfected/sorted 3T3 cells were added to hepatocyte cultures 24 hours after hepatocyte seeding. Liver-specific function was assayed by measuring albumin synthesis and cytochrome P450 1A1 (CYP1A1) activity of cultured media sampled at 72 and 96 hours after 3T3 seeding and averaged. Error bars represent standard error of the mean (n=3). * P<0.05, **P<0.01, ***P<0.001 (One-way ANOVA statistical analysis test).

3.5 Conclusion

In this work, we have identified a role for T-cadherin in cell-cell communication between hepatocytes and non-parenchymal cells using a technically simple method for enriching transfected cells which can be applied to further studies. Incubating cells with concentrations of siRNA greater than 100 nM does not improve knockdown efficiency but may actually negatively regulate RNAi-mediated gene silencing (**Figure 3.7**)^{41, 124}. In addition, excesses of either siRNA or cationic liposome has been shown to induce increased cytotoxicity, interferon response¹²⁵ and ‘off-target’ effects¹²⁶. While current techniques are available to fluorescently track RNAi delivery (co-delivery of fluorescent protein expressing plasmids, end-labeling with a dye), none offer such a simple, modular, and versatile means to generate a homogeneously silenced population. In addition to superiority over dyes in brightness and photostability (**Figure 3.8**), multicolor QD labels can be used interchangeably, with all particle sizes employing a common, passive mechanism to form delivery complexes. The point at which a cell’s RNAi machinery saturates is not yet known; yet at the least this capability simplifies known strategies to enrich for dual gene knockdowns using antibiotic-resistant markers that are co-transfected, transcribed, and selected. The numerous non-overlapping color possibilities of QDs (12 commercially available in the spectral range of FACS detectors) may further enable multiplexed and combinatorial gene studies for the potential illumination of entire biological pathways. Use of commercial QDs in the amounts specified would be reasonably economical—approximately the same cost as the liposome reagent and approximately 4 times lower than the synthesis of dye-labeled RNA. As shown in previous work, QDs are compatible with a variety of transfection techniques (other reagents, electroporation, microinjection) and therefore amenable to nucleic acid monitoring in cells lines and

primary cells that are susceptible to liposome-triggered cytotoxicity¹²⁷. Thus, quantum dots are versatile, photostable probes that offer an added dimension to improve the power of RNAi as an experimental tool.

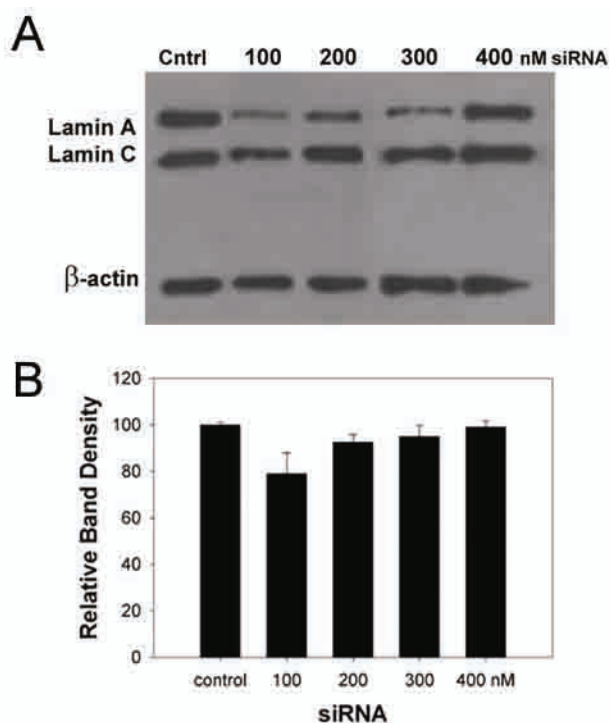


Figure 3.7 – Knockdown efficacy is not improved by transfecting higher doses of siRNA. 3T3 murine fibroblasts were transfected with 100, 200, 300 or 400 nM *Lmna* siRNA and harvested for protein after 72h. (A) Representative Western blot of Lamin A/C protein levels, β-actin loading control. (B) Band densitometry analysis from replicate experiments, where error bars represent standard error of the mean (n=2).

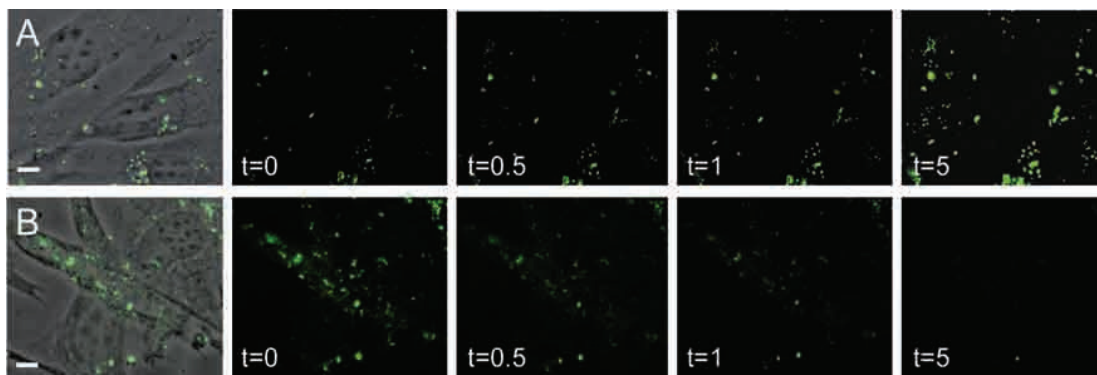


Figure 3.8 – Comparison of QD and fluorescein-labeled siRNA fluorescence in 3T3 murine fibroblasts. Cells were transfected with 20 μg QD (emission 566 nm) or 100 nM Lamin A/C siRNA modified with fluorescein on the 5' end of the sense strand. (A) QDs fluoresce brightly under continuous mercury lamp exposure over several minutes, while the fluorescein attached to the siRNA bleaches under continuous excitation and is no longer detectable after $t=5$ minutes (B). Scale bars are 25 μm .

3.6 Acknowledgements

We thank Mike Sailor for providing facilities for QD synthesis, Dennis Young for his assistance with flow cytometry, Barbara Ranscht for providing antibody, Jennifer Felix and Kathryn Hudson for hepatocyte isolation, Howard Green for supplying 3T3-J2 fibroblasts and Lee Gehrke for comments on the manuscript. Funding was generously provided by the National Science Foundation (AAC), a G.R.E.A.T. fellowship from UC-BREP (2004-16) (AMD), the David and Lucille Packard Foundation, NIH NIDDK, NCI, NIH (contract no. N01-CO37117) and NASA.

This chapter was reproduced in full from Chen AA, Derfus AM, Khetani SR and Bhatia SN. "Quantum Dots to Monitor RNAi delivery and Improve Gene Silencing." *Nucleic Acids Research* **33** (2005):e120. The dissertation author was the co-primary investigator and co-first author on the paper. He thanks Alice Chen, Salman Khetani, and Sangeeta Bhatia for their significant contributions to the work.

CHAPTER 4

TARGETED QUANTUM DOT CONJUGATES FOR SIRNA DELIVERY

4.1 Abstract

Co-delivery of siRNA and quantum dots using a cationic liposome reagent has allowed the monitoring of gene silencing *in vitro*. These complexes, however, are not suitable for systemic targeting due to their large size and net positive charge. Instead, we have replaced the functions of the cationic liposome with other components. Heterobifunctional crosslinkers were used to link siRNA duplexes to the surface of polymer-coated quantum dots. Along with the siRNA, homing peptides specific to tumor vasculature were attached. The cellular uptake and silencing efficiency of these conjugates was characterized.

4.2 Introduction

RNA interference (RNAi)-based therapeutics can be applied to a variety of diseases where protein over-expression is at fault. Design of a double-stranded RNA sequence against the mRNA of the targeted protein and delivery of this duplex into the cytoplasm of affected cells leads to a reduction in protein expression, or knockdown. Use of this technology *in vivo*, however, is hampered by problems with stability and systemic delivery. Due to the small size of individual siRNA duplexes, renal filtration is rapid and blood circulation half-life of unmodified nucleic acid is ~6min.¹⁰⁹

Conglomeration of siRNA duplexes into nano-sized complexes has shown to greatly improve their circulation time and therapeutic effect. Cholesterol-siRNA conjugates bind serum albumin after i.v. injection, forming long-circulating “natural” nanoparticles.¹⁰⁹ Additionally, carriers can be formed ex vivo by condensing the nucleic acid with a cationic protein (e.g. protamine¹²⁸) or polymer (e.g. poly(ethylene imine) (PEI)¹⁰⁷, cyclodextrin-containing polycations¹²⁹) prior to injection. In addition to improved circulation, these complexes can be targeted to a disease site through the attachment of peptide¹⁰⁷, small molecule (transferrin¹²⁹) or antibody¹²⁸ ligands. While the sequence specificity of siRNA does much to reduce collateral effects, targeted delivery to the site of focal disease can allow a reduction in the administered dose and may alleviate off-target knockdown¹²⁶.

Imaging agents delivered along with siRNA in these complexes can illustrate their biodistribution, allowing quantification of therapeutic reaching the target and improving the safety and efficacy of delivery. Yet, often 48 hours or more after administration of siRNA is required to observe gene knockdown, and fluorescent dyes are not stable for extended periods of time in vivo. Co-delivery of a fluorescent reporter plasmid along with the siRNA is not a reasonable strategy for clinical use. Instead, we propose attaching semiconductor quantum dots (QDs) to the siRNA as a photostable beacon. Monitoring the delivery of siRNA with QDs has been achieved by complexing both species with cationic liposomes (e.g. Lipofectamine 2000) for in vitro delivery.¹²¹ While this approach leads to internalization and endosome escape of both particles and nucleic acid, this strategy is not amenable to in vivo use and does not allow targeting to a subpopulation of diseased cells. In adapting this co-delivery

technique, key features that should be retained are QD/siRNA attachment, cell internalization of the complex, and exit from the endolysosomal pathway.

Our strategy for co-delivery of QDs and siRNA is presented in **Figure 4.1**. We have taken a multidentate approach, using the QD core as a scaffold and adding siRNA and homing peptides specific for tumor cells to functional groups on its surface. The QD core can be tuned for emission in the near-infrared (NIR), allowing greater imaging depth in tissue than visible wavelengths. The siRNA will be attached to the surface with a chemical crosslinker, rather than the electrostatic interactions used in many schemes. For this proof-of-concept work, the attached siRNA was designed against the EGFP gene, and complexes were delivered to EGFP-transfected HeLa cells in vitro. Attaching of a tumor homing peptide (F3), targeting cell-surface nucleolin¹³⁰, was attached to achieve cell uptake.

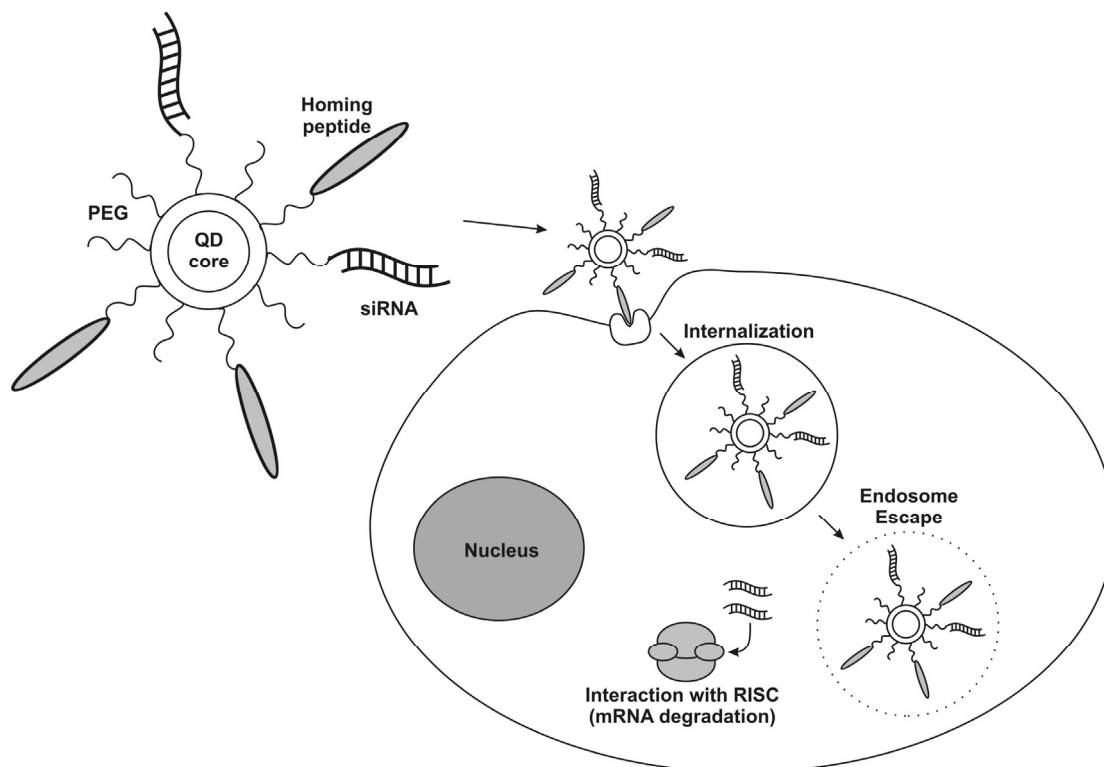


Figure 4.1 – Scheme for delivery of QD/siRNA conjugates. PEGylated QDs do not significantly internalize in most cell types. Attachment of a homing peptide allows receptor-mediated endocytosis. After internalization, the conjugate must escape the endosomal vesicle in order to interact with RISC and trigger mRNA degradation.

While the formulation of these particles may seem to be a simple task of co-conjugation, multiple questions exist that will affect their design and fabrication. First, we have investigated whether the attachment of these short peptides is necessary and sufficient to achieve cell internalization. Further, as particle surface area is limited (~100 surface amines on these QDs), the required copy number is also called into question. Increasing the number of peptides on the QDs accrues the opportunity cost of a lower siRNA dose per particle. There is also potential for interactions between the positively charged internalization peptides and the anionic siRNA cargo,

reducing the effectiveness of a peptide whose uptake mechanism is charge-dependent. Each of these factors must be considered in optimizing co-conjugation of these species for maximum knockdown.

Second, conjugation of siRNA to the particles must be stable in cell media (and potentially in serum), but must allow the duplex to interact with RISC. While RISC binding may be possible while the duplex is attached to the particle, release of the siRNA from the particle's surface upon internalization is likely desirable. We have investigated two crosslinkers for this task, and tested their efficiency independent of particle uptake by using a cationic liposome transfection reagent for delivery.

Finally, escape from the endolysosomal pathway is essential to prevent degradation of siRNA allow interaction with the cytoplasmic silencing machinery. While fluorophore-labeled peptides have been shown to reach the nuclei of cells in vitro and in vivo, are these peptides sufficient to allow endosome escape of QD conjugates? If not, does the addition of endosome-disrupting peptides or chemotherapeutics aid escape and increase knockdown? We have examined both of these questions in an effort to achieve cytoplasmic siRNA delivery.

4.3 Materials and Methods

4.3.1 Cell Culture

Internalization and knockdown experiments were performed using a HeLa cell line stably transfected with 1h destabilized EGFP (courtesy of Phillip Sharp, MIT). Growth media was Dulbecco's modified Eagle's medium (DMEM) containing 4.5 g/L

glucose and supplemented with 10% FBS, 100 units/mL penicillin, 100ug/mL streptomycin, and 292 ug/mL L-glutamine. Cells were passaged into 24-well plates and used at ~50% confluency.

4.3.2 Materials

Quantum dots with an emission maxima of 655, 705 and 800 nm and modified with PEG and amino groups were obtained from Quantum Dot Corporation (ITK amino). QD concentrations were measured by optical absorbance at 595nm, using extinction coefficients provided by the supplier. Crosslinkers used were sulfo-LC-SPDP (Sulfosuccinimidyl 6-(3'-[2-pyridyldithio]-propionamido)hexanoate)(Pierce) and sulfo-SMCC (Sulfosuccinimidyl-4-(*N*-maleimidomethyl)cyclohexane-1-carboxylate)(Sigma). Synthetic RNA duplexes directed against the EGFP mRNA were synthesized, with the sense strand modified to contain a 5' thiol group (Dharmacon) (Sense: 5'-Th-(CH₂)₆-GGC UAC GUC CAG GAG CGC ACC; Antisense: 5'-UGC GCU CCU GGA CGU AGC CUU). The F3 peptide was synthesized as previously described, with an animohexanoic acid (Ahx) spacer and cysteine residue added for conjugation (final sequence: C[Ahx]AKVK DEPQR RSARL SAKPA PPKPE PKPKK APAKK). Peptides were synthesized in house (F3, KAREC) and by Global Peptide (INF7).

4.3.3 QD/siRNA/F3 conjugation

Amino-modified QDs were conjugated to thiol-containing siRNA and peptides using Sulfo-LC-SPDP and Sulfo-SMCC crosslinkers. For sulfo-LC-SPDP, QDs were resuspended in 0.1M Sodium Phosphate, 0.15M Sodium Chloride, pH 7.2, using

Amicon Ultra-4 (100kDa cutoff) filters. For sulfo-SMCC, a slightly different buffer was used: 50mM Sodium Phosphate, 0.15M sodium chloride, pH 7.2. Crosslinker (1000-fold excess) was added to QDs and allowed to react for one hour. Samples were filtered on a NAP-5 gravity column (to remove excess crosslinker) into similar buffer supplemented with 10mM EDTA. SiRNA was treated with 0.1M DTT for one hour and filtered on a NAP-5 column into EDTA-containing buffer. Peptides were typically used from lyophilized powder. Peptide and/or siRNA was added to filtered QDs and allowed to react overnight at 4degC. Using three Amicon filters, product was filtered twice with PBS, twice with SSC (1.0 M sodium chloride, 100 mM sodium citrate, pH 7.2), and twice again with PBS. SSC washes were required to remove electrostatically bound siRNA and peptide, which was not removed with PBS washes alone.

4.3.4 QD internalization

QDs were added to cell monolayers in complete media at a final concentration of 50nM. After four hours, cells were washed with media, treated with trypsin (0.25%) and EDTA, and resuspended in 1% BSA (in PBS) for flow cytometry (BD FACSort, FL1 for EGFP signal and FL3 for QD signal).

4.3.5 Cationic liposome-mediated delivery

Experiments were performed using 1uL of Lipofectamine 2000 (Invitrogen) per well added to 50uL of serum/antibiotic-free media. QDs (also in 50uL media) were added and allowed to complex for 20 minutes. Cell media was changed to 400uL of serum/antibiotic-free, and QD solutions were added dropwise. Complete

media was added 12 -18 hours later. 48 hours after QD were added, cells were trypsinized and assayed for fluorescence by flow cytometry. Concentrations noted in figure and text refer to total media volume (500uL).

4.4 Results and Discussion

As described in **Figure 4.1**, a particle capable of three distinct functions is required for QD and siRNA delivery. Taking a modular approach, the required functions of internalization, siRNA attachment, and endosome escape were investigated separated, and then combined in a single particle.

First, peptides were conjugated to QDs to improve tumor cell uptake. Addition of as-purchased PEGlyated QDs to HeLa cell monolayers led to minimal cell uptake when quantified with flow cytometry (**Figure 4.2A**). Addition of F3 peptide to the QDs improved the uptake significantly (two orders of magnitude). The endosome escape peptide INF7, a variant of the influenza HA2 domain¹³¹, did not improve cell uptake, but did not prevent F3-mediated uptake when the two peptides were co-attached (1:1 reaction ratio). Conjugation of a control pentapeptide (KAREC) did not affect QD uptake as well. To confirm the specificity of F3 uptake, free F3 peptide was added to cells along with 50nM F3-QDs. Dose-dependent inhibition of uptake was observed with F3 peptide concentrations from 1uM to 1mM. Inhibition of uptake by free KAREC peptide was minimal by comparison. The large excess of free peptide required for inhibition may be due to multiple copies of the F3 peptide on each QD.

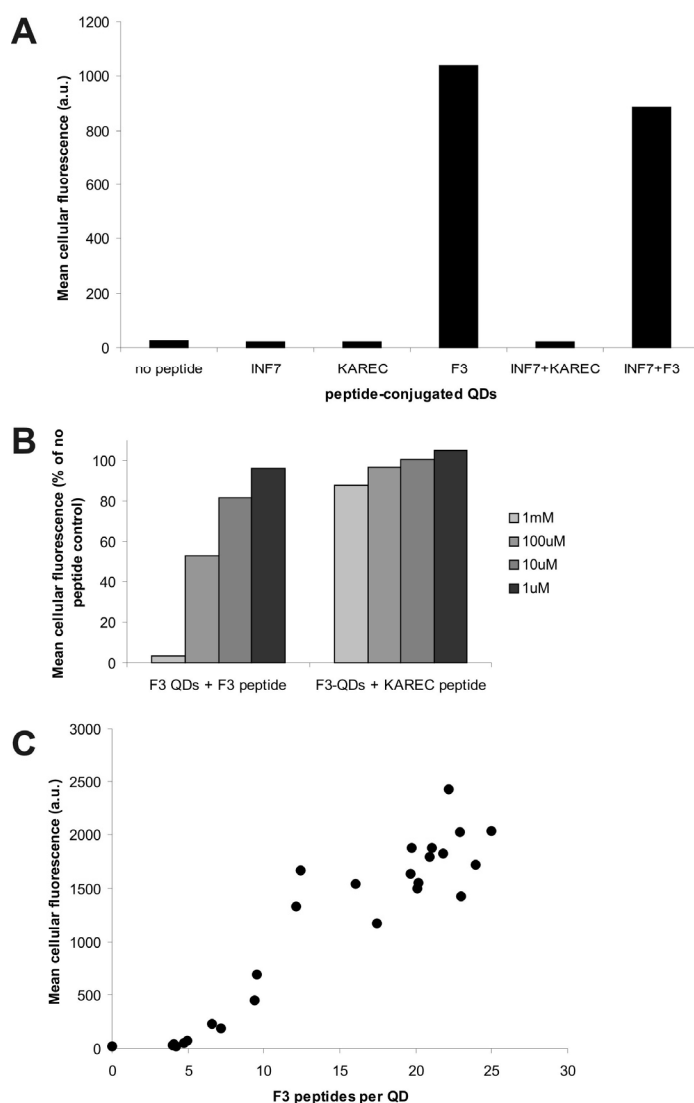


Figure 4.2 – Attachment of F3 peptide leads to QD internalization in HeLa cells. Various peptides were conjugated to QD705 particles, filtered to remove excess peptide, and incubated with cell monolayers for 4 hours. Flow cytometry of trypsinized cells indicates that the F3 peptide is required for cell entry (A). The addition of free F3 peptide inhibits F3-QD uptake, while KAREC peptide does not (B). Multivalency of F3 is required for uptake, as low numbers of peptide per QD (<10-15) does not lead to significant internalization. F3 peptide per QD was quantified by attaching FITC-labeled peptide with SPDP, treating the conjugate with beta-mercaptoethanol, filtering the QDs, and measuring the FITC fluorescence.

To quantify this ratio, FITC-labeled F3 peptide was synthesized and attached to QDs using a cleavable crosslinker (sulfo-LC-SPDP). After filtering to remove unreacted peptide, beta-mercaptoethanol (BME) was added to reduce the disulfide bond between peptide and QD. Using a 100kD cutoff filter, F3-FITC peptide was separated from the QDs and quantified by fluorescence. Several reactions were performed with various amounts of FITC-F3 and siRNA as reactants. For each formulation, the cellular uptake was quantified by flow cytometry and F3 number measured (**Figure 4.2C**, each point indicates a separate formulation). The results suggest a maximum of 20-25 F3 peptides can be added per QD. Attachment of a small number of peptides (0-5) did not lead to significant uptake (less than 10% of maximum). Uptake increases with peptide number, but begins to saturate around 20 copies per QD.

The use of cleavable (sulfo-LC-SPDP) or non-cleavable (sulfo-SMCC) crosslinkers for the attachment of F3 peptide did not significantly affect cell uptake. The choice of crosslinker, however, may affect the ability of attached siRNA to interact with RISC. The interior of the cell is a reducing environment, which would lead to cleavage of an SPDP generated crosslink and separation of QD and siRNA. On the other hand, the bond produced by SMCC is unaffected by reducing conditions (confirmed by treating the conjugates with 2.5% BME for 30 min). We compared the efficiency of QD/siRNA conjugates prepared with both crosslinkers. As a proof-of-concept, siRNA targeting the EGFP mRNA were used. Delivery of the conjugates to EGFP-labeled HeLa cells was performed by first complexing the particles with

Lipofectamine 2000, to satisfy the functions of cell internalization and endosome escape.

Using gel electrophoresis, the amount of siRNA conjugated per particle was quantified. Particles were first introduced under native (non-reduced) conditions (**Figure 4.3B**). The absence of a siRNA band in the SPDP and SMCC lanes indicates that no siRNA is loosely (electrostatically) bound to the particles. Washing the particles with a high salt solution was necessary to remove siRNA attached in this manner. While a 10-fold molar excess of siRNA was used for both formulations, the amount of siRNA attached to each QD was greater in the SMCC case. Running the gel after exposing the particles to BME for 30min leads to the appearance of a siRNA band in the SPDP lane, which can be quantified with standards and ImageQuant software (**Figure 4.3C**). Approximately two siRNA duplexes were conjugated per QD under these conditions. Both formulations were complexed with Lipofectamine 2000 and added to EGFP-labeled HeLa cells. Cellular fluorescence was quantified 48 hours later using flow cytometry. As hypothesized, the QD/siRNA formulation produced with the SPDP crosslinker leads to greater EGFP knockdown in a range of concentrations (**Figure 4.3D**).

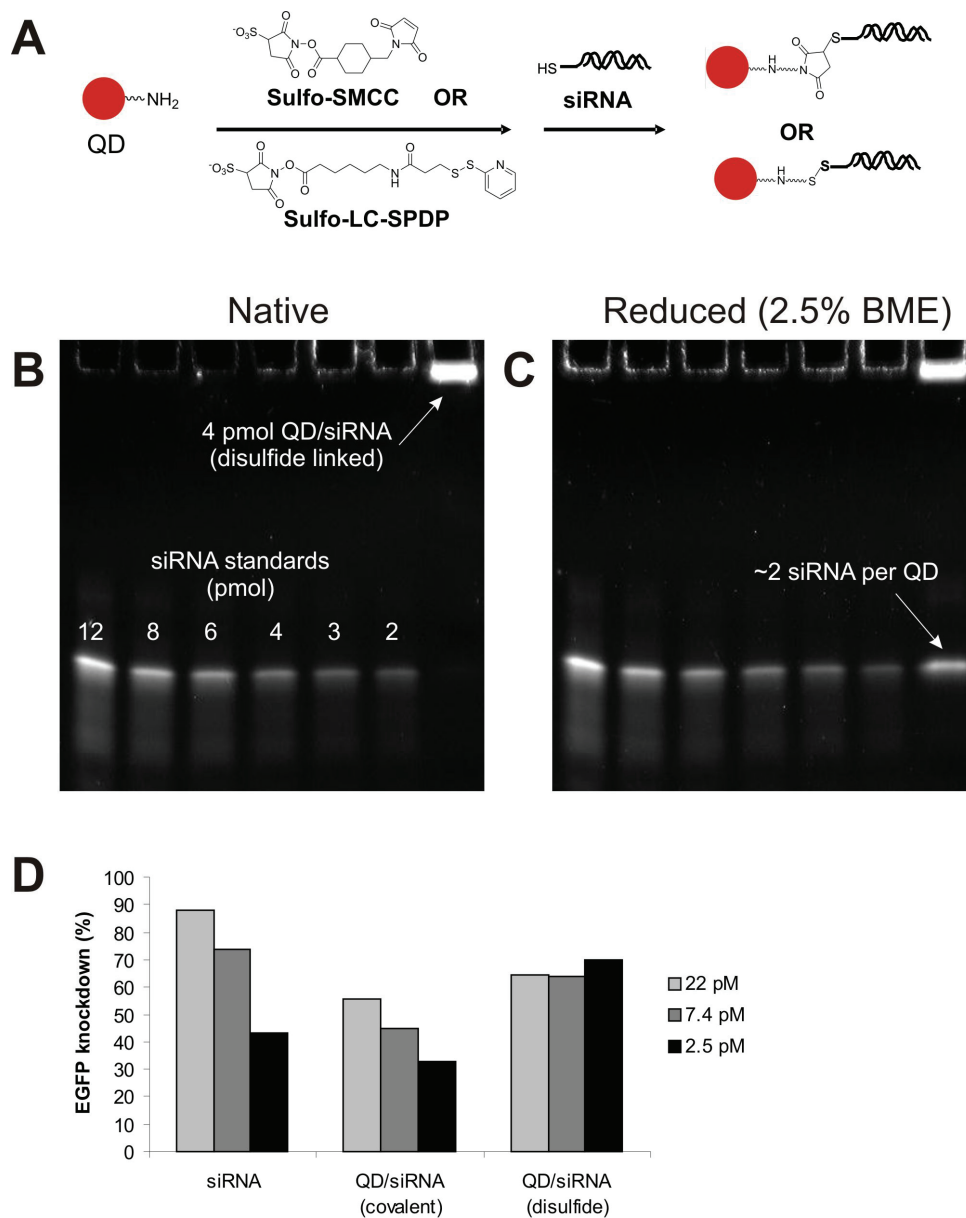


Figure 4.3 – Conjugation of siRNA to QDs with cleavable or non-cleavable crosslinkers. Thiol-modified siRNA was attached to amino-modified QDs using the water-soluble heterobifunctional crosslinkers sulfo-SMCC and sulfo-LC-SPDP (A). The crosslink produced by SPDP is cleavable with beta-mercaptoethanol, while the bond attained with SMCC is covalent. Gel electrophoresis of the disulfide-linked conjugates indicates that no siRNA are electrostatically bound to the conjugate (B). Upon treatment with beta-mercaptoethanol (BME), the QD/siRNA crosslink is reduced and the siRNA migrates down the gel even with siRNA standards. Delivery of the QD/siRNA conjugates with Lipofectamine 2000 (cationic liposome reagent), indicates the disulfide bond leads to superior EGFP knockdown (D).

In the absence of cationic liposome reagent, no reduction in EGFP signal is observed for either formulation. Attachment of F3 peptide along with siRNA is the first step towards Lipofectamine-independent knockdown. The ratio of siRNA and F3 peptide was varied with the goal of generating a formulation with high cell uptake, but also carrying a significant payload of siRNA. The results indicate a trade-off between one siRNA per particle with high uptake (>1000 a.u.), and two duplexes but low uptake (**Figure 4.4A**). It is possible that the negatively-charged siRNA are “laying down” on the surface of the aminated particles, preventing the attachment of additional F3 peptides. While fluorescence is non-linear, particles with high uptake and a single siRNA duplex were judged superior.

When this formulation was added to cells, however, no reduction in EGFP expression was observed 48 hours later. Staining with an endolysosomal marker (LysoSensor) and observation under fluorescence microscopy suggests the particles may be endosomal (**Figure 4.4B**). Though the issues of particle internalization and siRNA attachment have been solved, the feat of endosome escape remains. We plan to pursue the addition of chemotherapeutic (chloroquine) and/or endosome escape peptide (INF7).

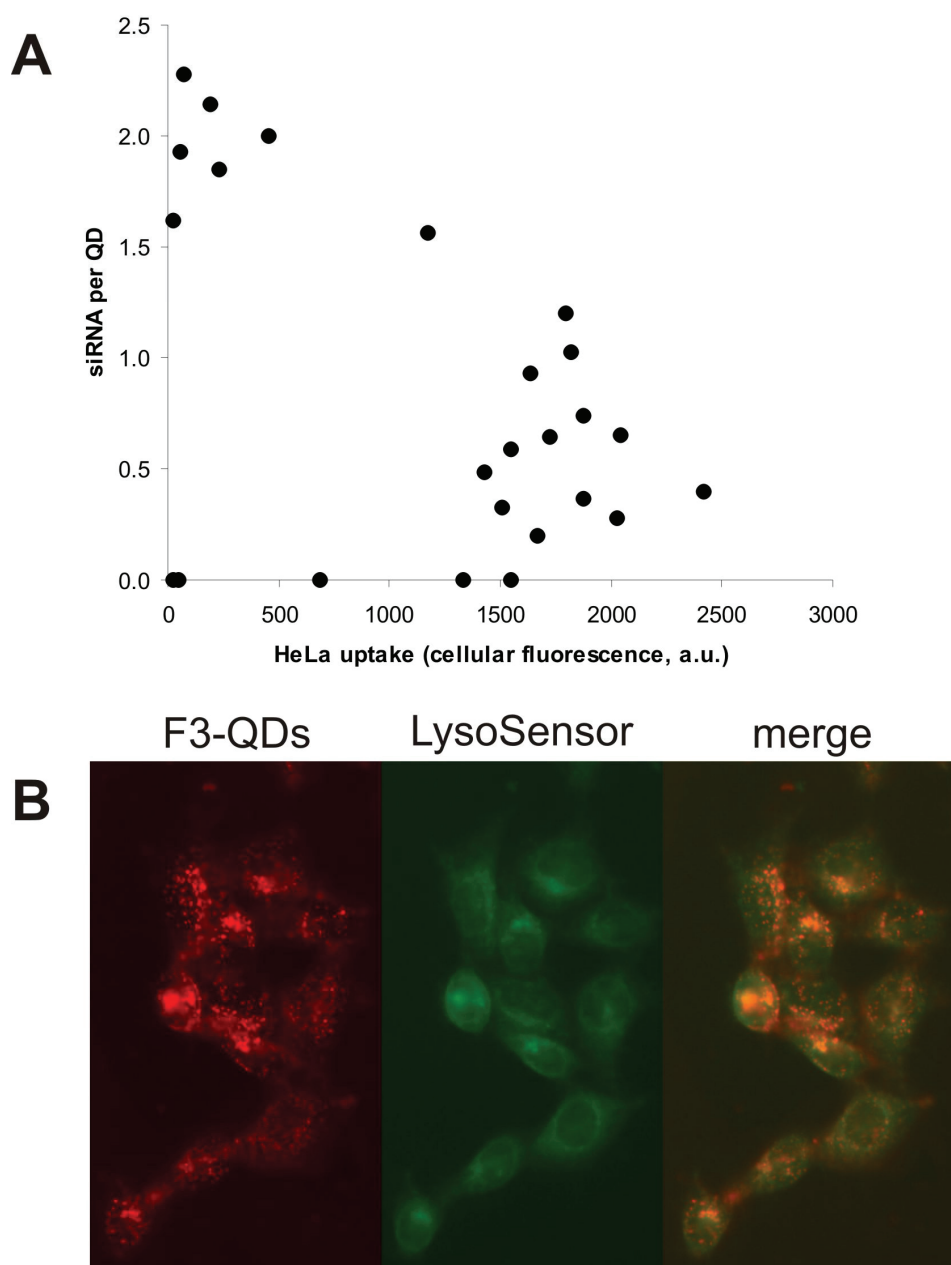


Figure 4.4 – EGFP knockdown is limited by number of siRNA per QD and endosome entrapment. While QD/F3/siRNA conjugates can be delivered to cells in significant numbers, these particles contain only 1-2 siRNA duplexes per particle (A). The conjugation of the large (13kD) negatively charged nucleic acid may prevent addition F3 peptides from attaching. Conjugates containing ~ 1 siRNA and ~ 20 F3 peptides are internalized into HeLa cells, but co-localize with an endosome label (LysoSensor) four hours after uptake (B). Both of these factors contribute to the lack of EGFP knockdown observed with these conjugates.

4.5 Conclusion

Three critical questions were addressed concerning the delivery of QD/siRNA/peptide conjugates. We found the F3 peptide was necessary and sufficient for QD uptake, and siRNA cargo co-attached without affecting the function of the peptide. Disulfide (sulfo-LC-SPDP) and covalent (sulfo-SMCC) crosslinkers were investigated for the attachment of siRNA to the particle, with the disulfide bond showing greater efficacy in lipofectamine-assisted silencing. Finally, we investigated the knockdown of these engineered particles, observing no significant gene silencing due to low siRNA loading and endosomal entrapment. We plan to investigate the addition of endosome escape functionality to the particle, which may improve overall efficacy.

4.6 Acknowledgements

We thank Fernando Ferrer for peptide synthesis, Phillip Sharp for HeLa cell line and siRNA sequence, and acknowledge financial support of the David and Lucile Packard Foundation, the National Cancer Institute of the National Institutes of Health (Contract No. N01-C0-37117). AMD thanks the UC Biotechnology Research and Education Program for a G.R.E.A.T. fellowship (#2004-16).

This chapter was reproduced in part from Derfus AM, Chen AA, Ruoslahti E, Bhatia SN. “Targeted Quantum Dot conjugates for siRNA delivery.” (submitted to *Bioconjugate Chemistry*). The dissertation author was the primary investigator and first author on the paper. He thanks Alice Chen, Erkki Ruoslahti, and Sangeeta Bhatia for their significant contributions to the work.

CHAPTER 5

PROBING THE CYTOTOXICITY OF SEMICONDUCTOR QUANTUM DOTS

5.1 Abstract

With their bright, photostable fluorescence, semiconductor quantum dots show promise as alternatives to organic dyes for biological labeling. Questions about their potential cytotoxicity, however, remain unanswered. While cytotoxicity of bulk cadmium selenide (CdSe) is well documented, a number of groups have suggested that CdSe QDs are cytocompatible, at least with some immortalized cell lines. Using primary hepatocytes as a liver model, we found that CdSe-core QDs were indeed acutely toxic under certain conditions. Specifically, we found that the cytotoxicity of QDs was modulated by processing parameters during synthesis, exposure to ultraviolet light, and surface coatings. Our data further suggests that cytotoxicity correlates with the liberation of free Cd²⁺ ions due to deterioration of the CdSe lattice. When appropriately coated, CdSe-core QDs can be rendered non-toxic and used to track cell migration and reorganization *in vitro*. Our results inform design criteria for the use of QDs *in vitro* and especially *in vivo* where deterioration over time may occur.

5.2 Introduction

Recently, nanomaterials have received enormous attention for their potential applications in biology and medicine. A key issue in evaluating the utility of these

materials is assessing their potential toxicity – either due to their inherent chemical composition (e.g. heavy metals) or as a consequence of their nanoscale properties (e.g. inhalation of particulate carbon nanotubes^{132, 133}). CdSe-core quantum dots are an example of a nanomaterial that has been shown useful as an alternative to fluorescent dyes for use in biological imaging, due to their bright fluorescence, narrow emission, broad UV excitation and high photostability^{1, 78, 134}. In addition to labeling of cellular structures *in vitro*^{47, 49, 51, 78, 79, 135}, several groups have demonstrated the use of QDs for fluorescence imaging *in vivo*^{1, 42, 55}.

As the popularity of QD labeling soars, however, concerns are beginning to surface about the toxicity of these cadmium-containing nanoparticles. Several commentaries have recently posed the question of QD toxicity, but no solid evidence exists to provide a definitive answer¹³⁶⁻¹³⁸. There has been considerable concern that the inherently toxic elements of the QD core (e.g., cadmium, selenium) would render the nanoparticles toxic to both cell cultures and live animals. While previous *in vitro* labeling experiments have not shown significant toxicity, most have used short-term QD labeling and immortalized cell lines that are not highly sensitive to heavy metals^{49, 51, 79}. Additionally, a relevant model for *in vivo* toxicity should be examined, as design criteria and constraints for preventing cytotoxicity *in vivo* are needed.

In vivo, the liver is the primary site of acute injury due to Cd exposure, and even low levels of cadmium ions (100-400 μ M) are known to reduce the viability of hepatocytes *in vitro*¹³⁹. Furthermore, greater than 25% of the cadmium administered to rats accumulates in the liver¹⁴⁰. Cadmium binding to sulfhydryl groups of critical mitochondrial proteins is thought to be the mechanism of hepatic injury¹⁴¹. Thiol group inactivation then leads to oxidative stress and mitochondrial dysfunction. Metallothionein, a protein found in the cytoplasm of hepatocytes, detoxifies cadmium by sequestering it into an inert complex. Yet, the small amounts of this protein

normally present in animals is not sufficient when cells are exposed to high levels of Cd^{2+} ions. Hepatocytes isolated from rats and grown *in vitro* have metallothionein levels similar to those in the intact liver, and thus isolated cells serve as representative model for *in vivo* hepatotoxicity¹⁴². Since the liver is a major target of Cd injury, primary hepatocyte culture is an ideal model to investigate the cytotoxicity of QDs.

A variety of syntheses, storage, coating strategies have been proposed for CdSe QDs^{8, 17, 44, 63, 80}. While long-term animal studies remains the gold standard for toxicology, examination of extreme conditions in appropriate *in vitro* models is a well-established approach to evaluate the toxicity of novel materials and is therefore the strategy pursued in this study. Our initial observations led us to conclude that process parameters and environmental conditions could dramatically affect the observed toxicity in a hepatocyte culture model. Furthermore, the cytotoxicity was affected by the degree and stability of the QD surface coating. We therefore set out to systematically examine the role of process parameters, surface coatings, and UV excitation on the rate of cytotoxicity as well as establish mechanistic framework to unify our findings and establish a benchmark for determining the biocompatibility of novel surface coatings.

5.3 Materials and Methods

5.3.1 Quantum Dot Synthesis

CdSe nanocrystals were synthesized¹⁷ and water-solubilized with mercaptoacetic acid (MAA)⁷⁸ as previously described. Briefly, CdSe nanocrystals were synthesized by rapid injection of a precursor $\text{Cd}(\text{CH}_3)_2/\text{Se}$ solution into high temperature TOPO solvent. The size of the particles was controlled by manipulating the TOPO impurities and the Oswald ripening process. The temperature was lowered to 70°C, methanol

was added to precipitate the QDs, and then centrifuged. Excess TOPO was soluble in the methanol and was removed during the decantation process. These QDs were readily redissolved in chloroform. Finally, excess MAA was added to chloroform-soluble QDs to yield water-soluble particles for cellular studies.

5.3.2 Quantum Dot Surface Coating

ZnS. To increase the quantum yield and protect the CdSe surface, a capping layer of 1-2 monolayers of ZnS was deposited by the slow addition of a $\text{Zn}(\text{CH}_3\text{CH}_2)_2/\text{S}$ solution at a temperature lower than for the synthesis of CdSe (270°C vs 360°C)^{44, 63, 80}. After the final of addition of the $\text{Zn}(\text{CH}_3\text{CH}_2)_2/\text{S}$ solution, the temperature was lowered, methanol was added, and the QDs redissolved in chloroform. The ZnS/CdSe QDs were water-solubilized with MAA.

Bovine Serum Albumin (BSA) coating. 1 mg/mL MAA-QDs were added to a 5% BSA solution in PBS. 50mM of 1-Ethyl-3-[3-dimethylaminopropyl]carbodiimide-hydrochloride (EDAC)(Sigma) was added to cross-link the BSA with the QDs, via the formation of a peptide bond. Since this reaction is non-specific, BSA proteins are also cross-linked to each other on the surface of the QD. This forms a highly stable protein-shell on the surface of the particle. These QDs are single, as observed by their intermittent on/off behavior on an epifluorescence microscope under Hg-lamp excitation. After conjugation, ultracentrifugation (45k RPM) was used to remove excess BSA from solution. Pelleted QDs were redissolved in small amounts of PBS.

Epidermal Growth Factor (EGF) coating. The procedure described in Akerman and coworkers was utilized to coat ZnS-capped CdSe with polyethylene glycol and EGF¹.

5.3.3 QD Processing and Characterization

TOPO oxidation of QD surface. Organic-soluble QDs were dissolved in tri-n-octylphosphine oxide (TOPO, Alfa Aesar) (heated to 60-70°C to liquefy the TOPO) and exposed to air for 30 minutes, 2.5 hours and 12 hours. The oxidized QDs were then water-solubilized with MAA (as above).

Ultraviolet Exposure. Solutions of QDs in PBS were placed under a 100W longwave (365 nm) UV lamp (UVP) at a distance of approximately 10 cm for 1, 2, 4, and 8 hours. The spherical irradiation was 15mW/cm² as determined with a radiometer (Cole-Parmer). For CdSe and ZnS/CdSe, the QDs precipitated between 2 and 4 hours of UV exposure, due to photo-catalyzed disulfide bond formation and subsequent loss of MAA ligands. BSA coated QDs remained soluble after 8 hours of UV exposure.

Spectroscopy. Absorbance measurements were made with a SpectraMax Plus spectrophotometer (Molecular Devices). A PerkinElmer LS45 luminescence spectrometer was used for fluorescence measurements.

QD solution images. A 1.3 megapixel digital camera (Olympus) was used to capture the white light and UV light images in **Figure 5.2A**.

5.3.4 Inductively Coupled Plasma Optical Emission Spectroscopy (ICP/OES)

5% nitric acid was added to samples of 0.25 mg/mL QDs in media to precipitate the nanoparticles, but retain the free cadmium in solution for analysis. The samples were centrifuged at 15k RPM to remove the QDs, and the solution was further diluted with nitric acid. A Perkin-Elmer Optima 3000DV was used to measure the samples and Cd standards. Calibrated emission peaks at 228.8, 214.4 and 226.5 nm were averaged.

5.3.5 Hepatocyte Culture and Viability

Hepatocytes were isolated from 2-3 month old adult female Lewis rats (Charles River Laboratories) by collagenase perfusion as previously described¹¹⁹. Less than one hour after isolation, 5×10^5 cells were seeded on 35mm wells coated with collagen I purified from rat tail tendons. Cultures were conducted at 37°C in DMEM with high glucose (Invitrogen), 10% fetal bovine serum, supplemented with 0.5 U/mL insulin, 7 ng/mL glucagon, 7.5 µg/mL hydrocortisone, 10 U/mL penicillin, and 10 µg/mL streptomycin. Twenty-four hours after seeding, spent media was removed and replaced with fresh media supplemented with QDs. After an additional 24 hours, the cultures were assayed for cell viability with MTT (Methylthiazolyldiphenyl-tetrazolium bromide, Sigma). The cells were washed with sterile PBS and a solution of 1mg/mL MTT in DMEM without phenol red was added. After one hour at 37°C, the media was removed and the purple precipitate was dissolved in 50% DMSO/isopropanol. The intensity of the purple color was measured as the absorbance at 570 nm minus background at 660 nm. Viability was determined by comparison to control cultures with no exposure to QDs.

5.3.6 Micropatterned Hepatocyte Co-Cultures and Biochemical Function

Hepatocyte/fibroblast co-cultures were conducted as described previously¹⁴³. Briefly, photoresist patterns were generated by spin-coating of S1818 photoresist on clean 2" glass wafers (Erie Scientific), exposure to UV light through a mask with 100 µm diameter features and 250 µm spacing, and development. Collagen I was adsorbed onto exposed glass domains, and remaining photoresist was removed by lift-off in acetone. The micropatterned collagen domains were subsequently treated with 0.05% BSA to block non-specific cell adhesion. Fresh hepatocytes were loaded with

EGF-QDs by incubation in suspension for one hour at 37°C in a 62.5 µg/mL solution of red EGF-QDs in media. QD-labeled hepatocytes were seeded on micropatterned substrates in serum-free media to form micropatterned hepatocyte colonies. 3T3 Fibroblasts (ATCC) were grown in DMEM with 10% bovine calf serum. The following day, 1.5×10^6 3T3 cells were seeded onto the micropatterned hepatocytes in fibroblast media, thereby producing micropatterned co-cultures.

Culture media was collected daily, stored at -20°C, and assayed for albumin secretion rates, a marker of liver-specific function, by ELISA with a horse radish peroxidase reporter conjugated to an anti-rat albumin antibody (Cappel Laboratories) using O-phenylenediamine (Sigma) as the chromogen.

5.3.7 Microscopy

Cell cultures were observed with an inverted microscope (Nikon TE200) by phase contrast microscopy or epifluorescence. Fluorescent images were acquired at $\lambda_{\text{ex}} = 540/25$ with $\lambda_{\text{em}} = 630/60$, captured by a CCD camera (CoolSnap HQ, Roper Scientific), and processed on MetaVue software (Universal Imaging).

5.4 Results and Discussion

5.4.1 Cytotoxicity of CdSe Quantum Dots *In Vitro*

In order to establish a model system for rigorous evaluation of cytotoxicity, primary hepatocytes were isolated from rats, cultured in monolayers and incubated with yellow-emitting CdSe QDs ($\lambda_{\text{em max}} = 582$ nm) for 24 hours (**Figure 5.1**). QDs were prepared using a high-temperature organometallic procedure with the solvent tri-n-octylphosphine oxide (TOPO) in an inert atmosphere¹⁷, water-solubilized with mercaptoacetic acid (MAA)⁷⁸, and delivered over a range of typical doses for both *in vitro* and *in vivo* experimentation (1.0, 0.25, 0.0625 mg/mL). We chose MAA

because it is one of the smallest solubilization ligands and thus the least protective of the QD surface¹⁴⁴. We perturbed the QD structure by exposing TOPO-capped QDs to air or illuminating with high-energy radiation and determined the influence of these parameters on cellular viability. Cytotoxicity was evaluated by MTT viability assay, a colorimetric measure of mitochondrial activity (**Figure 5.1A**), and morphologically with bright-field microscopy (**Figure 5.1B-C**).

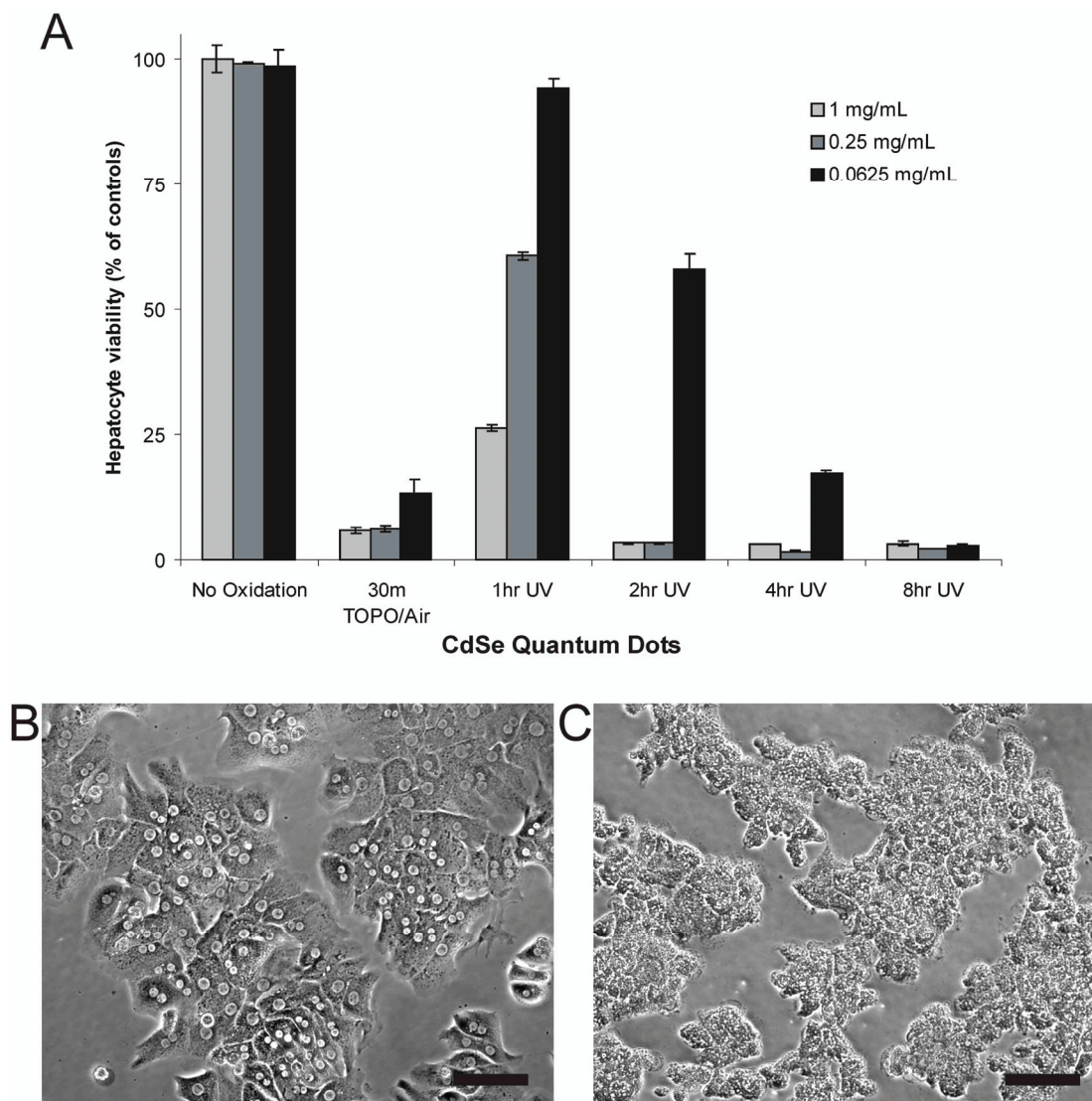


Figure 5.1 – Toxicity Of CdSe Quantum Dots In Liver Culture Model Is Dependent On Processing Conditions And Nanoparticle Dose. (A) Hepatocyte viability as assessed by mitochondrial activity of QD-treated cultures relative to untreated controls. Thirty minutes of exposure to air while TOPO-capped renders QDs highly toxic at all concentrations tested. Ultraviolet light exposure also induces toxicity that increases with exposure time and is QD concentration-dependent. Biochemical assays of viability were confirmed via phase contrast microscopy where control hepatocyte cultures exhibited distinct intercellular boundaries, well-defined nuclei, and polygonal morphology (B). Nonviable cultures (<5% of controls) exposed to cytotoxic QDs exhibited granular cytoplasm, indistinct intercellular boundaries, undefined nuclei and evidence of blebbing (C). Scale bar corresponds to 100 μm .

Our findings indicate that under standard conditions of synthesis and water-solubilization with MAA, the CdSe QDs were not cytotoxic (**Figure 5.1A**). All TOPO-capped QDs were maintained in an inert atmosphere prior to alterations. A high concentration of MAA was added to TOPO-coated QDs to render them water-soluble. However if TOPO-coated QDs were initially subjected to air for 30 minutes and then modified with MAA, a dramatic dose-dependent decrease in cellular viability was observed (from 98% to 21% at a QD concentration of 62.5 $\mu\text{g/mL}$). Based on these results, we suspected that O_2 in the air was oxidizing the surface of the CdSe QDs, leading to the observed cytotoxic effects.

To test this hypothesis, we used high-energy optical illumination to catalyze the oxidation process. Solutions of MAA-coated CdSe QDs were exposed to a UV-light source ($\lambda_{\text{em}} = 365 \text{ nm}$) with a power density of 15 mW/cm^2 for 1 to 8 hrs and then incubated with hepatocytes. Indeed, we observed a 6%, 42%, 83%, and 97% decrease in viability when cells were incubated with CdSe QDs (62.5 $\mu\text{g/mL}$) after being exposed to UV-light for 1, 2, 4, and 8 hrs (**Figure 5.1A**).

Both air and UV light have been reported to induce and catalyze, respectively, the oxidation of nanoparticle surfaces^{44, 59, 144, 145}. After exposure to an oxidative environment, we observed a progressive change in the color and absorbance profile of the QD solution, a blue-shift in the excitonic fluorescence spectra, a broad red-shifted fluorescence peak adjacent to the excitonic fluorescence peak, and a decrease in the quantum yield (**Figure 5.2A-B**). These results are in agreement with previous oxidation studies^{144, 145}. Shifts in the absorbance and fluorescence spectra occur because of a decrease in the size of the nanoparticle (loss of surface atoms due to oxidation), while the broad red-shifted fluorescence peak can be attributed to the formation of lower-energy bandgaps induced by newly formed defect structures. It has been postulated that O_2 molecules oxidize chalcogenide atoms (Se, S) located on

the surface of the QDs to form oxides (SeO_2 , SO_4^{2-})^{145, 146}. In the case of CdSe QDs, these SeO_2 molecules desorb from the surface, leaving behind “dangling” reduced Cd atoms. Thus, prolonged exposure of QDs to an oxidative environment can cause the decomposition of the CdSe nanocrystal, thereby leading to desorption of Cd ions or CdSe complexes from the core QD. In the UV-light experiment, we also observed a marked increase in cytotoxicity with oxidation time, suggesting that free cadmium was progressively released from the QDs.

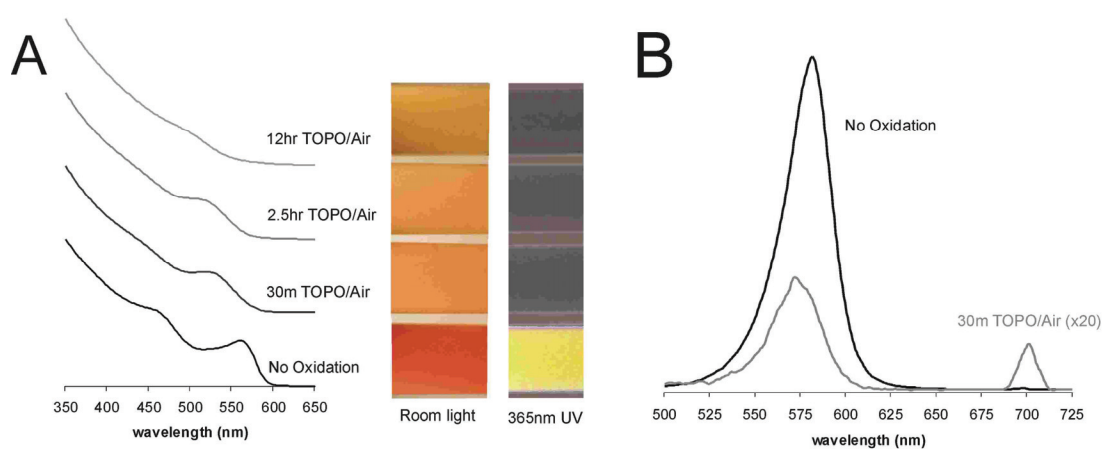


Figure 5.2 – Toxicity Of QDs Correlates with Surface Oxidation, Decrease of QD size, and Disruption of Crystal Lattice. (A) Increased exposure to air of TOPO-capped QDs correlates with surface oxidation as indicated by a blue-shift in the first quantum confinement peak and decrease in peak amplitude of absorbance spectra (in chloroform). Observable changes in color of QD solutions due to changes in absorbance spectra (white light – shift from red/orange to yellow) and fluorescence spectra (UV light – loss of fluorescence) are also consistent with surface oxidation. (B) Exposure to air of TOPO-capped QDs produces changes in fluorescence spectra (blue-shift of fluorescence peak by ~10 nm after 30 min) consistent with a decrease in QD size due to removal of surface atoms. For comparison, the amplitude of 30min TOPO curve has been increased 20 fold to compensate for the loss in quantum yield.

We theorized that release of free cadmium thereby led to cytotoxicity via conventional mechanisms of heavy metal toxicity. In order to lend credence to this hypothesis, we correlated the amount of free Cd^{2+} with the degree of observed

hepatotoxicity using inductively coupled plasma optical emission spectroscopy (ICP/OES). QD samples were processed to remove intact nanoparticles by acid precipitation and centrifugation, and the remaining solution was tested for free cadmium by ICP/OES. Since acid can slowly etch QDs, we first measured the Cd^{2+} concentration of non-oxidized MAA-QDs to determine a baseline Cd^{2+} concentration and to verify that the ICP/OES Cd^{2+} measurements were not due to acid degradation of QDs. Relatively high levels of Cd^{2+} were found both in the air-oxidized (126 ppm) and UV-exposed samples (82 ppm), while low levels were found in a solution of non-oxidized CdSe QDs (6 ppm). In our culture model, these Cd^{2+} ion concentrations correlated with high (95-98%) and low (0%) rates of cytotoxicity. This data correlates well with previous reports on rat hepatocyte cultures where exposure to 100-400 μM (11-44 ppm) Cd^{2+} ions led to significant cell death¹³⁹. Some cell types, such as cardiomyocytes, are sensitive to even lower levels of cadmium exposure (0.1 μM or 11 ppb), while other cell types are more resistant¹⁴⁰. Based on this data, it appears that surface oxidation of the CdSe nanocrystals during processing, via air-induced or UV-catalyzed oxidation, resulted in release of Cd surface atoms. The free cadmium in solution thereby rendered the QD solution cytotoxic via known mechanisms of cadmium hepatotoxicity (binding of thiol groups in the mitochondria)¹⁴¹. When the surface is not oxidized, however, the Cd atoms on the surface of the nanoparticles are bound to neighboring Se atoms and to the stabilizing ligand and are relatively innocuous.

These findings indicate that processing strategies, surface coatings, and use in biological applications that prevent surface oxidation should improve biocompatibility of CdSe-core QDs whereas oxidative environments should promote cytotoxicity. For cell-based studies using QDs, it is important to store and maintain them in an inert atmosphere (N_2) or with antioxidants, as our findings indicate that exposure to air

prior to capping can render the QDs cytotoxic. Additionally, an important implication of our findings is for *in vivo* applications (e.g. tumor targeting and imaging). We have previously observed that QDs, like other particulates, are cleared from circulation of live mice by the macrophages of the reticuloendothelial system (RES) in the liver and the spleen¹. Phagocytosis of nanoparticles would expose QDs to highly oxidative environments (H_2O_2) intended for elimination of microorganisms. We therefore tested the QD response to 1 mM H_2O_2 for 24 h *in vitro*. Our results indicate that free cadmium (24 ppm) is indeed released under these conditions *in vitro* (**Figure 5.3B**), leading to the possibility of QD toxicity in some *in vivo* applications. Strategies to protect the QD surface from highly oxidative environments or incorporation of surface coatings (such as polyethylene glycol) that promote escape from the RES may therefore be critical to the success of *in vivo* QD applications.

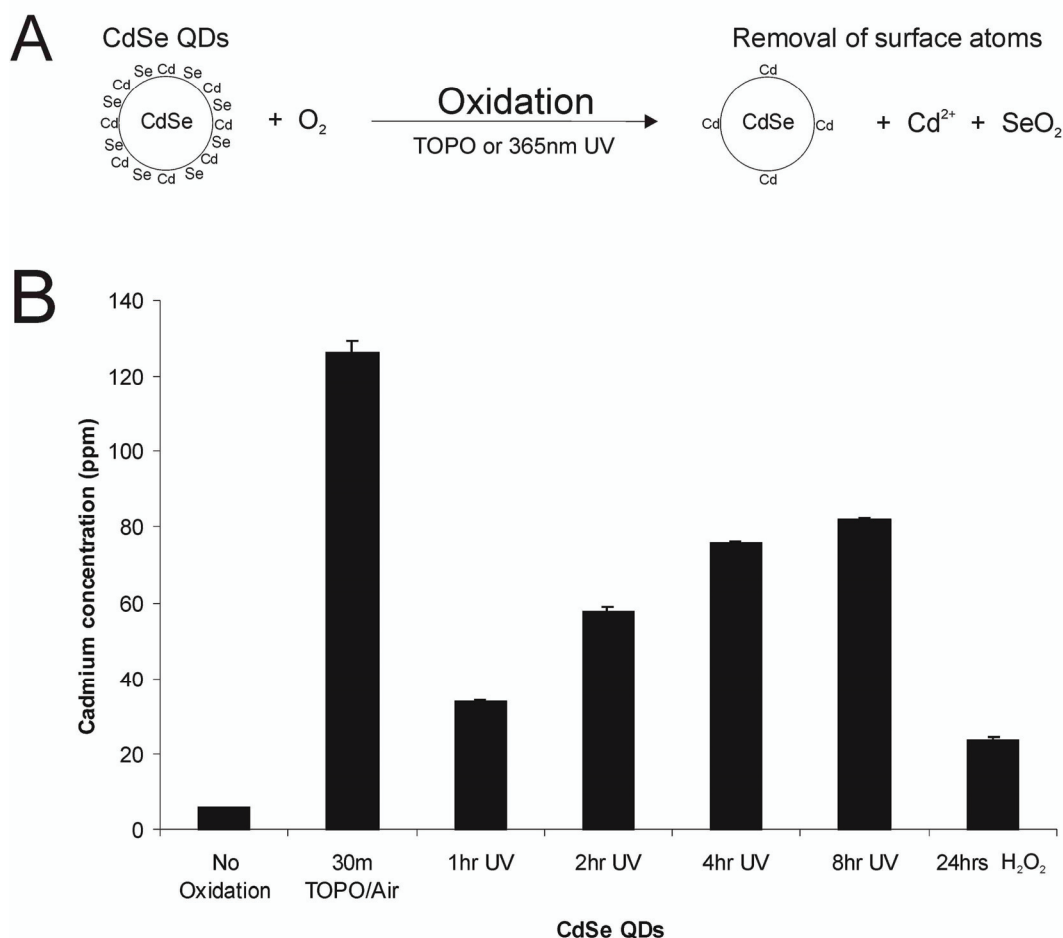


Figure 5.3 – Surface Oxidation Leads to Release of Cadmium Ions. (A) Proposed mechanism of Cd release from the QD surface via either TOPO-mediated or UV-catalyzed surface oxidation. (B) Inductively coupled plasma optical emission spectroscopy (ICP/OES) measurements of free cadmium in 0.25mg/mL solutions of QDs, indicating higher levels of free cadmium in all oxidized samples and increasing Cd levels with UV exposure time, correlating with cytotoxicity observed in Figure 5.1A.

5.4.2 Nanoparticle coatings to reduce surface oxidation

Surface ligands have been shown to decrease the QD surface oxidation by limiting transport of oxygen to the surface as has been observed for self-assembled monolayers on gold films¹⁴⁴. In a similar manner, we would expect the addition of surface

coatings (ZnS, DHLA⁵¹, BSA⁸⁶, polyacrylate⁴⁹), typically added to increase the quantum yield and stability of nanoparticles, to decrease the surface oxidation and resulting cytotoxicity.

To test the effects of surface coatings on cytotoxicity, CdSe QDs were capped with 1-2 monolayers of ZnS, yielding orange-emitting ($\lambda_{em\ max} = 600\text{ nm}$) ZnS/CdSe QDs^{44, 80}. The presence of the capping layer was confirmed by an increased, red-shifted fluorescence peak and characteristic changes in the absorbance spectra. As with the uncapped nanoparticles (**Figures 5.1-5.3**), surface oxidation was studied by treatment with: (1) exposure of TOPO-capped QDs to air for up to 12 hours, followed by water solubilization with MAA, and (2) exposure to 365nm UV light for up to 8 hours. QDs were assayed for cytotoxicity in primary hepatocyte cultures as described above.

Our findings indicate that ZnS capping virtually eliminated cytotoxicity due to oxidation by air during processing, which correlates well with previous XPS measurements showing that the addition of a ZnS capping layer renders QDs less susceptible to oxidation than the CdSe core alone⁴⁴ (**Figure 5.4A**). Spectral data indicated that the CdSe core is intact after 12 h of oxidation in air similar to previous studies, though some disruption of the ZnS cap was observed as a blue-shift in the absorbance spectra (**Figure 5.4B**). ZnS capping, however, did not fully eliminate cytotoxicity induced by UV photooxidation (**Figure 5.4A**). ICP/OES data indicated high levels of free Cd in solution after 8 h of photooxidation, confirming that the ZnS cap alone does not fully protect the CdSe core under these conditions (**Figure 5.4C**). While ZnS is less susceptible to oxidation than CdSe, the loss of sulfur atoms to form sulfate ions is possible, leaving the CdSe core vulnerable to oxidation^{145, 146}. The reported stability of ZnS-capped CdSe QDs is likely due to the relatively slow oxidation by air under ambient, uncatalyzed conditions. In contrast, high-energy radiation catalyzes this oxidation process, leading to the photodecomposition of QDs.

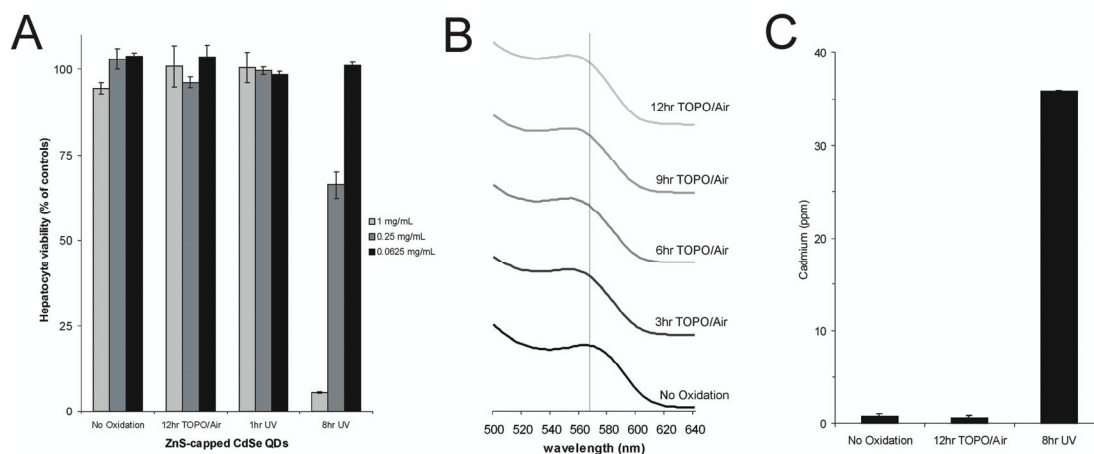


Figure 5.4 – Effects of ZnS Surface Coating on Surface Oxidation, Release of Cadmium, and Cytotoxicity. (A) ZnS capping of CdSe QDs eliminates TOPO/air-induced cytotoxicity and reduces photooxidation-mediated cytotoxicity as indicated by viability of QD-treated hepatocytes compared to Figure 5.1A. (B) While the CdSe core remains intact, the absorbance spectra of TOPO/air treated QDs displays a blue shift, possibly indicating a disruption of the ZnS cap (in chloroform). (C) Free cadmium levels measured by ICP/OES in 0.25 mg/mL QD solution correlate with patterns of cytotoxicity observed in (A).

Thus far, we have explored the influence of small organic ligands (MAA) on the photooxidative process of QDs and its affect on cytotoxicity. To explore the potential effects of large organic molecules on the cytotoxicity of QDs, we coated and cross-linked large organic-based molecules onto the surface of QDs. Bovine Serum Albumin (BSA) molecules were conjugated to the surface of MAA-coated ZnS-capped CdSe QDs with a water-based carbodiimide compound (EDAC) to produce a non-desorbable protein shell. Similar strategies have been used to coat the surface of QDs with dendrimer-like compounds¹⁴⁷, glass¹³⁴, and amphiphilic polymers⁴⁹. These types of QDs have an improved stability against flocculation, increased quantum yield, and surface ligands that allow further bioconjugation. As seen in **Figure 5.5A**, the addition of a BSA coat provided increased protection from photooxidation-mediated cytotoxicity over ZnS capping alone. Specifically, BSA-coated, ZnS-

capped QDs were found to have reduced cytotoxicity at 0.25mg/mL (98% viability) as compared to ZnS-capped QDs (66%) at the same concentration. ICP/OES measurements corroborated with these conclusions as measured by the reduction in release of free cadmium in BSA-coated dots (21 ppm) as compared to ZnS-capped QDs (36 ppm). It can be concluded that the protein-shell slows the oxidation process, likely by acting as a physical diffusion barrier for O₂ molecules to the surface. Toxicity was not completely eliminated by BSA capping, however, as evidenced by substantial cell death (95%) at the highest QD concentration tested (1.0 mg/mL) after 8 h of UV exposure. Under these conditions, spectral data also suggested significant surface oxidation (decrease in quantum confinement peak and 6 nm blue-shift in fluorescence peak) consistent with that observed for uncapped QDs (**Figure 5.5B-C**).

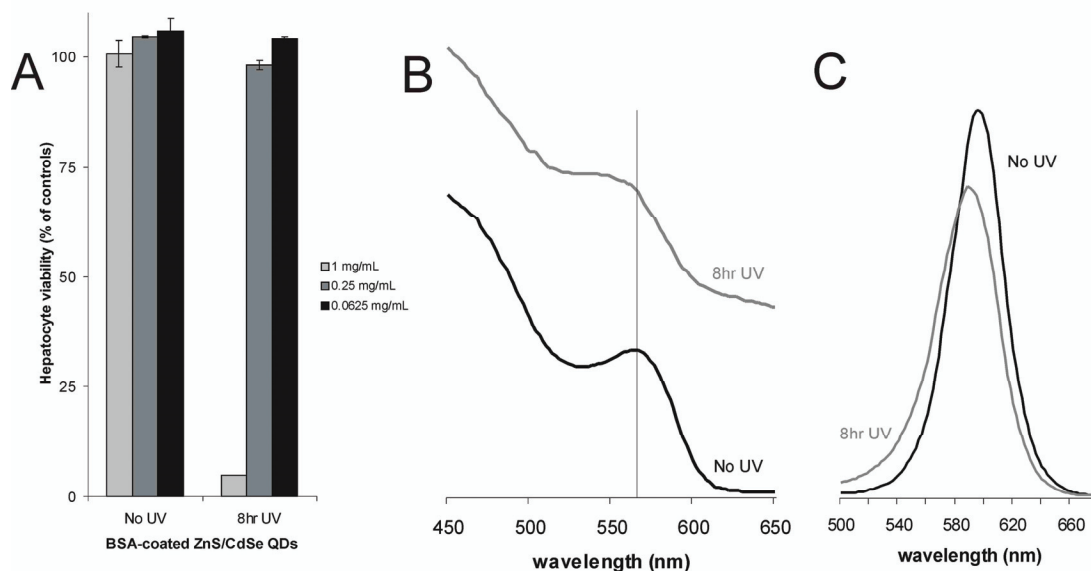


Figure 5.5 – Effects of Bovine Serum Albumin Surface Coating on Surface Oxidation and Cytotoxicity. BSA-coated ZnS-capped QDs were photooxidized with ultraviolet light and compared to unexposed controls. (A) Photooxidation of BSA-coated QDs rendered QDs toxic only at high doses (1 mg/mL) after extensive exposure (8 h). Note the reduced cytotoxicity of 0.25 mg/mL after 8 h of UV exposure (98% viability) as compared to ZnS capped dots under similar conditions (66% viability). (B) Photooxidation of BSA-coated QDs resulted in an observable change in the absorbance spectra (a decrease in the first quantum confinement peak), and (C) a change in the fluorescence spectra (a decrease in amplitude and blue-shift), corresponding to oxidation of the CdSe QD core.

To relate our toxicity results with surface coatings used by other groups, we also synthesized DHLA-capped^{51, 53, 148} and purchased polyacrylate/streptavidin-coated (Quantum Dot Corporation) ZnS/CdSe QDs. Exposure of these QDs to similar amounts of UV (8hrs at 15mW/cm²) also resulted in release of low levels of free cadmium, as measured by ICP-OES (32 ppm for DHLA QDs and 24 ppm for commercial QDs for ~250 ug/mL samples). Based on the correlation between hepatocyte toxicity and free cadmium measured by ICP, we would surmise that these QD formulations would also be cytotoxic at 1 mg/mL after UV exposure. Thus, even

with the high-performing commercially available QDs, release of free Cd over time is a concern.

In summary, the successive addition of an inorganic layer, small organic ligands, and a cross-linked organic shell progressively minimizes the cytotoxicity of QDs, increasing the biocompatibility of CdSe QDs. For typical *in vitro* cell-imaging studies, such high concentrations are not commonly used. A concentration of 1 mg/mL of QDs is approximately 10 fold higher than the concentrations used by Simon and co-workers for labeling HeLa cells⁵¹ and roughly 250 times higher than the concentrations used by Wu et al. for targeting of Her2 epitopes on breast cancer cells⁴⁹. Furthermore, for conventional long-term cell imaging studies, continuous excitation would not typically be employed. Therefore, our results indicate the upper concentration limit and light exposure at which QDs can be utilized for cell-imaging studies and that careful attention to the processing and coating details of QDs will minimize or prevent cellular toxicity.

For *in vivo* applications, however, protection of the CdSe surface from oxidation may be more critical. In two previous studies, relatively high concentrations of QDs (~100ug/mL of CdSe/ZnS) were delivered to mice through intravenous injection^{1, 55}. Once delivered to the body systemically, there are three fates for circulating particles – clearance intact through the kidney, breakdown into smaller particles, or sequestering of the particles (where they are protected from short-term breakdown, but also prevented from clearing the body). Since QD conjugates are typically spherical, greater than 7nm in diameter, and negatively charged, clearance through the kidney glomerulus is likely to be a rare event¹⁴⁹ (<0.1% clearance based on studies with albumin¹⁵⁰) unless they are first broken down into smaller particles. Our experiments suggest that, even with multiple inorganic/organic surface coatings, oxidation of the particles can occur, releasing free cadmium. While extreme conditions were used to

generate the acute cytotoxicity observed, slower release may result in chronic effects of cadmium exposure, such as kidney damage¹⁵¹. Penetration of UV light through the skin¹⁵² and/or oxidation due to inflammatory responses could induce cadmium release via surface oxidation; therefore, highly protective surface coatings would be critical to mitigating the toxicity of CdSe QDs *in vivo*. BSA and polyacrylate coatings are unlikely to be the only surface coatings that substantially reduce surface oxidation. In fact, we expect that other coating strategies currently employed or under development (i.e. polymer coatings, lipid-micelles with protein cross-linking) would offer varying degrees of protection from surface oxidation and resultant cytotoxicity. The data presented in this study should provide design criteria to quantitatively evaluate the robustness of a proposed coating strategy for *in vitro* or *in vivo* applications. Although other cadmium-containing QDs exist (CdS, CdTe), CdSe has proven to be the most utilized QD core material for biological experiments, likely due to a visible fluorescence range (blue to near infrared) and well-investigated synthesis methods. Though the other constituent elements of these QDs (Zn, Se, S) can be toxic in high doses, the concentrations exposed to the hepatocytes in these experiments are below cytotoxic levels (<4 mM)¹⁵³. Furthermore, the addition of either Zn or Se (both dietary supplements) has been shown to reduce, rather than exacerbate, cadmium toxicity¹⁵⁴.

5.4.3 Probing effects of QD on higher-order cellular functions: Application to live cell labeling

Thus far, our experiments have demonstrated that ZnS/CdSe QDs are not cytotoxic to primary hepatocytes at low concentrations (<0.25 mg/mL) and relatively short periods of UV exposure (\leq 1 hour). Working within these parameters, we sought to demonstrate the utility of QDs as a tool for long-term, live cell labeling in a sensitive

model system of liver tissue, the site of cadmium toxicity *in vivo*. Indeed, long-term, live cell labeling is one area where QDs show potential benefits over both conventional fluorescent dyes (e.g. calcein) and fluorescent proteins (e.g.. green fluorescent protein). Rather than using viability as a crude measure of toxicity, we investigated whether the migration or differentiated function of rat hepatocytes (a fragile, primary cell type) would be altered by labeling with ZnS-capped CdSe QDs.

In order to create a model of liver tissue that is stably differentiated over many days, we exploited a hepatocyte culture model we have previously developed¹⁵⁵. Specifically, hepatocytes are co-cultivated with non-parenchymal cells that promote differentiated function of hepatocytes *in vitro*. Furthermore, in order to track hepatocyte migration, we formed organized cellular arrays using a micropatterning technique described in detail elsewhere¹⁴³. Red-emitting CdSe QDs were capped with ZnS, coated with polyethylene glycol to prevent non-specific binding, and conjugated to a hepatocyte ligand, epidermal growth factor (EGF). Hepatocytes were then labeled by endocytosis of EGF-conjugated QDs ($\lambda_{em\ max} = 630\text{ nm}$) and micropatterned in arrays surrounded by fibroblasts.

On day 1 of co-culture, organized colonies of hepatocytes were identified morphologically under phase contrast microscopy and observed to correlate with red QD fluorescence (**Figure 5.6A-B**). Over 7 days in culture, hepatocytes reorganized due to cell migration. Again, phase contrast microscopy allowed correlation of hepatocyte morphology (polygonal cells with distinct nuclei) with QD fluorescence (**Figure 5.6C-D**). These data indicate the potential to label live cells for one week in culture. In addition to morphologic evidence of cell viability and microscopic evidence of cell migration, liver-specific function of these fragile, primary cells was assayed by measurement of daily albumin production. Our data indicate no deleterious effects of QD-labeling on hepatocellular function (**Figure 5.6E**) when

compared to unlabeled controls. Thus, organically-coated, ZnS-capped CdSe QDs were found to be 'biocompatible' with hepatic tissue as determined by cell viability, migration, and differentiated function over two weeks in culture. In the future, QDs could be utilized in a similar fashion to track a number of dynamic cellular processes including stem cell progeny, cancer metastases, morphogenesis, and wound healing.

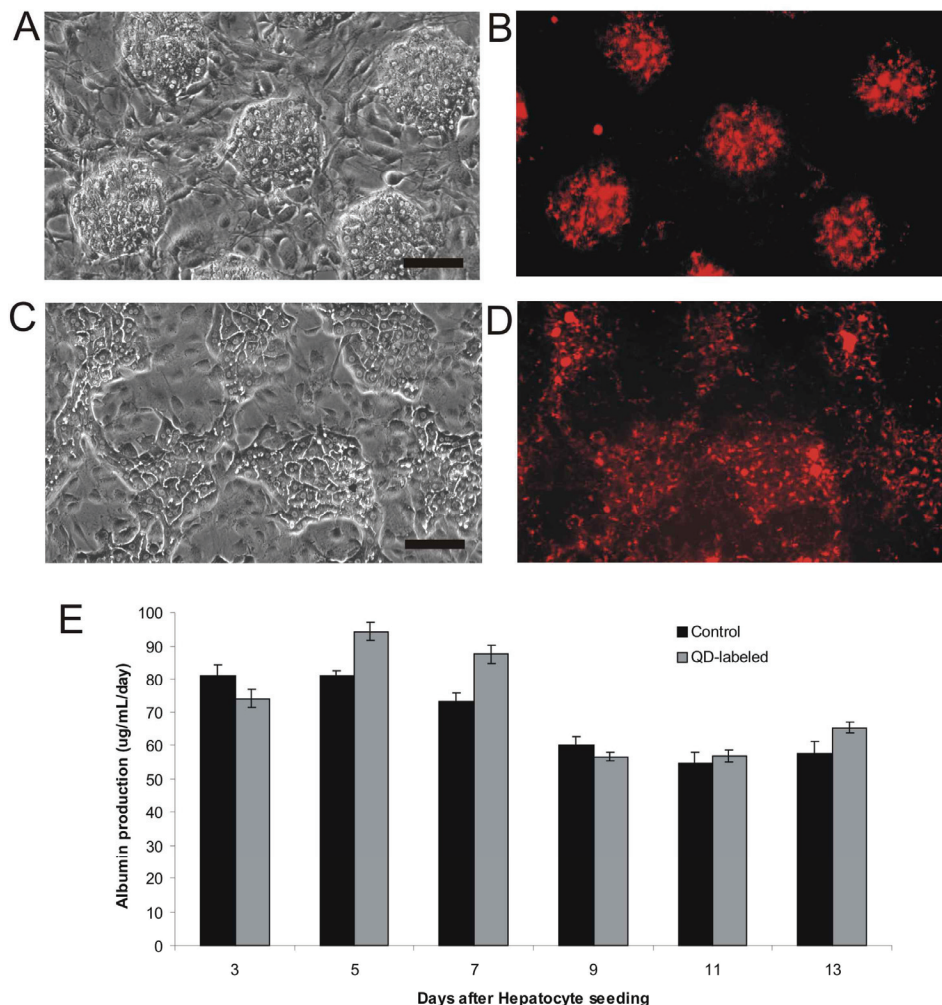


Figure 5.6 – Application of Coated QDs to Long-term Tracking of Primary Cells Without Compromising Liver-specific Function. Hepatocytes were co-cultivated with non-parenchymal cells (3T3 fibroblasts) to support liver-specific functions *in vitro*¹⁵⁵. Hepatocytes were labeled by endocytosis of EGF-coated red QDs. Co-cultures were organized in regular arrays using previously reported ‘micropatterning’ techniques¹⁴³ and cell migration was monitored by phase contrast and fluorescence microscopy. (A) Phase contrast micrograph of micropatterned array of hepatocyte colonies (~100 μm) surrounded by fibroblasts on day 1 of co-culture and corresponding fluorescence image (B) of QD-labeled hepatocytes. Scale bar corresponds to 100 μm (C) Phase contrast micrograph of co-culture demonstrates visible reorganization of hepatocyte colonies and corresponding fluorescence image (D) of QD-labeled hepatocytes after 7 days of co-culture. (E) Liver-specific functions of QD-labeled hepatocytes were comparable to control co-cultures for two weeks of culture as assessed by daily albumin secretion and averaged over two day periods.

5.5 Conclusion

In summary, we have shown that CdSe-core quantum dots are indeed cytotoxic under certain conditions. Specifically, surface oxidation through a variety of pathways led to the formation of reduced Cd on the QD surface and release of free cadmium ions, and correlated with cell death. Surface coatings such as ZnS and BSA were shown to significantly reduce, but not eliminate cytotoxicity. While many groups make use of a ZnS capping layer, synthesis methods using CdO as a precursor allow production of highly luminescent CdSe nanocrystals that do not require an inorganic capping layer^{8, 12}. Additionally, others are interested in minimizing the size of the nanoparticle shell and have made use of uncapped CdSe or CdS QDs for biological labeling experiments^{20, 156}. For these QDs, an organic capping layer must bear the burden of preventing surface oxidation, and therefore cytotoxicity.

Nonetheless, coated QDs were shown to be useful for long-term live cell labeling of hepatic tissue *in vitro* without deleterious effects on viability, migration, or differentiated function. The use of QDs *in vivo*, however, must be critically examined, as our results suggest Cd release is a possibility over time. In comparison to other nanomaterials that may exhibit novel mechanisms of toxicity due to their size (e.g. inhalation of carbon nanotubes), CdSe QDs were found to induce cell death due to their inherent chemical composition. Rather than signal an end to the future of QD labeling, these findings serve to suggest parameters for synthesis, processing, and surface coating to minimize heavy metal toxicity in biological applications and establish a quantitative framework to evaluate the potential of this and other types of nanomaterials (e.g., InP, InAs, Ag nanoparticles).

5.6 Acknowledgements

We thank Elliot Hui for assistance with micropatterning, Jennifer Felix for hepatocyte isolation, and Mike Sailor for providing facilities for QD synthesis. Funding provided by DARPA-MTO, David and Lucile Packard Foundation, NIH T32 HL07089, NIH NDDK, University of Toronto (WC), and the Connaught Foundation (WC).

This chapter was reproduced in full from Derfus AM, Chan WCW, and Bhatia SN. “Probing the Cytotoxicity of Semiconductor Quantum Dots.” *Nano Letters* **4** (2004): 11-18. The dissertation author was the primary investigator and first author on the paper. He thanks Warren Chan and Sangeeta Bhatia for their significant contributions to the work.

CHAPTER 6

REMOTELY TRIGGERED RELEASE FROM MAGNETIC NANOPARTICLES

6.1 Abstract

In the treatment of cancer, multifunctional vehicles offer the prospect of simultaneous diagnosis and therapy. In this report, we add the means to remotely trigger drug release onto a particle platform capable of image contrast. Application of electromagnetic fields to magnetic nanoparticles leads to local temperature rise, which can be used to actuate heat-labile bonds attaching drug molecules to the particle's surface. As a proof-of-concept, we demonstrate the pulsatile delivery of a single species and multistage release of two species *in vitro*, and imaging and remote actuation *in vivo*.

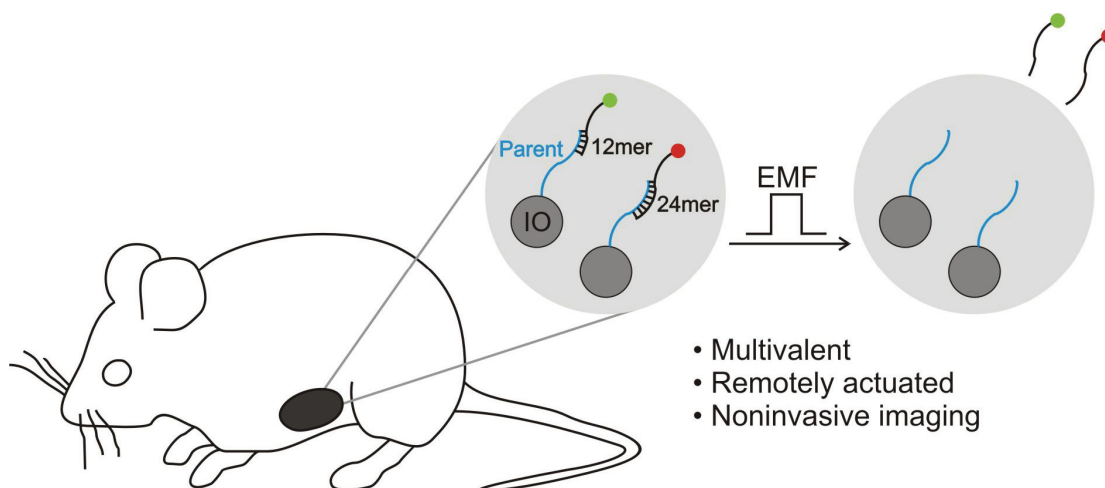


Figure 6.1 – Scheme for EMF-triggered release from magnetic nanoparticles.

6.2 Introduction

Multivalent nanoparticles have tremendous potential in the diagnosis and treatment of human disease.¹⁵⁷ Multiple surface moieties offer the ability to improve nanoparticle homing by increasing the effective affinity of targeting ligands as well as provide additional sites for conjugation of polymers that improve nanoparticle pharmacokinetics (e.g. PEG) and yet others for the attachment of therapeutic drug cargo. Drug release from a nanoparticle surface has been accomplished by bonds that are sensitive to hydrolytic degradation¹⁵⁸, or pH¹⁵; however, complex release profiles that can be controlled from large distances (>10 cm) have not been achieved. Here, we describe a multifunctional nanoparticle that is: (1) multivalent, (2) remotely-actuated, and (3) can be imaged noninvasively by magnetic resonance imaging (MRI). Superparamagnetic nanoparticles of 50 nm act as transducers to capture external electromagnetic energy not significantly absorbed by tissue (350-400 kHz) to break bonds on demand. Use of a nucleic acid strand conjugated to the nanoparticle and a model drug attached to its complement formed a tunable, heat-labile linker. The

multifunctional nanoparticles are used to demonstrate remote, pulsatile release of a single species and complex, multistage release of two species from their surface in vitro, and further used for noninvasive imaging and remote actuation upon implantation in vivo.

6.3 Materials and Methods

6.3.1 Particle preparation

Synthetic 30mer 'parent' DNA (Operon, IDT) were first conjugated to 50nm aminated magnetite nanoparticles (dextran-coated, Micromod), using sulfo-SMCC (Sigma) as the crosslinker. Particle solutions were first reacted with 1-2mg sulfo-SMCC (1 hr) to add a thiol-reactive maleimide group to the amines on the particles, and filtered with a magnetic column (Miltenyi Biotec) to remove excess crosslinker. The 'parent' oligonucleotides were synthesized containing a 5' disulfide moiety, which was reduced with 0.1M DTT for 30min at room temperature. The oligonucleotides were then filtered with a NAP-5 column (Amersham) to remove the DTT before addition to the activated particles. For a typical reaction, 5 nmol DNA was added to 5 pmol of particles (particles contained $\sim 10^4$ amine groups by fluorescamine assay). To quantify the number of oligonucleotides attached per particle (~ 100), DNA with a 3' fluorescein was conjugated, removed by hydrolysis (pH 10, 60°C, overnight) and quantified with standards.

After filtration of unconjugated parent DNA using a magnetic column, fluorescent complement DNA was added to the particles (in PBS) and allowed to hybridize overnight. For single release experiments (**Figure 6.7B**, left), fluorescein conjugated 18mer was used. For multistage experiments (**Figure 6.7B**, right), 5-FAM conjugated 12mer and HEX conjugated 24mer were separately added to particle

solutions. In all cases, dye conjugations were performed by the DNA supplier and occurred at the 5' end of the oligonucleotides. After hybridization, particles were filtered on a magnetic column at 4°C to remove unbound complement.

The sequences of DNA used in these experiments were as follows in **Table 6.1** (see **Figure 6.2** for DNA melting curves):

Table 6.1 – Oligonucleotide sequences

Name	Sequence (5' to 3')	Estimated T _m (°C)
Parent 24mer	GAAGTGC GGTTAGTCGGCTTGAATCAGCGA	71
complement 18mer	CGCTGATTCAAGCCGACTAACCGC	68
complement 12mer	TGATTCAAGCCGACTAAC	55
complement	TCGCTGATTCAA	41

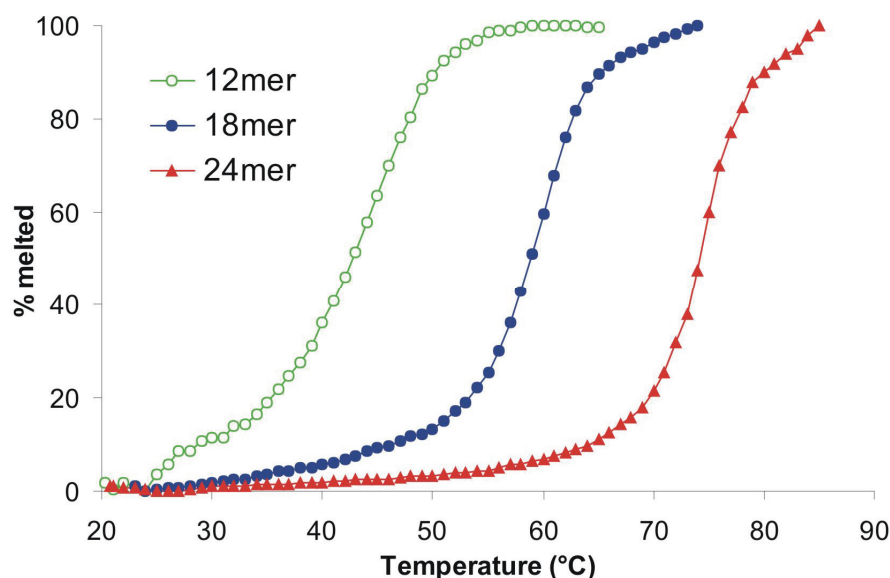


Figure 6.2 – Melting transition can be shifted by varying complement length. Equimolar concentrations of parent 30mer oligonucleotide and various complement lengths (12, 18, 24bp) were added to PBS and absorbance at 260nm was measured. Solution temperature was raised approximately 1°C per minute. Data was normalized to zero at room temperature and 100% at maximum measured absorbance. All oligonucleotides were HPLC purified and used at 0.75 μ M concentration.

6.3.2 Matrigel plug preparation

Phenol red free, growth factor reduced matrigel (400uL) (BD Biosciences) was added to 100uL of particles. To obtain 1.05% total concentration of particles, 75uL of DNA-conjugated particles (~3.3 mg/mL) were added to 25uL of similar 50nm particles (200mg/mL, Chemicell). Gels (total volume 500uL) were mixed at 4°C to prevent gelation.

6.3.3 In vitro experiments

For in vitro experiments, gels were added to polypropylene microcentrifuge tubes and incubated at 37°C for 45m to allow gelation. Gel plugs were then washed three times with 500uL of PBS over 15m. 200uL of buffer was added to the plugs and 150uL samples removed at 10m intervals. Remaining supernatant was discarded at each time point. When treated with EMF during a time interval, fields were switched on for 5m only, preceded by ~2.5m and followed by ~2.5m at room temperature. When fields were not applied during an interval, samples remained at room temperature. Supernatant samples was assayed on a plate-reader fluorometer (Molecular Devices Gemini XS) and amount of DNA quantified with standards.

For single fluor release experiments (Fig 1B), samples were exposed to 5m, 1.25kW EMF pulses, which yielded a final gel temperature of 60°C. For the dual fluor case (Fig 1C), 0.55kW (52 °C) and 3.0 kW fields (75 °C) were used.

6.3.4 Conductive heat transfer model

Experimental data was obtained using the setup in **Figure 6.3**.

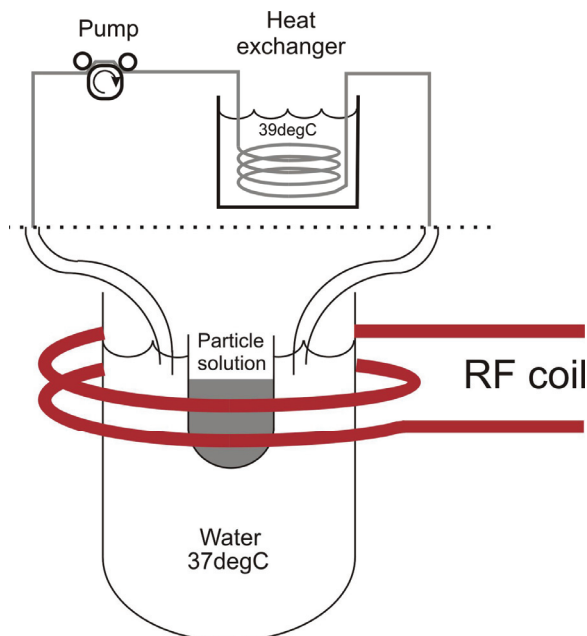


Figure 6.3 – Experimental Setup for conductive heat transfer measurements.

The concentration of iron oxide nanoparticles in solution was varied (1, 4, 7, 10 mg/mL) along with sample volume (50, 125, 250, 500, 1000 uL). To ensure near-spherical sample shape, various tube sizes were used. Maximum EMF power (3kW) was applied for 5min (time required for largest volume to reach steady state). Temperatures measured with a K-type thermocouple, immediately after the field was turned off. The data was fit to a conductive heat transfer equation, assuming steady state, spherical geometry and an infinite surrounding bath. The data and curve fit were plotted with Matlab and appear in **Figure 6.4**.

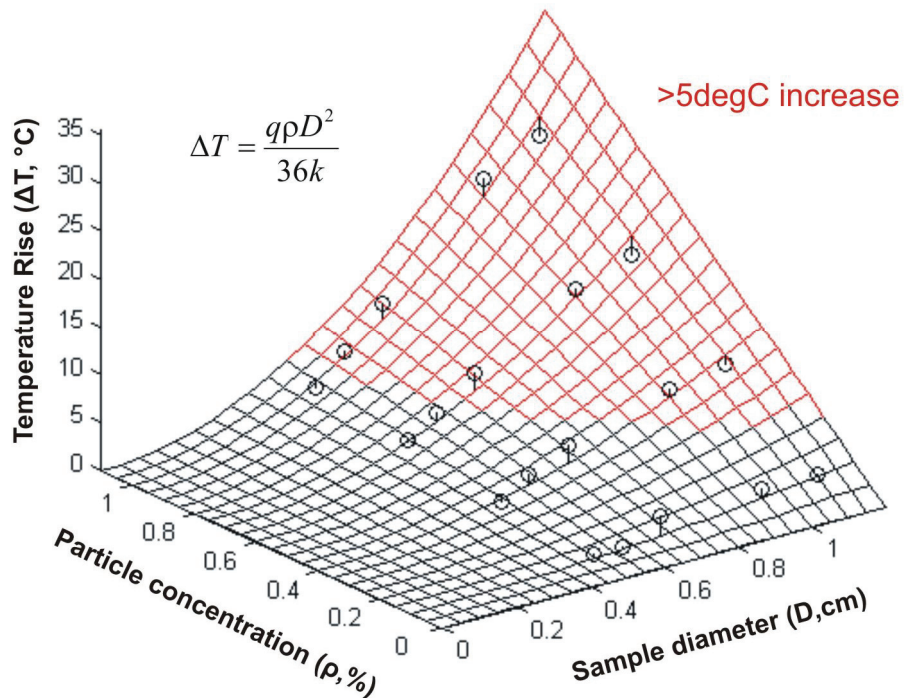


Figure 6.4 – EMF-induced temperature rise varies with particle concentration and sample diameter. Experimental data (open circles) was collected by applying maximum EMF (3kW power) to solutions of various diameters (D) containing various concentration of magnetic particles (ρ). These data were fit to a conductive heat transfer equation (inset), where k is thermal conductivity (for water: 0.64 W/m°C), and q is the heating rate (mW/mg). With a threshold of 5°C temperature rise to affect release, a minimum of 1.2 mg particles must be delivered to a 1cm diameter tumor.

After completion of release experiments, it was observed that larger temperature gradients between the matrigel plug center and edge could be obtained by modeling non-steady state behavior (shorter time intervals). Experiments were performed to confirm these results (**Figure 6.5**).

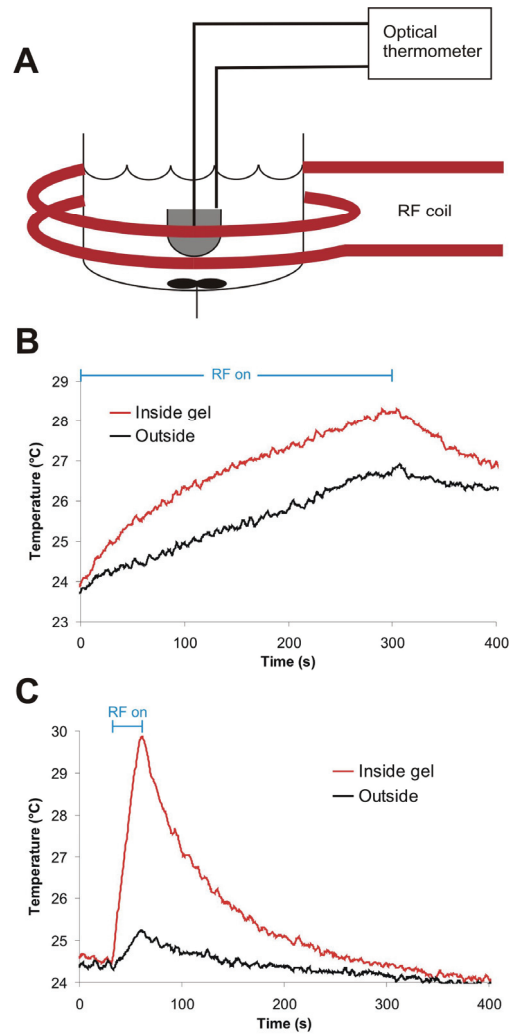


Figure 6.5 – Shorter heating intervals applied to higher particle concentrations reduces collateral heating. While all release experiments were performed with 5 minute heating intervals, heating of normal tissues surrounding tumors would be disadvantageous at these long intervals. Here, we applied EMF to gel plugs containing magnetic particles and monitored the temperature inside and at the plug edge (A). In (B), EMF was applied for 5 min to a 500uL gel plug containing 1mg particles, yielding a 4.3°C rise inside the plug and a 3.2°C rise at the plug edge. (C) By reducing the heating interval ten fold (30s), a higher particle concentration (7.5 mg per 500uL plug) was required, but resulted in an improved differential between gel temperature rise (5.4°C) and exterior rise (0.8°C).

6.3.5 In vivo experiments

Prior to injection of matrigel plugs into mice, approval from the Burnham Institute Animal Use Committee was obtained (AUF 05-054). In these experiments, 500uL volumes were injected subcutaneous near the posterior mammary fat pad of six athymic nude mice and allowed to gel for 45m. Prior to injection, animals were anesthetized with Avertin (tribromoethanol) and remained under anesthesia during the remainder of the experiment. Three animals were treated with EMF for two 5min doses, with 15m between field applications (+EMF), while three were not treated (-EMF). For treatment, mice were placed inside a plastic tube, which was mounted inside a horizontal two-turn copper coil. The tumor phantom was centered in the coil cross-section (see below in **Figure 6.6**).

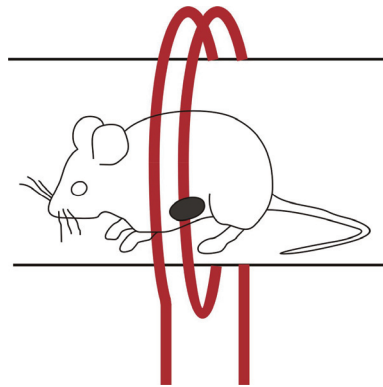


Figure 6.6 – Experimental setup for EMF application to tumor phantoms.

During EMF application, the temperature of the skin surface adjacent to the implanted plug was monitored with an optical thermocouple (Luxtron I652). Temperatures rose to 45-50°C by the end of exposure period. While we did not measure the temperature inside the implant, our model predicts a steady state temperature of 60 °C (23 °C rise) at the plug implant core, and 52 °C at the plug edge based on the particle concentration and volume injected (see **Figure 6.4**). In vitro

release from a similar plug heated with EMF for 5 min to 60°C showed a ~4 fold increase in release of fluorescein-labeled 18mer over 37°C control (not shown) and ~16 fold release over 23°C control (**Figure 6.7B**).

One hour after EMF treatment, animals were sacrificed. Tumor phantom and surrounding tissue (fascia and skin) were removed and embedded in OTC for histology. Sections were stained with DAPI and an anti-fluorescein antibody (followed by fluorescein conjugated secondary) to amplify small signals. To quantify penetration depth, 8 images of the tissue/phantom boundary were taken for each animal (3 animals per group, 24 images total). DAPI staining was used to demarcate the boundary between the two regions. Using Metamorph software (Universal Imaging), green fluorescence on the tissue side of the boundary was quantified. For each fluorescent “object”, the area and distance from the tissue boundary was measured. An area-weighted average distance was calculated. For the +EMF case, this value was 250 +/- 11 microns. For the -EMF group, the mean distance was 42 +/- 3 microns. The entire set of images appears as **Figure 6.9** and **Figure 6.10** below.

6.3.6 Radiofrequency electromagnetic field applicator:

A 3kW induction heating power supply (Ameritherm Nova 3) was used with a remote heating station and custom-made coils. The coil for in vitro experiments was 2.5-turns, 12mm ID, and resonated at 400 kHz. For the heat transfer model and mice experiments, a 2-turn, 30mm OD coil resonating at 338 kHz was used. All coils were constructed from 4.88 mm OD copper tubing and spray-coated with insulating paint. During experiments, cooling water (10-16°C) was circulated through the coil.

6.3.7 MR imaging:

T1-weighted data sets of mice implanted with iron oxide particle containing gel plugs were acquired using a horizontal bore 7-Tesla imaging spectrometer (General Electric). T1-weighted acquisition was intended to achieve good anatomical detail. Data were acquired using a custom small animal imaging coil. Imaging parameters included a spin echo sequence, TR 500, TE 12, 40 mm field of view, matrix 256x256, slice thickness 0.5mm.

6.4 Results and Discussion

In **Figure 6.7B** we demonstrate pulsatile release of a fluorophore by electromagnetic field (EMF) pulses (400 kHz, 1.25 kW) of 5 minute duration every 40 minutes. Such a profile would be useful for metronomic dosing of a cytotoxic or cystostatic drug. The use of nucleic acid duplexes as a heat-labile linker has the additional feature of temperature tunability through changes in chain length and variations in G/C content. In **Figure 6.7C** we use oligonucleotides of two different lengths and corresponding fluorescent species (12mer, FAM; 24 mer, HEX) to demonstrate the potential for complex release profiles. Low power EMF pulses (0.55 kW) trigger release predominantly of FAM by melting of the 12mer whereas higher power (3 kW) led to simultaneous release of both species. Such a profile could be used to release multiple drugs in series, synergistic drug combinations such as a chemosensitizer and chemotherapeutic, or combination regimens such as antiangiogenic and cytotoxic compounds.¹⁵⁹

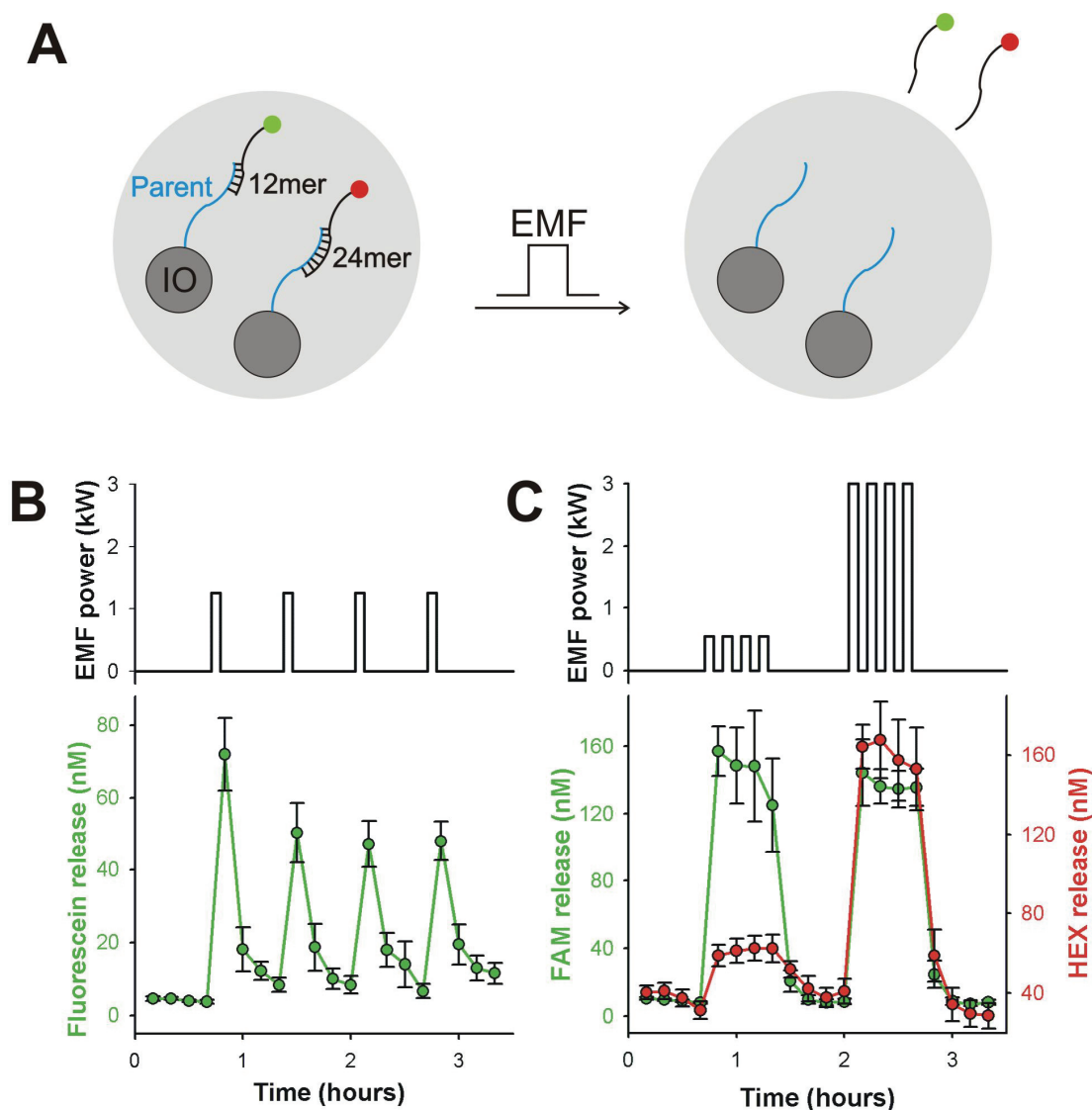


Figure 6.7 – Superparamagnetic nanoparticles transduce external electromagnetic energy to heat, thereby melting oligonucleotide duplexes that act as heat-labile tethers to model drugs (A). (B) In vitro, nanoparticles hybridized to fluorescein-conjugated 18mer were embedded in hydrogel plugs. Repeated EMF pulses of 5 minutes resulted in corresponding release of fluorescein. Alteration of oligonucleotide duplex length shifts response of heat-labile tether enabling complex release profiles. Low power EMF exposure results in release of FAM-conjugated 12mer whereas higher power results in simultaneous melting of both 12mer and 24mer tethers (C).

Next, we explored the use of the multifunctional nanoparticles in vivo by implantation of a subcutaneous tumor phantom consisting of a matrigel plug

containing nanoparticles in living mice. We examined the release of a model drug by EMF exposure of 3 kW and 5 minutes. Fluorescent micrographs of histological sections in **Figure 6.8A-B** depict a dramatic increase in penetration depth of the model cargo into surrounding tissue due to EMF exposure. Image analysis was performed on 24 fluorescent images from each group (3 animals, 8 images each, **Figures 6.9 and 6.10**). The average distance of fluorescence signal from the tissue/phantom boundary in animals treated with EMF was approximately six-fold over unexposed controls (250 +/- 11 microns vs. 42 +/- 3 microns). Such an increase in penetration depth could prove useful for treatment of peripheral disease – areas often underdosed in hyperthermia generated by thermal seeds.¹⁶⁰ The use of the particle core to transduce external EMF energy to break local bonds is an advantage over near-infrared light and other potential remote triggers that are more efficiently absorbed or scattered by tissue.⁶⁵ At 400 kHz, field penetration into 15 cm of tissue is >99%,¹⁶¹ yet absorbed power density due to eddy current heating is generally an order of magnitude less than due to implanted particles.⁷⁰ Finally, **Figure 6.8C** depicts the noninvasive visualization of the nanoparticles by magnetic resonance imaging, demonstrating the potential utility as both diagnostic and therapeutic vehicles.

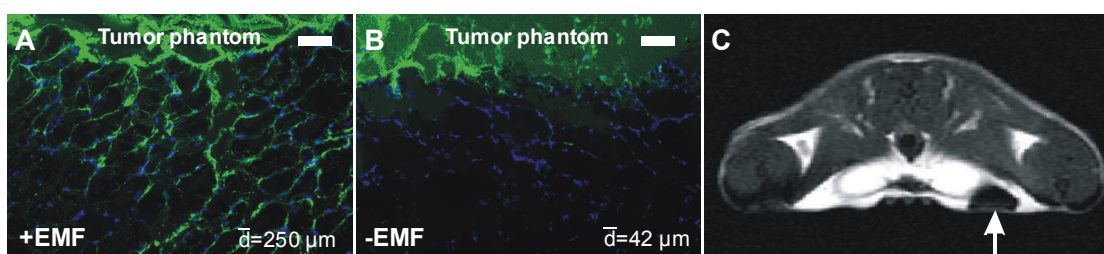


Figure 6.8 – Release from nanoparticles in vivo. Multifunctional nanoparticles were mixed with matrigel and injected subcutaneously near the posterior mammary fat pad of mice, forming tumor phantoms. Application of EMF to implanted phantoms with 18mer tethers resulted in release of model drugs and penetration into surrounding tissue (A) when compared to unexposed controls (B, scale bar = 100 microns). These mice were imaged with a 7T MRI scanner, and a transverse section is shown in (C) (arrow indicates tumor phantom).

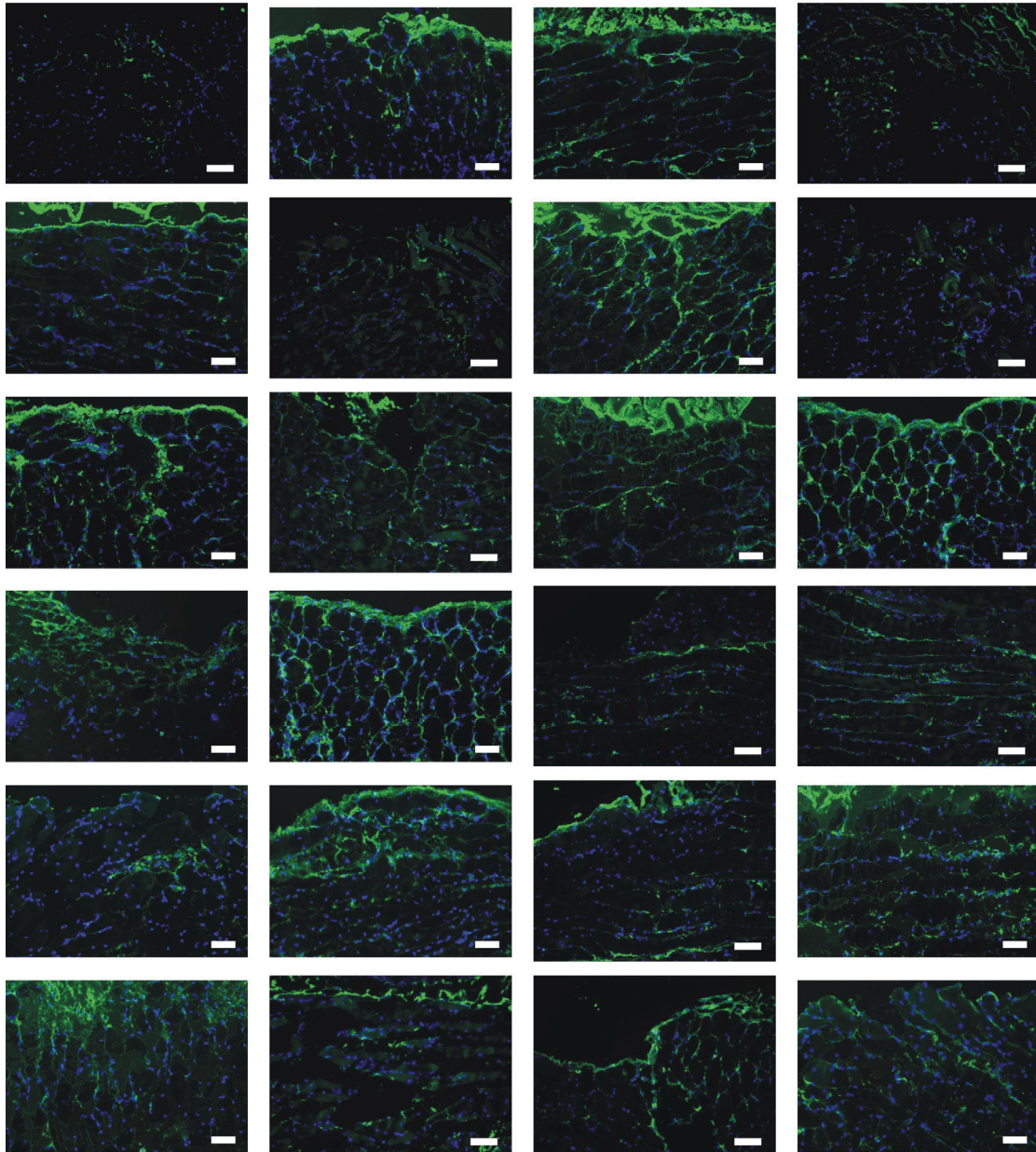


Figure 6.9 – Images of tissue/phantom boundary in +EMF group used to quantify penetration depth. Scale bar = 100 microns.

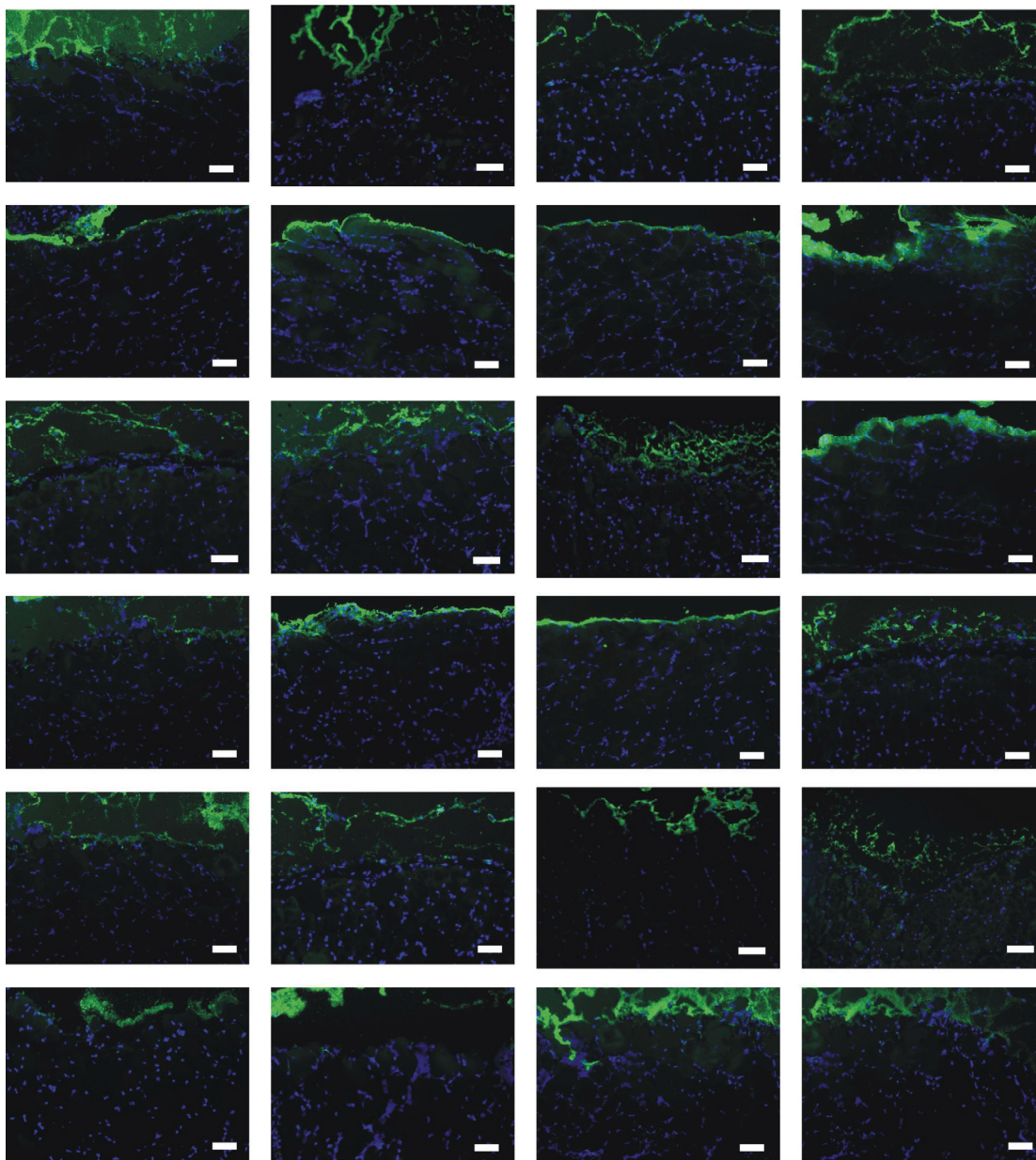


Figure 6.10 – Images of tissue/phantom boundary in -EMF group used to quantify penetration depth. Scale bar = 100 microns.

6.5 Conclusion

In our view, the fabrication of integrated, multifunctional nanodevices offers the potential to shift the current paradigm whereby diagnostics and therapeutics are

sequential elements of patient care. In this example, nanoparticles could be delivered intravascularly using homing peptides¹, used to visualize diseased tissue by MRI and then to guide focused application of electromagnetic energy, ultimately enabling remote, physician-directed drug delivery with minimal collateral tissue exposure. The performance of these devices can be improved in the future by new materials and chemistry. Particle cores with higher magnetization would result in greater heating efficiency, requiring a lower particle concentration for release. Additionally, an improved heat-labile tether, with a sharp temperature transition slightly above 37°C, might be obtained by attaching several duplexes in parallel.¹⁶² Nevertheless, the scheme outlined here demonstrates the potential to remotely trigger release from a nanoparticle, a modular function compatible with other nanoscale treatment platforms (e.g. gold nanoshells⁶⁵, carbon nanotubes¹⁴).

6.6 Epilogue

The discussion above focuses on the release of therapeutic agent from particles targeted to a disease site through the systemic circulation. Our release strategy may find use in another realm as well – triggered release from an implanted drug-eluting reservoir. For drugs that must be taken regularly, some groups have proposed the implantation of microchip-like devices to meter these medications.^{163, 164} Doses of a drug are contained in small wells capped with a thin gold layer. Current is passed through the gold cap, leading to corrosion and release. One drawback, however, is that these devices require an implanted power source, which increases the overall footprint. Later generations of the device utilize polymer degradation, rather than electrical current, to control release.¹⁶⁵ While there are no metallic parts in this formulation, it also does not allow the customization of release profiles after

implantation. Hydrogels containing the releasable particles described above would over both of these issues.

Admittedly, our strategy has the drawback of generating a local temperature rise in the area of the implant. In some cases, however, such as the implantation of a drug-eluting reservoir after tumor resection, this heating may have additional, therapeutic effects. In an effort to preserve the surrounding tissue, tumor cells at the boundaries of the resected region are often left behind after surgery. To reduce the chances of remission, drug-eluting reservoirs are placed at the resection site and slowly release anticancer medication. Gliadel wafers, for example, are FDA-approved reservoirs of the chemotherapeutic carmustine, or BCNU, used to treat brain tumors.¹⁶⁶ Release from these wafers occurs as the polymer wafer degrades and is not controllable after implantation. If a hydrogel containing our releasable particles were implanted instead, release could be controlled on demand and multiple drugs released in a prescribed order.

With this motivation in mind, we developed a system for the encapsulation of magnetic particles into calcium alginate hydrogel beads. Calcium alginate was chosen due to a pore size large enough to allow the diffusion of small molecule drugs and short oligonucleotides out of matrix, but tight enough to trap the 50nm magnetic nanoparticles. The fabrication of these beads is described in **Figure 6.11**. Dextran-coated iron oxide particles are first conjugated to 30mer parent DNA strands using the sulfo-SMCC crosslinker. Particles are mixed with a 1.5% sodium alginate solution (Keltone LV), and added dropwise to a 150mM calcium chloride solution. After 10 minutes, beads were washed and added to solutions of fluorescent oligonucleotide of 12, 18, or 24 base pairs. After hybridizing for 24 hrs at room temperature, beads were washed an additional 24 hrs to remove unbound complement. The resulting beads are approximately 3mm in diameter and black in color.

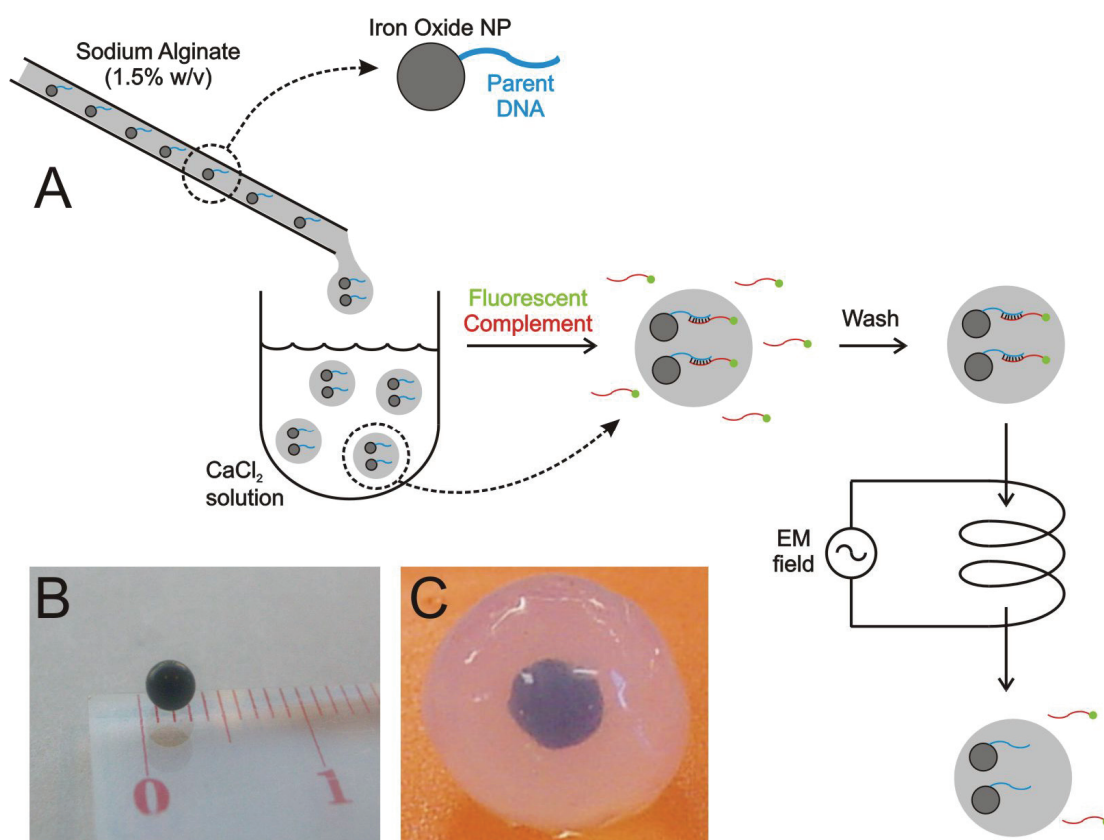


Figure 6.11 – Scheme for fabrication of alginate beads containing releasable particles. Alginate beads are prepared by the dropwise addition of magnetic particle/sodium alginate solution into a calcium chloride solution (A). The resulting beads are nearly spherical and ~3mm in diameter (B). For applications where heating of the surrounding tissue is not tolerable, a gel overcoat can be added to the beads to aid in heat dissipation (C).

These beads were then characterized by scanning electron microscopy (SEM) and fluorescence imaging (**Figure 6.12**). SEM images were taken on an FEI Quanta 600 in high vacuum mode. Beads were first dehydrated with a graded ethanol series, critical point dried using carbon dioxide, and sputtered with gold prior to imaging. The images indicate a tight pore size (<50nm) on the surface of the beads, but a looser network (~200nm pore size) on the interior (**Figure 6.12B**). Fluorescence imaging of a bead cross-section reveals signal on the interior of the bead, indicating that the

fluorescently labeled complement strand has diffused and bound throughout. The fluorescence, however, does appear brighter at the bead edge.

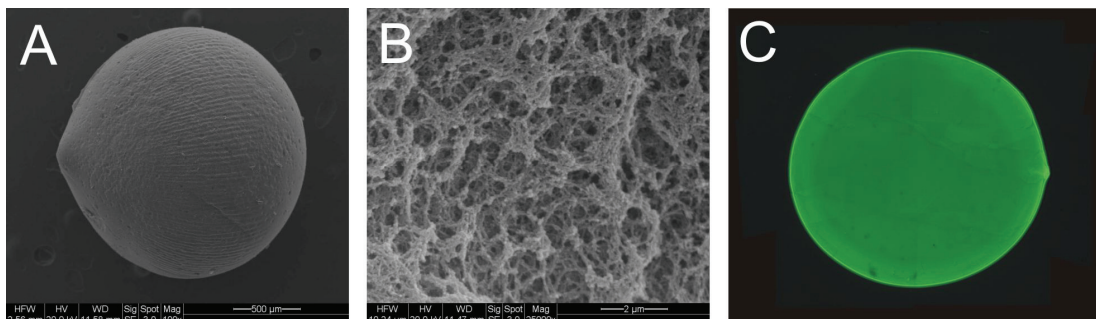


Figure 6.12 – Characterization of magnetic particle hydrogels. Whole beads (A, 100x) and bead cross-sections (B, 25000x) were examined by SEM. The beads are near-spherical and have a tight pore network on their surface, which was not quantifiable by SEM. The interior of the beads, on the other hand, contains a much looser pore network. A bead cross-section was also examined by fluorescence microscopy, revealing complement DNA bound throughout the bead (C).

6.7 Acknowledgements

The authors thank Miriam Scadeng for MR imaging, Evelyn York for SEM imaging, and acknowledge financial support of the David and Lucile Packard Foundation, the National Cancer Institute of the National Institutes of Health (Contract No. N01-C0-37117). AMD thanks the UC Biotechnology Research and Education Program for a G.R.E.A.T. fellowship (#2004-16).

This chapter was reproduced in part from Derfus AM, von Maltzahn G, Harris TJ, Duza T, Vecchio KS, Ruoslahti E, Bhatia SN. “Remotely Triggered Release from Magnetic Nanoparticles” (submitted to *Nature Nanotechnology*). The dissertation author was the primary investigator and first author on the paper. He thanks Geoff von Maltzahn, Todd Harris, Tasmia Duza, Ken Vecchio, Erkki Ruoslahti, and Sangeeta Bhatia for their significant contributions to the work.

CHAPTER 7

SUMMARY AND CONCLUSIONS

7.1 Perspectives on siRNA delivery

In chapters two through four, we progressed toward a siRNA vehicle that allows gene silencing and quantification of delivery. Co-attachment of QDs and siRNA to a common vehicle fixed the ratio of the two species, allowing cellular fluorescence to serve as an easily-quantifiable proxy for nucleic acid delivery. Quantum dots are more stable in a cellular environment than organic dyes, and use of these particles allows the monitoring of transfected cells as their gene expression changes over several days. Cationic liposome reagents served as an initial means for this co-delivery, and remain the most useful technique for in vitro observations. With the goal of clinical use, however, we transitioned this platform to a smaller, more stable form-factor. Direct attachment of siRNA to QDs using heterobifunctional crosslinkers fixed the ratio between the two species. Tumor homing peptides were added to the vehicle to achieve cell uptake, and potentially allow systemic targeting. Endosomal escape of these QD/siRNA/peptide conjugates, however, remains to be solved.

Looking forward, systemic delivery of the conjugate carries new challenges, as the RNA cargo must be sufficiently protected from nuclease enzymes during transit. One hope is that the vehicle may sterically hinder RNase, due to its large size and close proximity of siRNA to the particle's surface. Early experiments with gold colloids, however, indicate the degradation rate is not decreased (D-H Min). Co-

encapsulation of particles and siRNA into a polymer matrix may improve the stability, but would increase the overall size of the conjugate. The use of alternative nucleic acids that are resistant to nucleases is another option, though increases in synthesis costs would be significant.

Another hurdle to successful *in vivo* use is the targeted delivery of particles to tumors. Though attachment of the F3 peptide is intended to perform this function, the lack of success with homing iron oxide particles by the group has raised concern (D. Simberg, T. Duza). These results are in sharp contrast to the success achieved by the group when targeting quantum dots to tumors (F3, Lyp-1) and normal lung (GFE) with phage-display derived peptides¹. In reconciling these seemingly disparate results, it may be useful to examine differences in the particle (size and coating), and peptide (number and sequence) components. The quantum dots used in the Akerman/Chan experiments were 3.5-5.5 nm in size with a small (~1nm) mercaptoacetic acid coating prior to addition of PEG-thiol and peptide to the surface. Light scattering of similar conjugates (Chapter 2) gives a total hydrodynamic size of 25-30 nm, though this estimate may be slightly exaggerated due to the high mobility of the PEG chains. Akerman and Chan estimated 120 (no PEG) or 70 (with PEG) peptides per QD. On the other hand, iron oxide particles are typically coated with a crosslinked dextran layer (giving an overall size of 50-70 nm), with ~100-1000 peptides covalently linked to their surface. Accessibility of the peptide target may be important, as CREKA (a pentapeptide used for iron oxide experiments) targets the extracellular matrix (particles may be too large to extravasate), but F3 and Lyp-1 home to vessels (vascular or lymphatic). Particle size may also play a large role, as Weissleder and coworkers have shown success targeting smaller iron oxide particles with small molecules¹⁶⁷. These particles also demonstrated a long (>10 hours) circulation half-life, and small molecule libraries were screened specifically for

nanoparticle homing. Differences in phage and iron oxide particles may require novel, particle-specific homing peptides, and schemes must be identified to screen for these sequences.

In summary, the targeting of larger (30-100 nm) nanoscale conjugates is not straightforward and requires extensive further investigation. In the meantime, however, siRNA-laden particles can be directly injected at the tumor site. A peptide ligand will still be required for uptake, but systemic targeting is not needed immediately. Freeing the particles from the endosomal compartment and protecting the particle cargo from nuclease enzymes, on the other hand, will require more immediate solutions.

7.2 Potential for clinical use of quantum dots

Due to curiosity about the stability of their cadmium-containing cores, we explored the potential cytotoxicity of quantum dots in chapter five. When added to hepatocyte cultures, CdSe and ZnS-capped CdSe quantum dots are not acutely cytotoxic to cells, even in high concentration (1 mg/mL). Similar observations in vitro and in mice have led many groups to claim that quantum dots are safe for clinical use^{2, 51, 55, 168}. While this conclusion is perhaps correct, the methodology is rather unscientific. Long-term use of quantum dots in humans may lead to unintended consequences and only long-term animal studies with repeated doses of particles may uncover these issues.

Partially by accident, we observed that the breakdown of the CdSe core is possible in oxidative conditions. While this finding had been previously investigated^{44, 144}, these groups focused on the consequences for fluorescence, rather than the side products of crystal degradation. We initially observed effects of degradation on the viability of hepatocyte monolayer cultures. The effects of oxidation (catalyzed by

heat or UV light), were dose-dependent, as longer time periods in an oxidative environment lead to increased toxicity. We hypothesized that the mechanism of cell death was cadmium-related, and confirmed this association by measuring the Cd content of the oxidized QD solutions with ICP-OES. The addition of 1-2 monolayers of ZnS and a BSA coating reduced the degradation significantly, and conjugates of this sort can be used in vitro with a low risk of cytotoxicity.

We did, however, observe Cd release from ZnS-capped and BSA coated quantum dots after 8 hours of UV exposure. Breakdown of purchased quantum dots (QDC) also occurred in this environment. Initially, some reviews of our work suggested that this funding will limit the clinical use of quantum dot bioconjugates. Rather, we believe that these findings merely serve as a quantitative guideline for practical use. The rate of particle breakdown and delivery of repeated doses will be important in calculating an estimated cadmium load. Chronic cadmium exposure can damage the kidneys and liver (and may be carcinogenic), but only when a threshold is reached. Very small levels are routinely absorbed from the environment and can be efficiently sequestered by the metal-binding proteins in the liver (e.g. metallothionein). Additionally, the stage of disease must be taken into account. If the use of quantum dots provides sufficient benefit, the risk of cadmium exposure can be managed.

With quantum dots, as well as other nanoparticles, further investigation into the eventual clearance of these materials must be considered. Many nanoparticles are too large to be excreted through the kidneys. Some groups have observed the presence of intact nanoparticles in the bile (S. Wickline, personal communication) or feces (Ballou et al, unpublished), though this route is unexpected. In general, particles will be broken down and their products excreted or absorbed by the body. As a result, chronic affects of these materials are likely to be related to the effects of their

constituent materials. In some cases, however, the aspect ratio and shape of particles must be considered, as it might enable a novel cytotoxic mechanism (e.g. carbon nanotubes).

7.3 Improving the feasibility of remotely triggered release

Leveraging the unique physical properties of nanomaterials to perform previously impossible treatment tasks has led to much excitement surrounding bionanotechnology. In chapter six, we explored a scheme to remotely trigger the release of therapeutic from a nanoparticle carrier by exploiting one of these unique features. In the presence of an alternating magnetic field, superparamagnetic nanoparticles will rotate through their medium (Brownian relaxation), or reorient their magnetic moment (Neel relaxation) to achieve a lower energy state. Repeated realignment leads to energy loss in the form of heat. While heat is generated locally at the particle, the heat produced by a single particle is insignificant⁶⁸. Yet, if a population of particles are present in a volume, the temperature can be raised several degrees. We harnessed this remote heating phenomenon to remotely cleave a heat-labile bond. As a proof-of-concept, we utilized a DNA duplex linker to connect a fluorophore (model drug) to the surface of dextran-coated iron oxide.

While our initial results offered a glimpse of the potential use of this technology (tunable, multistage release, *in vivo* use), practical application of this scheme will require crossing several hurdles. First, a significant quantity of iron oxide (1.2 mg in a 1cm diameter tumor) must be delivered to achieve even a 5 degree temperature rise. Systemic targeting of this quantity may be possible, though current hyperthermia treatments utilize direct injection of particles in the tumor site^{73, 74}. Potentially, higher strength electromagnetic field and improved particle magnetization may lower this

threshold as well. Second, the DNA duplex linker is not ideal, due to its broad temperature transition and high melting temperature. Perhaps a chemical linker could be designed (or screened for) with a sharp transition to instability at temperatures of 40-42 degC, though little evidence of such a linker exists in the literature. More practically, several nucleic acid linkers might be used in parallel, so that cooperative effects between the strands lead to a sharp melting point¹⁶². Finally, the therapeutic to be released must be inactive until release. Likely, delivered particles will be internalized by target cells, as well as macrophages in the liver and spleen. To enable timing of release and reduce off-target effects, the drug activity should be greatly hindered by attachment to the particle and cellular removal (e.g. in the endosomes) of the drug from the particle minimized. Obviously these concerns will require extensive further investigation, but the barriers to practical use do not appear insurmountable.

REFERENCES

- (1) Akerman, M. E.; Chan, W. C.; Laakkonen, P.; Bhatia, S. N.; Ruoslahti, E., Nanocrystal targeting in vivo. *Proc Natl Acad Sci USA* **2002**, 99, (20), 12617-21.
- (2) Gao, X.; Cui, Y.; Levenson, R. M.; Chung, L. W.; Nie, S., In vivo cancer targeting and imaging with semiconductor quantum dots. *Nat Biotechnol* **2004**, 22, (8), 969-76.
- (3) Remsen, L. G.; McCormick, C. I.; Roman-Goldstein, S.; Nilaver, G.; Weissleder, R.; Bogdanov, A.; Hellstrom, I.; Kroll, R. A.; Neuwelt, E. A., MR of carcinoma-specific monoclonal antibody conjugated to monocrystalline iron oxide nanoparticles: the potential for noninvasive diagnosis. *AJNR Am J Neuroradiol* **1996**, 17, (3), 411-8.
- (4) Medarova, Z.; Pham, W.; Kim, Y.; Dai, G.; Moore, A., In vivo imaging of tumor response to therapy using a dual-modality imaging strategy. *Int J Cancer* **2005**.
- (5) Lanza, G. M.; Wallace, K. D.; Scott, M. J.; Cacheris, W. P.; Abendschein, D. R.; Christy, D. H.; Sharkey, A. M.; Miller, J. G.; Gaffney, P. J.; Wickline, S. A., A novel site-targeted ultrasonic contrast agent with broad biomedical application. *Circulation* **1996**, 94, (12), 3334-40.
- (6) Farokhzad, O. C.; Jon, S.; Khademhosseini, A.; Tran, T. N.; Lavan, D. A.; Langer, R., Nanoparticle-aptamer bioconjugates: a new approach for targeting prostate cancer cells. *Cancer Res* **2004**, 64, (21), 7668-72.
- (7) Winter, P. M.; Caruthers, S. D.; Kassner, A.; Harris, T. D.; Chinen, L. K.; Allen, J. S.; Lacy, E. K.; Zhang, H.; Robertson, J. D.; Wickline, S. A.; Lanza, G. M., Molecular imaging of angiogenesis in nascent Vx-2 rabbit tumors using a novel alpha(nu)beta3-targeted nanoparticle and 1.5 tesla magnetic resonance imaging. *Cancer Res* **2003**, 63, (18), 5838-43.
- (8) Mosqueira, V. C.; Legrand, P.; Morgat, J. L.; Vert, M.; Mysiakine, E.; Gref, R.; Devissaguet, J. P.; Barratt, G., Biodistribution of long-circulating PEG-grafted nanocapsules in mice: effects of PEG chain length and density. *Pharm Res* **2001**, 18, (10), 1411-9.
- (9) Raja, K. S.; Wang, Q.; Gonzalez, M. J.; Manchester, M.; Johnson, J. E.; Finn, M. G., Hybrid virus-polymer materials. 1. Synthesis and properties of PEG-decorated cowpea mosaic virus. *Biomacromolecules* **2003**, 4, (3), 472-6.
- (10) Appeldoorn, C. C.; Molenaar, T. J.; Bonnefoy, A.; van Leeuwen, S. H.; Vandervoort, P. A.; Hoylaerts, M. F.; van Berkel, T. J.; Biessen, E. A., Rational

optimization of a short human P-selectin-binding peptide leads to nanomolar affinity antagonists. *J Biol Chem* **2003**, 278, (12), 10201-7.

(11) Szardenings, M.; Muceniece, R.; Mutule, I.; Mutulis, F.; Wikberg, J. E., New highly specific agonistic peptides for human melanocortin MC(1) receptor. *Peptides* **2000**, 21, (2), 239-43.

(12) Quintana, A.; Raczka, E.; Piehler, L.; Lee, I.; Myc, A.; Majoros, I.; Patri, A. K.; Thomas, T.; Mule, J.; Baker, J. R., Jr., Design and function of a dendrimer-based therapeutic nanodevice targeted to tumor cells through the folate receptor. *Pharm Res* **2002**, 19, (9), 1310-6.

(13) Choi, Y.; Thomas, T.; Kotlyar, A.; Islam, M. T.; Baker, J. R., Jr., Synthesis and functional evaluation of DNA-assembled polyamidoamine dendrimer clusters for cancer cell-specific targeting. *Chem Biol* **2005**, 12, (1), 35-43.

(14) Kam, N. W.; O'Connell, M.; Wisdom, J. A.; Dai, H., Carbon nanotubes as multifunctional biological transporters and near-infrared agents for selective cancer cell destruction. *Proc Natl Acad Sci U S A* **2005**.

(15) Kohler, N.; Sun, C.; Wang, J.; Zhang, M., Methotrexate-modified superparamagnetic nanoparticles and their intracellular uptake into human cancer cells. *Langmuir* **2005**, 21, (19), 8858-64.

(16) Zhao, R.; Goldman, I. D., Resistance to antifolates. *Oncogene* **2003**, 22, (47), 7431-57.

(17) Moghimi, S. M.; Hunter, A. C.; Murray, J. C., Long-circulating and target-specific nanoparticles: theory to practice. *Pharmacol Rev* **2001**, 53, (2), 283-318.

(18) O'Neal, D. P.; Hirsch, L. R.; Halas, N. J.; Payne, J. D.; West, J. L., Photo-thermal tumor ablation in mice using near infrared-absorbing nanoparticles. *Cancer Lett* **2004**, 209, (2), 171-6.

(19) Kim, S.; Lim, Y. T.; Soltész, E. G.; De Grand, A. M.; Lee, J.; Nakayama, A.; Parker, J. A.; Mihaljevic, T.; Laurence, R. G.; Dor, D. M.; Cohn, L. H.; Bawendi, M. G.; Frangioni, J. V., Near-infrared fluorescent type II quantum dots for sentinel lymph node mapping. *Nat Biotechnol* **2004**, 22, (1), 93-7.

(20) Flacke, S.; Fischer, S.; Scott, M. J.; Fuhrhop, R. J.; Allen, J. S.; McLean, M.; Winter, P.; Sicard, G. A.; Gaffney, P. J.; Wickline, S. A.; Lanza, G. M., Novel MRI contrast agent for molecular imaging of fibrin: implications for detecting vulnerable plaques. *Circulation* **2001**, 104, (11), 1280-5.

- (21) Winter, P. M.; Morawski, A. M.; Caruthers, S. D.; Fuhrhop, R. W.; Zhang, H.; Williams, T. A.; Allen, J. S.; Lacy, E. K.; Robertson, J. D.; Lanza, G. M.; Wickline, S. A., Molecular imaging of angiogenesis in early-stage atherosclerosis with alpha(v)beta3-integrin-targeted nanoparticles. *Circulation* **2003**, 108, (18), 2270-4.
- (22) Weissleder, R., Liver MR imaging with iron oxides: toward consensus and clinical practice. *Radiology* **1994**, 193, (3), 593-5.
- (23) Kircher, M. F.; Mahmood, U.; King, R. S.; Weissleder, R.; Josephson, L., A multimodal nanoparticle for preoperative magnetic resonance imaging and intraoperative optical brain tumor delineation. *Cancer Res* **2003**, 63, (23), 8122-5.
- (24) Gupta, H.; Weissleder, R., Targeted contrast agents in MR imaging. *Magn Reson Imaging Clin N Am* **1996**, 4, (1), 171-84.
- (25) Gupta, A. K.; Gupta, M., Synthesis and surface engineering of iron oxide nanoparticles for biomedical applications. *Biomaterials* **2005**, 26, (18), 3995-4021.
- (26) Hafeli, U. O.; Sweeney, S. M.; Beresford, B. A.; Sim, E. H.; Macklis, R. M., Magnetically directed poly(lactic acid) 90Y-microspheres: novel agents for targeted intracavitary radiotherapy. *J Biomed Mater Res* **1994**, 28, (8), 901-8.
- (27) Jain, T. K.; Morales, M. A.; Sahoo, S. K.; Leslie-Pelecky, D. L.; Labhasetwar, V., Iron oxide nanoparticles for sustained delivery of anticancer agents. *Mol Pharm* **2005**, 2, (3), 194-205.
- (28) Josephson, L.; Tung, C. H.; Moore, A.; Weissleder, R., High-efficiency intracellular magnetic labeling with novel superparamagnetic-tat peptide conjugates. *Bioconjugate Chemistry* **1999**, 10, (2), 186-191.
- (29) Schwarze, S. R.; Ho, A.; Vocero-Akbani, A.; Dowdy, S. F., In vivo protein transduction: delivery of a biologically active protein into the mouse. *Science* **1999**, 285, (5433), 1569-72.
- (30) St'astny, M.; Plocova, D.; Etrych, T.; Kovar, M.; Ulbrich, K.; Rihova, B., HEMA-hydrogels containing cytostatic drugs. Kinetics of the drug release and in vivo efficacy. *J Control Release* **2002**, 81, (1-2), 101-11.
- (31) Lanza, G. M.; Yu, X.; Winter, P. M.; Abendschein, D. R.; Karukstis, K. K.; Scott, M. J.; Chinen, L. K.; Fuhrhop, R. W.; Scherrer, D. E.; Wickline, S. A., Targeted antiproliferative drug delivery to vascular smooth muscle cells with a magnetic resonance imaging nanoparticle contrast agent: implications for rational therapy of restenosis. *Circulation* **2002**, 106, (22), 2842-7.

- (32) Ulrich, A. S., Biophysical aspects of using liposomes as delivery vehicles. *Biosci Rep* **2002**, 22, (2), 129-50.
- (33) Torchilin, V. P.; Rammohan, R.; Weissig, V.; Levchenko, T. S., TAT peptide on the surface of liposomes affords their efficient intracellular delivery even at low temperature and in the presence of metabolic inhibitors. *Proc Natl Acad Sci U S A* **2001**, 98, (15), 8786-91.
- (34) Lewin, M.; Carlesso, N.; Tung, C. H.; Tang, X. W.; Cory, D.; Scadden, D. T.; Weissleder, R., Tat peptide-derivatized magnetic nanoparticles allow in vivo tracking and recovery of progenitor cells. *Nat Biotechnol* **2000**, 18, (4), 410-4.
- (35) Jiang, T.; Olson, E. S.; Nguyen, Q. T.; Roy, M.; Jennings, P. A.; Tsien, R. Y., Tumor imaging by means of proteolytic activation of cell-penetrating peptides. *Proc Natl Acad Sci U S A* **2004**, 101, (51), 17867-72.
- (36) Frankel, A. D.; Pabo, C. O., Cellular uptake of the tat protein from human immunodeficiency virus. *Cell* **1988**, 55, (6), 1189-93.
- (37) Wadia, J. S.; Stan, R. V.; Dowdy, S. F., Transducible TAT-HA fusogenic peptide enhances escape of TAT-fusion proteins after lipid raft macropinocytosis. *Nat Med* **2004**, 10, (3), 310-5.
- (38) Vendeville, A.; Rayne, F.; Bonhoure, A.; Bettache, N.; Montcourrier, P.; Beaumelle, B., HIV-1 Tat enters T cells using coated pits before translocating from acidified endosomes and eliciting biological responses. *Mol Biol Cell* **2004**, 15, (5), 2347-60.
- (39) Mastrobattista, E.; Koning, G. A.; van Bloois, L.; Filipe, A. C.; Jiskoot, W.; Storm, G., Functional characterization of an endosome-disruptive peptide and its application in cytosolic delivery of immunoliposome-entrapped proteins. *J Biol Chem* **2002**, 277, (30), 27135-43.
- (40) Laakkonen, P.; Porkka, K.; Hoffman, J. A.; Ruoslahti, E., A tumor-homing peptide with a targeting specificity related to lymphatic vessels. *Nat Med* **2002**, 8, (7), 751-5.
- (41) Liu, Y.; Liggitt, D.; Zhong, W.; Tu, G.; Gaensler, K.; Debs, R., Cationic liposome-mediated intravenous gene delivery. *J Biol Chem* **1995**, 270, (42), 24864-70.
- (42) Dubertret, B.; Skourides, P.; Norris, D. J.; Noireaux, V.; Brivanlou, A. H.; Libchaber, A., In vivo imaging of quantum dots encapsulated in phospholipid micelles. *Science* **2002**, 298, (5599), 1759-62.

- (43) Kawano, T.; Yamagata, M.; Takahashi, H.; Niidome, Y.; Yamada, S.; Katayama, Y.; Niidome, T., Stabilizing of plasmid DNA in vivo by PEG-modified cationic gold nanoparticles and the gene expression assisted with electrical pulses. *J Control Release* **2006**.
- (44) Dabbousi, B. O.; Rodriguezviejo, J.; Mikulec, F. V.; Heine, J. R.; Mattoussi, H.; Ober, R.; Jensen, K. F.; Bawendi, M. G., (Cdse)Zns Core-Shell Quantum Dots - Synthesis and Characterization of a Size Series of Highly Luminescent Nanocrystallites. *J. Phys. Chem. B* **1997**, 101, (46), 9463-9475.
- (45) Michalet, X.; Pinaud, F. F.; Bentolila, L. A.; Tsay, J. M.; Doose, S.; Li, J. J.; Sundaresan, G.; Wu, A. M.; Gambhir, S. S.; Weiss, S., Quantum dots for live cells, in vivo imaging, and diagnostics. *Science* **2005**, 307, (5709), 538-44.
- (46) Han, M.; Gao, X.; Su, J. Z.; Nie, S., Quantum-dot-tagged microbeads for multiplexed optical coding of biomolecules. *Nat Biotechnol* **2001**, 19, (7), 631-5.
- (47) Dahan, M.; Levi, S.; Luccardini, C.; Rostaing, P.; Riveau, B.; Triller, A., Diffusion dynamics of glycine receptors revealed by single-quantum dot tracking. *Science* **2003**, 302, (5644), 442-5.
- (48) Derfus, A. M.; Chan, W. C.; Bhatia, S. N., Intracellular Delivery of Quantum Dots for Live Cell Labeling and Organelle Tracking. *Advanced Materials* **2004**, In press.
- (49) Wu, X.; Liu, H.; Liu, J.; Haley, K. N.; Treadway, J. A.; Larson, J. P.; Ge, N.; Peale, F.; Bruchez, M. P., Immunofluorescent labeling of cancer marker Her2 and other cellular targets with semiconductor quantum dots. *Nat Biotechnol* **2003**, 21, (1), 41-6.
- (50) Lidke, D. S.; Nagy, P.; Heintzmann, R.; Arndt-Jovin, D. J.; Post, J. N.; Grecco, H. E.; Jares-Erijman, E. A.; Jovin, T. M., Quantum dot ligands provide new insights into erbB/HER receptor-mediated signal transduction. *Nat Biotechnol* **2004**, 22, (2), 198-203.
- (51) Jaiswal, J. K.; Mattoussi, H.; Mauro, J. M.; Simon, S. M., Long-term multiple color imaging of live cells using quantum dot bioconjugates. *Nat Biotechnol* **2003**, 21, (1), 47-51.
- (52) Pathak, S.; Choi, S. K.; Arnheim, N.; Thompson, M. E., Hydroxylated quantum dots as luminescent probes for in situ hybridization. *J Am Chem Soc* **2001**, 123, (17), 4103-4.

- (53) Medintz, I. L.; Clapp, A. R.; Mattoussi, H.; Goldman, E. R.; Fisher, B.; Mauro, J. M., Self-assembled nanoscale biosensors based on quantum dot FRET donors. *Nature Materials* **2003**, 2, (9), 630-638.
- (54) Voura, E. B.; Jaiswal, J. K.; Mattoussi, H.; Simon, S. M., Tracking metastatic tumor cell extravasation with quantum dot nanocrystals and fluorescence emission-scanning microscopy. *Nat Med* **2004**, 10, (9), 993-8.
- (55) Larson, D. R.; Zipfel, W. R.; Williams, R. M.; Clark, S. W.; Bruchez, M. P.; Wise, F. W.; Webb, W. W., Water-soluble quantum dots for multiphoton fluorescence imaging in vivo. *Science* **2003**, 300, (5624), 1434-6.
- (56) Derfus, A. M.; Chan, W. C. W.; Bhatia, S. N., Probing the cytotoxicity of semiconductor quantum dots. *Nano Letters* **2004**, 4, (1), 11-18.
- (57) Zheng, J.; Zhang, C.; Dickson, R. M., Highly fluorescent, water-soluble, size-tunable gold quantum dots. *Phys Rev Lett* **2004**, 93, (7), 077402.
- (58) Samia, A. C.; Chen, X.; Burda, C., Semiconductor quantum dots for photodynamic therapy. *J Am Chem Soc* **2003**, 125, (51), 15736-7.
- (59) Katari, J. E. B.; Colvin, V. L.; Alivisatos, A. P., X-Ray Photoelectron Spectroscopy of Cdse Nanocrystals with Applications to Studies of the Nanocrystal Surface. *J. Phys. Chem.* **1994**, 98, (15), 4109-4117.
- (60) Schutt, E. G.; Klein, D. H.; Mattrey, R. M.; Riess, J. G., Injectable microbubbles as contrast agents for diagnostic ultrasound imaging: the key role of perfluorochemicals. *Angew Chem Int Ed Engl* **2003**, 42, (28), 3218-35.
- (61) Feinstein, S. B., The powerful microbubble: from bench to bedside, from intravascular indicator to therapeutic delivery system, and beyond. *Am J Physiol Heart Circ Physiol* **2004**, 287, (2), H450-7.
- (62) Lanza, G. M.; Wickline, S. A., Targeted ultrasonic contrast agents for molecular imaging and therapy. *Curr Probl Cardiol* **2003**, 28, (12), 625-53.
- (63) Dougherty, T. J.; Gomer, C. J.; Henderson, B. W.; Jori, G.; Kessel, D.; Korbelik, M.; Moan, J.; Peng, Q., Photodynamic therapy. *J Natl Cancer Inst* **1998**, 90, (12), 889-905.
- (64) Oseroff, A. R.; Ohuoha, D.; Hasan, T.; Bommer, J. C.; Yarmush, M. L., Antibody-targeted photolysis: selective photodestruction of human T-cell leukemia cells using monoclonal antibody-chlorin e6 conjugates. *Proc Natl Acad Sci U S A* **1986**, 83, (22), 8744-8.

- (65) Hirsch, L. R.; Stafford, R. J.; Bankson, J. A.; Sershen, S. R.; Rivera, B.; Price, R. E.; Hazle, J. D.; Halas, N. J.; West, J. L., Nanoshell-mediated near-infrared thermal therapy of tumors under magnetic resonance guidance. *Proc Natl Acad Sci U S A* **2003**, 100, (23), 13549-54.
- (66) Hainfeld, J. F.; Slatkin, D. N.; Smilowitz, H. M., The use of gold nanoparticles to enhance radiotherapy in mice. *Phys Med Biol* **2004**, 49, (18), N309-15.
- (67) Hamad-Schifferli, K.; Schwartz, J. J.; Santos, A. T.; Zhang, S.; Jacobson, J. M., Remote electronic control of DNA hybridization through inductive coupling to an attached metal nanocrystal antenna. *Nature* **2002**, 415, (6868), 152-5.
- (68) Rabin, Y., Is intracellular hyperthermia superior to extracellular hyperthermia in the thermal sense? *Int J Hyperthermia* **2002**, 18, (3), 194-202.
- (69) Jordan, A.; Wust, P.; Fahling, H.; John, W.; Hinz, A.; Felix, R., Inductive Heating of Ferrimagnetic Particles and Magnetic Fluids - Physical Evaluation of Their Potential for Hyperthermia. *International Journal of Hyperthermia* **1993**, 9, (1), 51-68.
- (70) Stauffer, P. R.; Cetas, T. C.; Jones, R. C., Magnetic Induction-Heating of Ferromagnetic Implants for Inducing Localized Hyperthermia in Deep-Seated Tumors. *Ieee Transactions on Biomedical Engineering* **1984**, 31, (2), 235-251.
- (71) Jordan, A.; Wust, P.; Scholz, R.; Tesche, B.; Fahling, H.; Mitrovics, T.; Vogl, T.; Cervos-Navarro, J.; Felix, R., Cellular uptake of magnetic fluid particles and their effects on human adenocarcinoma cells exposed to AC magnetic fields in vitro. *Int J Hyperthermia* **1996**, 12, (6), 705-22.
- (72) Jordan, A.; Scholz, R.; Wust, P.; Fahling, H.; Krause, J.; Wlodarczyk, W.; Sander, B.; Vogl, T.; Felix, R., Effects of magnetic fluid hyperthermia (MFH) on C3H mammary carcinoma in vivo. *Int J Hyperthermia* **1997**, 13, (6), 587-605.
- (73) Jordan, A.; Scholz, R.; Wust, P.; Fahling, H.; Felix, R., Magnetic fluid hyperthermia (MFH): Cancer treatment with AC magnetic field induced excitation of biocompatible superparamagnetic nanoparticles. *Journal of Magnetism and Magnetic Materials* **1999**, 201, 413-419.
- (74) Gneveckow, U.; Jordan, A.; Scholz, R.; Bruss, V.; Waldofner, N.; Rieke, J.; Feussner, A.; Hildebrandt, B.; Rau, B.; Wust, P., Description and characterization of the novel hyperthermia- and thermoablation-system MFH 300F for clinical magnetic fluid hyperthermia. *Med Phys* **2004**, 31, (6), 1444-51.

- (75) Hildebrandt, B.; Wust, P.; Ahlers, O.; Dieing, A.; Sreenivasa, G.; Kerner, T.; Felix, R.; Riess, H., The cellular and molecular basis of hyperthermia. *Crit Rev Oncol Hematol* **2002**, 43, (1), 33-56.
- (76) Wust, P.; Hildebrandt, B.; Sreenivasa, G.; Rau, B.; Gellermann, J.; Riess, H.; Felix, R.; Schlag, P. M., Hyperthermia in combined treatment of cancer. *Lancet Oncol* **2002**, 3, (8), 487-97.
- (77) Gobel, U.; Calaminus, G.; Schneider, D. T.; Schmidt, P.; Haas, R. J., Management of germ cell tumors in children: approaches to cure. *Onkologie* **2002**, 25, (1), 14-22.
- (78) Chan, W. C.; Nie, S., Quantum dot bioconjugates for ultrasensitive nonisotopic detection. *Science* **1998**, 281, (5385), 2016-8.
- (79) Parak, W. J.; Boudreau, R.; Le Gros, M.; Gerion, D.; Zanchet, D.; Micheel, C. M.; Williams, S. C.; Alivisatos, A. P.; Larabell, C., Cell motility and metastatic potential studies based on quantum dot imaging of phagokinetic tracks. *Adv. Mater.* **2002**, 14, (12), 882-885.
- (80) Hines, M. A.; Guyot-Sionnest, P., Synthesis and Characterization of Strongly Luminescing ZnS-Capped CdSe Nanocrystals. *J. Phys. Chem.* **1996**, 100, (2), 468-471.
- (81) Zuhorn, I. S.; Hoekstra, D., On the mechanism of cationic amphiphile-mediated transfection. To fuse or not to fuse: is that the question? *J Membr Biol* **2002**, 189, (3), 167-79.
- (82) Brock, R.; Jovin, T. M., Heterogeneity of signal transduction at the subcellular level: microsphere-based focal EGF receptor activation and stimulation of Shc translocation. *J Cell Sci* **2001**, 114, (Pt 13), 2437-47.
- (83) Pemberton, L. F.; Blobel, G.; Rosenblum, J. S., Transport routes through the nuclear pore complex. *Curr Opin Cell Biol* **1998**, 10, (3), 392-9.
- (84) Rizzuto, R.; Nakase, H.; Darras, B.; Francke, U.; Fabrizi, G. M.; Mengel, T.; Walsh, F.; Kadenbach, B.; DiMauro, S.; Schon, E. A., A gene specifying subunit VIII of human cytochrome c oxidase is localized to chromosome 11 and is expressed in both muscle and non-muscle tissues. *J Biol Chem* **1989**, 264, (18), 10595-600.
- (85) Tsong, T. Y., Electroporation of cell membranes. *Biophys J* **1991**, 60, (2), 297-306.
- (86) Gao, X.; Chan, W. C.; Nie, S., Quantum-dot nanocrystals for ultrasensitive biological labeling and multicolor optical encoding. *J Biomed Opt* **2002**, 7, (4), 532-7.

- (87) Derfus, A. M.; Chan, W. C.; Bhatia, S. N., Probing the Cytotoxicity of Semiconductor Quantum Dots. *Nano Letters* **2004**, in press.
- (88) Golzio, M.; Teissie, J.; Rols, M. P., Direct visualization at the single-cell level of electrically mediated gene delivery. *Proc Natl Acad Sci U S A* **2002**, 99, (3), 1292-7.
- (89) Bremner, K. H.; Seymour, L. W.; Pouton, C. W., Harnessing nuclear localization pathways for transgene delivery. *Curr Opin Mol Ther* **2001**, 3, (2), 170-7.
- (90) Hubner, S.; Xiao, C. Y.; Jans, D. A., The protein kinase CK2 site (Ser111/112) enhances recognition of the simian virus 40 large T-antigen nuclear localization sequence by importin. *J Biol Chem* **1997**, 272, (27), 17191-5.
- (91) Pante, N.; Kann, M., Nuclear pore complex is able to transport macromolecules with diameters of about 39 nm. *Mol Biol Cell* **2002**, 13, (2), 425-34.
- (92) Manfredi, G.; Fu, J.; Ojaimi, J.; Sadlock, J. E.; Kwong, J. Q.; Guy, J.; Schon, E. A., Rescue of a deficiency in ATP synthesis by transfer of MTATP6, a mitochondrial DNA-encoded gene, to the nucleus. *Nat Genet* **2002**, 30, (4), 394-9.
- (93) Poot, M.; Zhang, Y. Z.; Kramer, J. A.; Wells, K. S.; Jones, L. J.; Hanzel, D. K.; Lugade, A. G.; Singer, V. L.; Haugland, R. P., Analysis of mitochondrial morphology and function with novel fixable fluorescent stains. *J Histochem Cytochem* **1996**, 44, (12), 1363-72.
- (94) Fire, A.; Xu, S.; Montgomery, M. K.; Kostas, S. A.; Driver, S. E.; Mello, C. C., Potent and specific genetic interference by double-stranded RNA in *Caenorhabditis elegans*. *Nature* **1998**, 391, (6669), 806-11.
- (95) Kamath, R. S.; Fraser, A. G.; Dong, Y.; Poulin, G.; Durbin, R.; Gotta, M.; Kanapin, A.; Le Bot, N.; Moreno, S.; Sohrmann, M.; Welchman, D. P.; Zipperlen, P.; Ahringer, J., Systematic functional analysis of the *Caenorhabditis elegans* genome using RNAi. *Nature* **2003**, 421, (6920), 231-7.
- (96) Maeda, I.; Kohara, Y.; Yamamoto, M.; Sugimoto, A., Large-scale analysis of gene function in *Caenorhabditis elegans* by high-throughput RNAi. *Curr Biol* **2001**, 11, (3), 171-6.
- (97) Boutros, M.; Kiger, A. A.; Armknecht, S.; Kerr, K.; Hild, M.; Koch, B.; Haas, S. A.; Consortium, H. F.; Paro, R.; Perrimon, N., Genome-wide RNAi analysis of growth and viability in *Drosophila* cells. *Science* **2004**, 303, (5659), 832-5.
- (98) Novina, C. D.; Sharp, P. A., The RNAi revolution. *Nature* **2004**, 430, (6996), 161-4.

- (99) Semizarov, D.; Frost, L.; Sarthy, A.; Kroeger, P.; Halbert, D. N.; Fesik, S. W., Specificity of short interfering RNA determined through gene expression signatures. *Proc Natl Acad Sci U S A* **2003**, 100, (11), 6347-52.
- (100) Raab, R. M.; Stephanopoulos, G., Dynamics of gene silencing by RNA interference. *Biotechnol Bioeng* **2004**, 88, (1), 121-32.
- (101) Huppi, K.; Martin, S. E.; Caplen, N. J., Defining and assaying RNAi in mammalian cells. *Mol Cell* **2005**, 17, (1), 1-10.
- (102) Spagnou, S.; Miller, A. D.; Keller, M., Lipidic carriers of siRNA: differences in the formulation, cellular uptake, and delivery with plasmid DNA. *Biochemistry* **2004**, 43, (42), 13348-56.
- (103) Oberdoerffer, P.; Kanellopoulou, C.; Heissmeyer, V.; Paeper, C.; Borowski, C.; Aifantis, I.; Rao, A.; Rajewsky, K., Efficiency of RNA interference in the mouse hematopoietic system varies between cell types and developmental stages. *Mol Cell Biol* **2005**, 25, (10), 3896-905.
- (104) McManus, M. T.; Sharp, P. A., Gene silencing in mammals by small interfering RNAs. *Nat Rev Genet* **2002**, 3, (10), 737-47.
- (105) Muratovska, A.; Eccles, M. R., Conjugate for efficient delivery of short interfering RNA (siRNA) into mammalian cells. *FEBS Lett* **2004**, 558, (1-3), 63-8.
- (106) Lorenz, C.; Hadwiger, P.; John, M.; Vornlocher, H. P.; Unverzagt, C., Steroid and lipid conjugates of siRNAs to enhance cellular uptake and gene silencing in liver cells. *Bioorg Med Chem Lett* **2004**, 14, (19), 4975-7.
- (107) Schiffelers, R. M.; Ansari, A.; Xu, J.; Zhou, Q.; Tang, Q.; Storm, G.; Molema, G.; Lu, P. Y.; Scaria, P. V.; Woodle, M. C., Cancer siRNA therapy by tumor selective delivery with ligand-targeted sterically stabilized nanoparticle. *Nucleic Acids Res* **2004**, 32, (19), e149.
- (108) Itaka, K.; Kanayama, N.; Nishiyama, N.; Jang, W. D.; Yamasaki, Y.; Nakamura, K.; Kawaguchi, H.; Kataoka, K., Supramolecular nanocarrier of siRNA from PEG-based block cationic polymer carrying diamine side chain with distinctive pKa directed to enhance intracellular gene silencing. *J Am Chem Soc* **2004**, 126, (42), 13612-3.
- (109) Soutschek, J.; Akinc, A.; Bramlage, B.; Charisse, K.; Constien, R.; Donoghue, M.; Elbashir, S.; Geick, A.; Hadwiger, P.; Harborth, J.; John, M.; Kesavan, V.; Lavine, G.; Pandey, R. K.; Racie, T.; Rajeev, K. G.; Rohl, I.; Toudjarska, I.; Wang, G.; Wuschko, S.; Bumcrot, D.; Koteliensky, V.; Limmer, S.; Manoharan, M.; Vornlocher, H. P., Therapeutic silencing of an endogenous gene by systemic administration of modified siRNAs. *Nature* **2004**, 432, (7014), 173-8.

- (110) Chiu, Y. L.; Ali, A.; Chu, C. Y.; Cao, H.; Rana, T. M., Visualizing a correlation between siRNA localization, cellular uptake, and RNAi in living cells. *Chem Biol* **2004**, 11, (8), 1165-75.
- (111) Kumar, R.; Conklin, D. S.; Mittal, V., High-throughput selection of effective RNAi probes for gene silencing. *Genome Res* **2003**, 13, (10), 2333-40.
- (112) Hemann, M. T.; Fridman, J. S.; Zilfou, J. T.; Hernando, E.; Paddison, P. J.; Cordon-Cardo, C.; Hannon, G. J.; Lowe, S. W., An epi-allelic series of p53 hypomorphs created by stable RNAi produces distinct tumor phenotypes in vivo. *Nat Genet* **2003**, 33, (3), 396-400.
- (113) Derfus, A. M.; Chan, W. C.; Bhatia, S., Probing the cytotoxicity of semiconductor quantum dots. *Nano Letters* **2004**, 4, (1), 11-18.
- (114) Mattheakis, L. C.; Dias, J. M.; Choi, Y. J.; Gong, J.; Bruchez, M. P.; Liu, J.; Wang, E., Optical coding of mammalian cells using semiconductor quantum dots. *Anal Biochem* **2004**, 327, (2), 200-8.
- (115) Derfus, A. M.; Chan, W. C. W.; Bhatia, S. N., Intracellular Delivery of Quantum Dots for Live Cell Labeling and Organelle Tracking. *Advanced Materials* **2004**, 16, (12), 961-966.
- (116) Rheinwald, J. G.; Green, H., Serial cultivation of strains of human epidermal keratinocytes: the formation of keratinizing colonies from single cells. *Cell* **1975**, 6, (3), 331-43.
- (117) Ranscht, B.; Dours-Zimmermann, M. T., T-cadherin, a novel cadherin cell adhesion molecule in the nervous system lacks the conserved cytoplasmic region. *Neuron* **1991**, 7, (3), 391-402.
- (118) Seglen, P. O., Preparation of isolated rat liver cells. *Methods Cell Biol* **1976**, 13, 29-83.
- (119) Dunn, J. C.; Yarmush, M. L.; Koebe, H. G.; Tompkins, R. G., Hepatocyte function and extracellular matrix geometry: long-term culture in a sandwich configuration. *Faseb J* **1989**, 3, (2), 174-7.
- (120) Bhatia, S. N.; Balis, U. J.; Yarmush, M. L.; Toner, M., Effect of cell-cell interactions in preservation of cellular phenotype: cocultivation of hepatocytes and nonparenchymal cells. *Faseb J* **1999**, 13, (14), 1883-900.

- (121) Chen, A. A.; Derfus, A. M.; Khetani, S. R.; Bhatia, S. N., Quantum dots to monitor RNAi delivery and improve gene silencing. *Nucleic Acids Res* **2005**, *33*, (22), e190.
- (122) Allen, J. W.; Johnson, R. S.; Bhatia, S. N., Hypoxic inhibition of 3-methylcholanthrene-induced CYP1A1 expression is independent of HIF-1alpha. *Toxicol Lett* **2005**, *155*, (1), 151-9.
- (123) Behnia, K.; Bhatia, S.; Jastromb, N.; Balis, U.; Sullivan, S.; Yarmush, M.; Toner, M., Xenobiotic metabolism by cultured primary porcine hepatocytes. *Tissue Eng* **2000**, *6*, (5), 467-79.
- (124) Kennedy, S.; Wang, D.; Ruvkun, G., A conserved siRNA-degrading RNase negatively regulates RNA interference in *C. elegans*. *Nature* **2004**, *427*, (6975), 645-9.
- (125) Sledz, C. A.; Holko, M.; de Veer, M. J.; Silverman, R. H.; Williams, B. R., Activation of the interferon system by short-interfering RNAs. *Nat Cell Biol* **2003**, *5*, (9), 834-9.
- (126) Jackson, A. L.; Bartz, S. R.; Schelter, J.; Kobayashi, S. V.; Burchard, J.; Mao, M.; Li, B.; Cavet, G.; Linsley, P. S., Expression profiling reveals off-target gene regulation by RNAi. *Nat Biotechnol* **2003**, *21*, (6), 635-7.
- (127) Hirko, A.; Tang, F.; Hughes, J. A., Cationic lipid vectors for plasmid DNA delivery. *Curr Med Chem* **2003**, *10*, (14), 1185-93.
- (128) Song, E.; Zhu, P.; Lee, S. K.; Chowdhury, D.; Kussman, S.; Dykxhoorn, D. M.; Feng, Y.; Palliser, D.; Weiner, D. B.; Shankar, P.; Marasco, W. A.; Lieberman, J., Antibody mediated in vivo delivery of small interfering RNAs via cell-surface receptors. *Nat Biotechnol* **2005**, *23*, (6), 709-17.
- (129) Hu-Lieskovan, S.; Heidel, J. D.; Bartlett, D. W.; Davis, M. E.; Triche, T. J., Sequence-specific knockdown of EWS-FLI1 by targeted, nonviral delivery of small interfering RNA inhibits tumor growth in a murine model of metastatic Ewing's sarcoma. *Cancer Res* **2005**, *65*, (19), 8984-92.
- (130) Christian, S.; Pilch, J.; Akerman, M. E.; Porkka, K.; Laakkonen, P.; Ruoslahti, E., Nucleolin expressed at the cell surface is a marker of endothelial cells in angiogenic blood vessels. *J Cell Biol* **2003**, *163*, (4), 871-8.
- (131) Plank, C.; Oberhauser, B.; Mechtler, K.; Koch, C.; Wagner, E., The influence of endosome-disruptive peptides on gene transfer using synthetic virus-like gene transfer systems. *J. Biol. Chem.* **1994**, *269*, (17), 12918-12924.

- (132) Lam, C. W.; James, J. T.; McCluskey, R.; Hunter, R. L., Pulmonary Toxicity of Single-Wall Carbon Nanotubes in Mice 7 and 90 Days after Intratracheal Instillation. *Toxicol Sci* **2003**.
- (133) Warheit, D. B.; Laurence, B. R.; Reed, K. L.; Roach, D. H.; Reynolds, G. A.; Webb, T. R., Comparative Pulmonary Toxicity Assessment of Single Wall Carbon Nanotubes in Rats. *Toxicol Sci* **2003**.
- (134) Bruchez, M.; Moronne, M.; Gin, P.; Weiss, S.; Alivisatos, A. P., Semiconductor Nanocrystals as Fluorescent Biological Labels. *Science* **1998**, 281, (5385), 2013-2016.
- (135) Hanaki, K.; Momo, A.; Oku, T.; Komoto, A.; Maenosono, S.; Yamaguchi, Y.; Yamamoto, K., Semiconductor quantum dot/albumin complex is a long-life and highly photostable endosome marker. *Biochem Biophys Res Commun* **2003**, 302, (3), 496-501.
- (136) Seydel, C., Quantum dots get wet. *Science* **2003**, 300, (5616), 80-81.
- (137) Dagani, R., Nanomaterials: Safe or Unsafe? *Chemical and Engineering News* **2003**, 81, (17), 30-33.
- (138) Colvin, V. L., The potential environmental impact of engineered nanomaterials. *Nat Biotechnol* **2003**, 21, (10), 1166-70.
- (139) Santone, K. S.; Acosta, D.; Bruckner, J. V., Cadmium toxicity in primary cultures of rat hepatocytes. *J Toxicol Environ Health* **1982**, 10, (1), 169-77.
- (140) Limaye, D. A.; Shaikh, Z. A., Cytotoxicity of cadmium and characteristics of its transport in cardiomyocytes. *Toxicol Appl Pharmacol* **1999**, 154, (1), 59-66.
- (141) Rikans, L. E.; Yamano, T., Mechanisms of cadmium-mediated acute hepatotoxicity. *J Biochem Mol Toxicol* **2000**, 14, (2), 110-7.
- (142) Liu, J.; Kershaw, W. C.; Klaassen, C. D., Rat primary hepatocyte cultures are a good model for examining metallothionein-induced tolerance to cadmium toxicity. *In Vitro Cell Dev Biol* **1990**, 26, (1), 75-9.
- (143) Bhatia, S. N.; Yarmush, M. L.; Toner, M., Controlling cell interactions by micropatterning in co-cultures: hepatocytes and 3T3 fibroblasts. *J Biomed Mater Res* **1997**, 34, (2), 189-99.
- (144) Aldana, J.; Wang, Y. A.; Peng, X. G., Photochemical instability of CdSe nanocrystals coated by hydrophilic thiols. *J. Am. Chem. Soc.* **2001**, 123, (36), 8844-8850.

- (145) Spanhel, L.; Haase, M.; Weller, H.; Henglein, A., Photochemistry of Colloidal Semiconductors. 20. Surface Modifications and Stability of Strong Luminescing CdS Particles. *J Am Chem Soc* **1987**, 109, 5649-5655.
- (146) Alivisatos, A. P., Perspectives on the Physical Chemistry of Semiconductor Nanocrystals. *J. Phys. Chem.* **1996**, 100, (31), 13226-13239.
- (147) Wang, Y. A.; Li, J. J.; Chen, H. Y.; Peng, X. G., Stabilization of inorganic nanocrystals by organic dendrons. *J. Am. Chem. Soc.* **2002**, 124, (10), 2293-2298.
- (148) Mattoussi, H.; Mauro, J. M.; Goldman, E. R.; Anderson, G. P.; Sundar, V. C.; Mikulec, F. V.; Bawendi, M. G., Self-assembly of CdSe-ZnS quantum dot bioconjugates using an engineered recombinant protein. *Journal of the American Chemical Society* **2000**, 122, (49), 12142-12150.
- (149) Rose, B. D.; Rennke, H. G., *Renal Pathophysiology*. ed.; Williams & Wilkins: Baltimore, 1994; 'Vol.' p 351.
- (150) Lund, U.; Rippe, A.; Venturoli, D.; Tenstad, O.; Grubb, A.; Rippe, B., Glomerular filtration rate dependence of sieving of albumin and some neutral proteins in rat kidneys. *Am J Physiol Renal Physiol* **2003**, 284, (6), F1226-34.
- (151) Brzoska, M. M.; Kaminski, M.; Supernak-Bobko, D.; Zwierz, K.; Moniuszko-Jakoniuk, J., Changes in the structure and function of the kidney of rats chronically exposed to cadmium. I. Biochemical and histopathological studies. *Arch Toxicol* **2003**, 77, (6), 344-52.
- (152) Elisseeff, J.; Anseth, K.; Sims, D.; McIntosh, W.; Randolph, M.; Langer, R., Transdermal photopolymerization for minimally invasive implantation. *Proc Natl Acad Sci USA* **1999**, 96, (6), 3104-7.
- (153) Stacey, N. H.; Klaassen, C. D., Comparison of the effects of metals on cellular injury and lipid peroxidation in isolated rat hepatocytes. *J Toxicol Environ Health* **1981**, 7, (1), 139-47.
- (154) Goyer, R. A., Nutrition and metal toxicity. *Am J Clin Nutr* **1995**, 61, (3 Suppl), 646S-650S.
- (155) Bhatia, S. N.; Balis, U. J.; Yarmush, M. L.; Toner, M., Effect of cell-cell interactions in preservation of cellular phenotype: cocultivation of hepatocytes and nonparenchymal cells. *Faseb J* **1999**, 13, (14), 1883-900.
- (156) Kloepfer, J. A.; Mielke, R. E.; Wong, M. S.; Nealson, K. H.; Stucky, G.; Nadeau, J. L., Quantum Dots as Strain- and Metabolism-Specific Microbiological Labels. *Appl. Environ. Microbiol.* **2003**, 69, (7), 4205-4213.

- (157) Ferrari, M., Cancer nanotechnology: opportunities and challenges. *Nat Rev Cancer* **2005**, 5, (3), 161-71.
- (158) Gref, R.; Minamitake, Y.; Peracchia, M. T.; Trubetskoy, V.; Torchilin, V.; Langer, R., Biodegradable long-circulating polymeric nanospheres. *Science* **1994**, 263, (5153), 1600-3.
- (159) Sengupta, S.; Eavarone, D.; Capila, I.; Zhao, G.; Watson, N.; Kiziltepe, T.; Sasisekharan, R., Temporal targeting of tumour cells and neovasculature with a nanoscale delivery system. *Nature* **2005**, 436, (7050), 568-72.
- (160) Hilger, I.; Hiergeist, R.; Hergt, R.; Winnefeld, K.; Schubert, H.; Kaiser, W. A., Thermal ablation of tumors using magnetic nanoparticles: an in vivo feasibility study. *Invest Radiol* **2002**, 37, (10), 580-6.
- (161) Young, J. H.; Wang, M. T.; Brezovich, I. A., Frequency/depth penetration considerations in hyperthermia by magnetically induced currents. *Electron Lett* **1980**, 16, 358-359.
- (162) Jin, R.; Wu, G.; Li, Z.; Mirkin, C. A.; Schatz, G. C., What controls the melting properties of DNA-linked gold nanoparticle assemblies? *J Am Chem Soc* **2003**, 125, (6), 1643-54.
- (163) Santini, J. T., Jr.; Cima, M. J.; Langer, R., A controlled-release microchip. *Nature* **1999**, 397, (6717), 335-8.
- (164) Santini, J. T.; Richards, A. C.; Scheidt, R.; Cima, M. J.; Langer, R., Microchips as controlled drug-delivery devices. *Angewandte Chemie-International Edition* **2000**, 39, (14), 2397-2407.
- (165) Richards Grayson, A. C.; Choi, I. S.; Tyler, B. M.; Wang, P. P.; Brem, H.; Cima, M. J.; Langer, R., Multi-pulse drug delivery from a resorbable polymeric microchip device. *Nat Mater* **2003**, 2, (11), 767-72.
- (166) Brem, H.; Gabikian, P., Biodegradable polymer implants to treat brain tumors. *J Control Release* **2001**, 74, (1-3), 63-7.
- (167) Weissleder, R.; Kelly, K.; Sun, E. Y.; Shtatland, T.; Josephson, L., Cell-specific targeting of nanoparticles by multivalent attachment of small molecules. *Nat Biotechnol* **2005**, 23, (11), 1418-23.
- (168) Ballou, B.; Lagerholm, B. C.; Ernst, L. A.; Bruchez, M. P.; Waggoner, A. S., Noninvasive imaging of quantum dots in mice. *Bioconjug Chem* **2004**, 15, (1), 79-86.